In vivo functional profiling and structural characterisation of the human *Glp1r* A316T variant

Liliane El Eid[1], Kieran Deane-Alder[2,3], Roxana-Maria Rujan[4], Zamara Mariam[4], Affiong I. Oqua[1], Yusman Manchanda[1], Matthew J. Belousoff[2,3], Jorge Bernardino de la Serna[5], Kyle W. Sloop[6], Guy A. Rutter[1,7,8,9], Alex Montoya[10], Dominic J. Withers[10,11], Steven J. Millership[1], Karim Bouzakri[12], Ben Jones[13], Christopher A. Reynolds[4,14], Patrick M. Sexton[2,3], Denise Wootten[2,3], Giuseppe Deganutti[4], and Alejandra Tomas[1,*]

[1] Section of Cell Biology and Functional Genomics, Division of Diabetes, Endocrinology and Metabolism, Department of Metabolism, Digestion and Reproduction, Imperial College London, London, United Kingdom.

[2] Drug Discovery Biology, Monash Institute of Pharmaceutical Sciences, Monash University, Parkville, Victoria, Australia.

[3] ARC Centre for Cryo-Electron Microscopy of Membrane Proteins, Monash Institute of Pharmaceutical Sciences, Monash University, Parkville, Victoria, Australia.

[4] Centre for Health and Life Sciences, Coventry University, Coventry, United Kingdom.

[5] National Heart and Lung Institute, Imperial College London, London, United Kingdom.

[6] Diabetes, Obesity and Complications, Lilly Research Laboratories, Eli Lilly and Company, Indianapolis, Indiana, United States.

[7] CHUM Research Centre, Faculty of Medicine, University of Montreal, Quebec, Canada.

[8] Research Institute of the McGill University Health Centre, Montreal, QC, Canada.

[9] LKC School of Medicine, Nanyang Technological University, Singapore.

[10] MRC Laboratory of Medical Sciences, London, United Kingdom.

[11] Institute of Clinical Sciences, Faculty of Medicine, Imperial College London, London, United Kingdom.

[12] Centre Européen d'Étude du Diabète, Strasbourg, France.

[13] Section of Endocrinology and Investigative Medicine, Division of Diabetes, Endocrinology and Metabolism, Department of Metabolism, Digestion and Reproduction, Imperial College London, London, United Kingdom.

[14] School of Life Sciences, University of Essex, Colchester, United Kingdom.

* Corresponding author; E-mail: a.tomas-catala@imperial.ac.uk

Abstract

Glucagon-like peptide-1 receptor (GLP-1R) agonists are a highly effective therapy class for type 2 diabetes (T2D) and obesity, yet there are variable patient responses. Variation in the human *Glp1r* gene leading to altered receptor structure, signal transduction, and function might be directly linked to therapeutic responses in patients. A naturally occurring, low-frequency, gain-of-function missense variant, rs10305492 G>A (A316T), protects against T2D and cardiovascular disease. Here we employ CRISPR/Cas9 technology to generate a humanised knock-in mouse model bearing the homozygous *Glp1r* A316T substitution. Human *Glp1r* $^{A316T/A316T}$ mice displayed lower fasting blood glucose levels and improved glucose tolerance, as well as increased plasma insulin levels and insulin secretion responses, even under metabolic stress. They also exhibited alterations in islet cytoarchitecture and β-cell identity indicative of compensatory mechanisms under a high-fat, high-sucrose (HFHS) diet challenge. Across all models investigated, the human *Glp1r* A316T variant exhibited characteristics of constitutive activation but blunted incretin-induced responses. Our results are further supported by cryo-EM analysis and molecular dynamics (MD) simulations of the GLP-1R A316T structure, demonstrating that the A316T *Glp1r* variant governs basal receptor activity and pharmacological responses to GLP-1R-targeting anti-diabetic therapies, highlighting the importance of the precise molecular characterisation of human *Glp1r* variants to predict individual therapy responses.

Introduction

The glucagon-like peptide-1 receptor (GLP-1R), an important drug target for the treatment of type 2 diabetes (T2D), obesity, and cardiovascular disease, is a class B1 secretin-like G protein-coupled receptor (GPCR) predominantly expressed in the pancreas and cardiac tissue, but also present in other organs such as the brainstem, stomach, intestine, and kidneys[1, 2]. The endogenous ligand for GLP-1R, GLP-1, is a 30 amino acid peptide incretin hormone secreted into the bloodstream from intestinal L-cells upon food intake[3], unsuitable for pharmacological use due to its short half-life (~2 mins) – with several GLP-1 analogues developed to bypass rapid degradation by the enzyme dipeptidyl peptidase 4 (DPP-4) and prolong pharmacokinetics[4], including semaglutide (Ozempic, Wegovy), proven clinically successful in reducing blood glucose levels, gastric emptying, appetite, and body weight[5, 6]. Akin to other GPCRs, the GLP-1R undergoes a conformational change upon agonist binding, allowing it to pleiotropically couple with heterotrimeric G proteins[7, 8], with preferential engagement of $G\alpha_s$, leading to activation of adenylate cyclase, cyclic adenosine monophosphate (cAMP) generation, potentiation of intracellular calcium, insulin granule mobilisation and exocytosis in pancreatic β-cells[3, 9]. Active GLP-1R plays a crucial role in regulating blood glucose homeostasis from pancreatic and extra-pancreatic tissues, including the abovementioned potentiation of glucose-stimulated insulin secretion as well as inhibition of glucagon secretion, delayed gastric emptying, and appetite suppression in the brain[3, 10], with further physiological functions such as blood pressure regulation[11, 12], maintenance of renal function[13, 14], neuroprotection, and improved learning and memory[15-18], revealed by recent studies.

Despite the success of newly developed GLP-1R agonists (GLP-1RAs) in the clinic, there is considerable heterogeneity amongst patient responses, with some exhibiting marked improvement while others showing little to no beneficial effect, and/or prominent adverse side effects[19]. Natural genetic variants of human GPCRs can be linked to clinical and physiological changes associated with receptor disfunction, e.g., alterations in receptor structure, basal and ligand-dependent activity, and/or level of expression[20]. As

one of the most studied class B1 GPCRs, several naturally occurring *Glp1r* missense variants have been identified, some of which are associated with T2D risk and related glycaemic traits in genome-wide association studies (GWAS)[21-24]. Large-scale sequencing and functional genetics analyses have revealed a low-frequency *Glp1r* missense variant (Ala316Thr; rs10305492; MAF = 1.4%), associated with lower fasting glucose, and reduced risk of T2D and cardiovascular disease[21-23]. The consequences of this variant on receptor function and their relationship with metabolic traits remain poorly defined, with conflicting results reported[25, 26]. Previous structural clues about this variant, as well as initial *in vitro* assessments of variant receptor signalling, have suggested that it confers a gain-of-function (GoF) phenotype[23, 27, 28], but in-depth characterisation of its functional effects in relevant tissues and *in vivo* has not been performed, precluding the generation of useful guidelines for the sub-classification of T2D patients for disease management related to the presence of this or other *Glp1r* genetic variants.

Here we present a detailed comparison between the human wildtype (WT) and Ala316Thr (A316T) GLP-1R, including functional characterisation and responses to incretin therapies in pancreatic β-cells, primary murine and human islets, as well as assessment of the *in vivo* consequences of the A316T variant using a newly generated humanised *Glp1r* mouse model bearing a homozygous A316T (c.946G>A, p.A316T) substitution in the human *Glp1r* gene (*hGlp1r* $^{A316T/A316T}$), both under physiological conditions as well as following diabetes induction by prolonged exposure to a high-fat, high-sucrose (HFHS) diet. We additionally present the cryo-EM structure of the A316T GLP-1R bound to its endogenous agonist, GLP-1, together with computational analyses, based on molecular dynamics (MD) simulations of WT *versus* A316T receptors, that elucidate the structural changes in the receptor underling the functional effects of the A316T variant.

Results

Human Glp1r $^{A316T/A316T}$ mice exhibit enhanced glucose homeostasis but reduced pharmacological responses to GLP-1RAs under different nutritional states

A mouse line expressing human GLP-1R from the murine *Glp1r* locus was previously generated via homologous recombination[29]. To study the biological function of the human rs10305492 G>A *Glp1r* variant, a global knock-in mouse model harbouring the A316T single nucleotide polymorphism (SNP) (*hGlp1r* $^{A316T/A316T}$) was generated using a CRISPR/Cas9 approach, with WT *hGlp1r* $^{+/+}$ littermates used as controls (Extended Data Fig. 1a,b). Genotypes were confirmed by PCR and Sanger sequencing, followed by glucose homeostasis studies in a mixed sex cohort.

Despite no discernible weight differences between *hGlp1r* $^{A316T/A316T}$ and WT littermates (Fig. 1a), glucose tolerance was markedly improved following an oral gavage (Fig. 1b), and fasting blood glucose levels were significantly lower in the *hGlp1r* $^{A316T/A316T}$ mice on a chow diet (Fig. 1c), confirming previously reported human GWAS data[21-23]. To examine the acute *versus* sustained pharmacogenetic effects of the GLP-1R A316T variant, we performed intraperitoneal glucose tolerance tests (IPGTTs) immediately after (acute) and six hours post-administration of vehicle (saline) or the GLP-1RAs exendin-4 or exendin-F1. We observed significantly improved acute glucose responses to vehicle administration in *hGlp1r* $^{A316T/A316T}$ *versus* WT *hGlp1r* $^{+/+}$ littermate mice, with a similar trend at the 6 hour time-point (Fig. 1d,e). Conversely, *hGlp1r* $^{A316T/A316T}$ and WT *hGlp1r* $^{+/+}$ mice exhibited similar glucose responses to exendin-4, both acutely and 6 hours post-agonist administration (Fig. 1f,g), with comparable glucoregulatory loss at the 6 hour time-point, associated with exendin-4-induced receptor desensitisation effects[30]. A similar trend could be observed acutely with the biased agonist exendin-F1, which, as expected by its bias profile away from β-arrestin recruitment, displayed reduced desensitisation in both mouse genotypes *versus* exendin-4[30], although prolonged glucose levels were marginally improved for *hGlp1r* $^{A316T/A316T}$ mice (Fig. 1h), without reaching statistical significance when measured as areas under the curve (AUCs) *versus* WT *hGlp1r* $^{+/+}$ mice (Fig. 1i). Direct comparison between AUCs for the different conditions and genotypes analysed per time-point is shown in Extended Data Fig. 2a,b. Agonist-specific glycaemic responses (ΔAUC, corresponding to agonist- minus vehicle-treated AUC differences) revealed significantly reduced acute

exendin-4 responses in *hGlp1r* $^{A316T/A316T}$ *versus* WT *hGlp1r* $^{+/+}$ littermates, a difference that was maintained at the 6 hour time-point, when exendin-4 treatment resulted in a paradoxical increase in blood glucose levels compared to vehicle administration in *hGlp1r* $^{A316T/A316T}$ mice (Fig. 1j). Interestingly, while *hGlp1r* $^{A316T/A316T}$ mice displayed similarly reduced acute responses to exendin-F1 when compared to *hGlp1r* $^{+/+}$ mice, this difference was absent at the 6 hour time-point, suggesting a higher beneficial impact of the reduced desensitisation afforded by this biased agonist[30] for the A316T variant-expressing mice (Fig. 1k). These effects were also apparent when calculated as vehicle fold changes (Extended Data Fig. 2c), with no significant differences in prolonged over acute effects for either agonist per genotype (Extended Data Fig. 2d,e). Similar experiments performed as above in heterozygous *hGlp1r* $^{A316T/+}$ mice showed no clear differences *versus* WT *hGlp1r* $^{+/+}$ littermates (Extended Data Fig. 2f-p).

Concurrently, plasma samples collected 10 minutes into the IPGTT assays showed higher insulin levels in *hGlp1r* $^{A316T/A316T}$ mice *versus* WT *hGlp1r* $^{+/+}$ littermates after vehicle administration, an effect that became significant for the 6 hour time-point (Fig. 1l,m). As expected, plasma insulin levels increased in response to exendin-4 administration for the WT *hGlp1r* $^{+/+}$ mice, but this effect was absent for *hGlp1r* $^{A316T/A316T}$. When expressed as vehicle fold changes, plasma insulin rises in response to exendin-4 were reduced for *hGlp1r* $^{A316T/A316T}$ mice *versus* WT *hGlp1r* $^{+/+}$ littermates, a difference that became significant at the 6 hour time-point (Fig. 1n).

We next analysed glycaemic responses in *hGlp1r* $^{A316T/A316T}$ *versus* WT *hGlp1r* $^{+/+}$ littermate control mice fed a HFHS diet for 12-14 weeks to investigate variant-associated phenotypes in a model of diet-induced metabolic stress and T2D. After 14 weeks of HFHS diet, *hGlp1r* $^{A316T/A316T}$ mice displayed lower weight gain compared to WT *hGlp1r* $^{+/+}$ littermates (Fig. 2a,b). Consistent with our prior results in lean conditions, oral glucose tolerance was significantly improved in *hGlp1r* $^{A316T/A316T}$ mice (Fig. 2c), but no changes were observed in fasting glycemia between genotypes (Fig. 2d). HFHS-fed *hGlp1r* $^{A316T/A316T}$ mice exhibited significantly enhanced glucose tolerance under vehicle conditions compared to *hGlp1r* $^{+/+}$ control mice,

both acutely and at the 6 hour time-point (Fig. 2e,f). Glucose responses to exendin-4 and exendin-F1 resembled those of WT *hGlp1r* $^{+/+}$ mice, but with slightly more pronounced desensitisation in both cases for *hGlp1r* $^{A316T/A316T}$ mice (Fig. 2g-j). Direct comparison between AUCs for the different conditions and genotypes analysed per time-point is shown in Extended Data Fig. 3a,b. When expressed as ΔAUC vehicle increases, the glucose-lowering effect of both GLP-1RAs was again significantly reduced in HFHS-fed *hGlp1r* $^{A316T/A316T}$ *versus* WT *hGlp1r* $^{+/+}$ littermates, with differences now apparent both acutely and 6 hours post-agonist administration for both exendin-4 and exendin-F1 (Fig. 2k,l). These effects were also apparent when calculated as vehicle fold changes (Extended Data Fig. 3c), with no significant differences in prolonged over acute effect for each agonist per genotype, as previously observed under lean conditions (Extended Data Fig. 3d,e). As in chow-fed conditions, basal plasma insulin levels were increased in *hGlp1r* $^{A316T/A316T}$ mice, an effect that was now significant acutely (Extended Data Fig. 3f).

To assess the effects of the A316T variant in response to a clinically relevant GLP-1RA, we conducted additional experiments in HFHS-fed animals treated with the long-acting GLP-1RA semaglutide[31]. We observed a similar profile of enhanced responses to vehicle alone at the 24 and 72 hour time-points in HFHS-fed *hGlp1r* $^{A316T/A316T}$ mice (Fig. 2m,n). Glucose responses to semaglutide were very similar to those of HFHS-fed *hGlp1r* $^{+/+}$ littermates at both time-points analysed, with slightly lower glucose curves for *hGlp1r* $^{A316T/A316T}$ mice but no significant AUC changes (Fig. 2o,p). Direct comparison between AUCs for the different conditions and genotypes analysed per time-point is shown in Extended Data Fig. 3g,h. ΔAUC vehicle increases showed worse glucose responses to semaglutide in *hGlp1r* $^{A316T/A316T}$ *versus* *hGlp1r* $^{+/+}$ littermate controls 24 hours post-agonist treatment, with these differences no longer apparent at the 72 hour time-point, when both genotypes displayed fully desensitised GLP-1R responses (Fig. 2q). As above, these effects were similarly apparent when calculated as vehicle fold changes (Extended Data Fig. 3i). This time, however, we observed a nearly significant reduction in prolonged over acute effects for semaglutide in *hGlp1r* $^{A316T/A316T}$ compared to *hGlp1r* $^{+/+}$ mice (Extended Data Fig. 3j), indicative of

faster GLP-1R desensitisation in response to semaglutide with the former genotype. Parallel experiments in HFHS-fed heterozygous *hGlp1r* $^{A316T/+}$ mice showed more attenuated differences *versus* WT *hGlp1r* $^{+/+}$ littermates for weight gain, oral glucose tolerance, fasting glucose, and acute *versus* 6-hour responses to vehicle, exendin-4 and exendin-F1 (Extended Data Fig. 4a-l), with the only significant effect being increased desensitisation in *hGlp1r* $^{A316T/+}$ mice 6 hours post-exendin-4 administration (Extended Data Fig. 4g,h). However, HFHS-fed heterozygous *hGlp1r* $^{A316T/+}$ mice exhibited improved glucose tolerance 24 hours post-vehicle administration (Extended Data Fig. 4m,n), but significantly worse ΔAUC glucose responses to semaglutide when compared to WT *hGlp1r* $^{+/+}$ littermates (Extended Data Fig. 4o-q), an effect that, as seen for exendin-4 administration in chow-fed mice, led to paradoxically higher glucose levels compared to those exhibited by vehicle-treated *hGlp1r* $^{A316T/+}$ mice (Extended Data Fig. 4q).

Alterations of islet cytoarchitecture and β-cell identity in human Glp1r $^{A316T/A316T}$ ***mice***

Previous studies have suggested that, due to its proliferative and anti-apoptotic effects, GLP-1R activity might lead to alterations in critical aspects of islet cytoarchitecture such as size, cellular composition, differentiation, and β-cell identity[32-35]. Changes in islet architecture have also been linked to β-cell dysfunction and T2D progression[36-39]. With the A316T variant conferring a GoF phenotype in glucose tolerance and plasma insulin levels in the absence of agonist stimulation, indicative of increased basal GLP-1R activity, we hypothesised that these effects might lead to changes in islet cytoarchitecture and β-cell identity in our humanised *Glp1r* knock-in mouse model. To test this hypothesis, we conducted histological examinations of pancreatic tissue and isolated islets from both chow- and HFHS-fed *hGlp1r* $^{A316T/A316T}$ and WT *hGlp1r* $^{+/+}$ control mice. Islets isolated from chow-fed *hGlp1r* $^{A316T/A316T}$ mice showed a non-significant tendency for increased numbers of insulin-positive and glucagon-positive cells, with no changes in the relative percentage for either cell type (Fig. 3a,b). Islets isolated from HFHS-fed *hGlp1r* $^{A316T/A316T}$ mice, however, displayed a remarkable increase in the number of glucagon-positive cells with no changes in insulin-positive cell numbers, leading to a significant increase in the percentage of

glucagon-positive cells, and a concomitant decrease in the percentage of insulin-positive cells *versus* WT *hGlp1r* $^{+/+}$ mouse islets (Fig. 3c,d). These results were mostly recapitulated in whole pancreas sections from each mouse type: while chow-fed mice did not show significant differences in β- or α-cell mass, α-to-β cell ratio, or islet diameter between genotypes (Fig. 3e-h), immunolabelling of pancreas sections from HFHS-fed *hGlp1r* $^{A316T/A316T}$ mice revealed increased α-cell mass, α-to-β-cell ratio, and islet diameter *versus* WT *hGlp1r* $^{+/+}$ controls (Fig. 3i-l). Interestingly, α-cells from HFHS-fed *hGlp1r* $^{A316T/A316T}$ mouse islets showed a distinct loss of their typical localisation to the islet periphery (the two outermost layers of cells in the islet), and were instead intermingled with β-cells throughout the islet core (Fig. 3m). Closer examination of intra-islet endocrine cell localisation revealed a significant proportion of non-peripheral cells expressing both insulin and glucagon (Fig. 3i, arrows), potentially indicating a compensatory α-to-β-cell trans-differentiation effect, as previously observed after GLP-1RA exposure[40-43], concomitant to an α-cell amplification effect in response to the HFHS challenge in *hGlp1r* $^{A316T/A316T}$ islets. α-cell heterogeneity has been previously observed in human islets under different conditions[44, 45]; analysis of expression of β-cell "enriched" and "disallowed" genes revealed an upregulation of genes associated with β-cell identity and function such as *Mafa* (with a tendency for increased expression of *Kcnj11* and *Ins1*) in islets isolated from both chow- and HFHS-fed *hGlp1r* $^{A316T/A316T}$ mice, with no changes observed in β-cell disallowed genes (*Slc16a1*, *Ldha*), but with a tendency for increased α-cell-specific *Gcg* expression (Extended Data Fig. 5a,b). Interestingly, expression of the β-cell disallowed gene *Acot7*[46] was significantly upregulated in chow-fed *hGlp1r* $^{A316T/A316T}$ mouse islets but not in islets from the same mice after prolonged HFHS feeding.

Changes in cell surface expression, agonist-induced cAMP generation and insulin secretion responses in islets from human Glp1r $^{A316T/A316T}$ ***mice***

Accounting for potential variations in cell surface expression of GLP-1R variants is crucial, as differences in this parameter can influence baseline receptor activity in β-cells and subsequent responses to GLP-

1RAs[28]. Of note, the humanised *Glp1r* mouse model employed in this study displays reduced levels of GLP-1R surface expression when compared to non-humanised mice expressing endogenous mouse *Glp1r* (Extended Data Fig. 5c,d), potentially due to *hGlp1r* being expressed as a mini-gene inserted in the murine *Glp1r* locus[29]. We therefore have restricted our comparisons to levels of surface expression in humanised *Glp1r* mice with the same genetic background to avoid any confounding effects. Islets extracted from both chow- and HFHS-fed *hGlp1r* $^{A316T/A316T}$ mice showed reduced surface GLP-1R levels *versus* WT *hGlp1r* $^{+/+}$ littermate control islets, assessed by labelling with the fluorescent GLP-1R antagonist exendin-9-TMR. Results were corroborated *in vivo* by subcutaneous injection of exendin-9-Cy5 (LUXendin645[2]) in living mice prior to transcardial fixation and pancreas tissue section analysis (Fig. 4a,b).

We next analysed acute cAMP responses in chow-fed *hGlp1r* $^{A316T/A316}$ *versus* WT *hGlp1r* $^{+/+}$ mouse islets transduced with the baculoviral cAMP fluorescent biosensor cADDis[47]. Results did not achieve statistical significance but showed a trend for reduced cAMP outputs in response to exendin-4 stimulation in *hGlp1r* $^{A316T/A316}$ islets, while, conversely, we measured a near-significant increase in cAMP response to the biased agonist exendin-F1 (Fig. 4c-e). *Ex vivo* insulin secretion assays from the same islets showed increased secretory outputs in response to both acute (30 minute) and sustained (16 hour, cumulative) exposure to 11 mM glucose for the *hGlp1r* $^{A316T/A316}$ genotype (Fig. 4f). Insulin secretion vehicle fold responses to both exendin-4 and exendin-F1 were however blunted in chow-fed *hGlp1r* $^{A316T/A316}$ *versus* *hGlp1r* $^{+/+}$ islets, with no measurable increases over vehicle detected following overnight exposure to exendin-4 (Fig. 4g). As observed in the *in vivo* studies, no significant differences were detected in prolonged over acute responses for either agonist *versus* WT *hGlp1r* $^{+/+}$ islets, despite a tendency for the bulk of the A316T variant effect to be present already acutely (Fig. 4h). Parallel experiments in islets from HFHS-fed *hGlp1r* $^{A316T/A316}$ *versus hGlp1r* $^{+/+}$ mice showed similar tendencies as in chow islets which, however, did not reach statistical significance (Extended Data Fig. 5e-g). Finally, secretion analysis after

24 hours of stimulation with the clinically relevant agonist semaglutide again showed increased insulin secretion in response to 11 mM glucose, but a significant decrease in the vehicle fold response to this long-acting agonist in *hGlp1r* $^{A316T/A316}$ islets from HFHS-fed mice (Fig. 4i,j).

Additional experiments were performed using islets from *hGlp1r* $^{-/-}$ mice, generated *in house* from the same *hGlp1r* $^{+/+}$ mouse line as above, transduced with adenoviral vectors expressing SNAP/FLAG-tagged WT or A316T hGLP-1R (pAV-SNAP/FLAG-*hGlp1r* ^{WT} or ^{A316T}). Using a membrane impermeable fluorescent SNAP tag probe, we again measured reduced surface expression of SNAP/FLAG-*hGlp1r* ^{A316T} compared to its WT counterpart (Extended Data Fig. 6a,b). Intracellular Ca^{2+} mobilisation, another downstream signalling readout of GLP-1R activation associated with insulin granule exocytosis, was also examined in this system using the fluorescent calcium indicator Cal-520 AM and time-lapse fluorescence microscopy. While we could not detect significant differences in calcium responses between SNAP/FLAG-*hGlp1r* ^{WT} and ^{A316T} for most GLP-1RAs investigated, we did find increased intracellular Ca^{2+} levels in *hGlp1r* $^{-/-}$ pAV-SNAP/FLAG-*hGlp1r* ^{A316T} islets following stimulation with exendin-F1 (Extended Data Fig. 6c-h), in line with our previous findings for cAMP signalling.

Impact of the A316T variant on primary human islets and a human β-cell line

Given the strong evidence from previous GWAS and HEK293 data[48], and our *in vivo* observations of the effect of the GLP-1R A316T variant on glucose homeostasis, we next investigated its impact on human β-cell models, including human donor islets and the well-characterised human β-cell line EndoC-βH3[49]. EndoC-βH3 cells were genetically modified by CRISPR/Cas9 to generate a *Glp1r* $^{-/-}$enriched multiclonal cell population, and then transduced with adenoviruses expressing SNAP/FLAG-*hGlp1r* ^{WT} or ^{A316T} as above. As for our previous findings, EndoC-βH3 *Glp1r* $^{-/-}$ SNAP/FLAG-*hGlp1r* ^{A316T} cells showed reduced GLP-1R cell surface expression (Fig. 5a,b), and similar insulin secretion profiles to the ones observed in *hGlp1r* $^{A316T/A316T}$ mouse islets, with enhanced basal insulin secretion but significantly reduced exendin-4-stimulated vehicle fold increases (Fig. 5c,d). Experiments were translated to primary human islets

transduced with SNAP/FLAG-*hGlp1r* ^{WT} or ^{A316T}-expressing adenoviruses as above, a system that would mimic a heterozygous phenotype for the A316T variant expression. Results again showed reduced surface expression of SNAP/FLAG-*hGlp1r* ^{A316T} *versus* ^{WT} islets (Fig. 5e,f), as well as a trend towards increased basal insulin secretion but reduced exendin-4 vehicle fold responses (Fig. 5g,h).

Modulation of GLP-1R trafficking by the A316T variant

Having characterised the functional effects of the A316T variant *in vivo* and *ex vivo*, we next explored the molecular mechanisms underlying the observed changes in GLP-1R cell surface expression and signalling. To do so, we employed an *in vitro* INS-1 832/3 rat β-cell model where endogenous GLP-1R expression is deleted by CRISPR/Cas9[50] to generate stable multiclonal lines expressing SNAP/FLAG-tagged WT or A316T human GLP-1R. Similarly to our previous findings, SNAP/FLAG-*hGlp1r* ^{A316T} cells showed reduced receptor surface expression *versus* its WT counterpart (Fig. 6a). Moreover, assessment of SNAP/FLAG-*hGlp1r* ^{wt} *versus* ^{A316T} expression by Western blotting, or with the cell-permeable SNAP-tag probe BG-OG[51], revealed significantly reduced total levels of the A316T variant compared to the WT receptor (Fig. 6b,c), suggesting increased basal degradation or reduced protein synthesis. To clarify the mechanism underlying this phenotype, we treated the cells from above with bafilomycin A1, an established vacuolar-type H^+-ATPase inhibitor that prevents lysosomal degradation[52]. Bafilomycin A1 exposure resulted in complete recovery of surface expression levels in INS-1 832/3 *Glp1r* $^{-/-}$ SNAP/FLAG-*hGlp1r* ^{A316T} cells, now comparable to WT controls (Fig. 6d). The same effect was observed using *hGlp1r* $^{-/-}$ islets transduced with SNAP/FLAG-*hGlp1r* ^{WT} *versus* ^{A316T} adenoviruses (Fig. 6e), or in islets purified from *hGlp1r* $^{+/+}$ *versus* $^{A316T/A316T}$ mice (Fig. 6f), indicating increased basal turnover and lysosomal degradation as the cause for the decrease in surface and total levels of the GLP-1R A316T variant. Next, we assessed GLP-1R trafficking behaviours in response to GLP-1RA stimulation in INS-1 832/3 *Glp1r* $^{-/-}$ SNAP/FLAG-*hGlp1r* ^{WT} and ^{A316T} cells by high-content microscopy assays. A316T GLP-1R internalisation was similar to that of WT receptor in response to exendin-4 and exendin-F1 but was significantly

increased following stimulation with the endogenous agonist GLP-1 (Fig. 6g, Extended Data Fig. 7a,b). A316T receptor recycling to the plasma membrane was again not different to WT with exendin-4 and exendin-F1, but was significantly reduced for GLP-1 (Fig. 6h, Extended Data Fig. 7c,d). Finally, receptor degradation was not significantly different between WT and A316T for any of the agonists tested (Fig. 6i, Extended Data Fig. 7e,f). Overall, the A316T variant receptor appeared to show a specific trafficking pattern in response to the endogenous agonist GLP-1, but very similar trafficking behaviours to WT receptors with exendin-4-derived agonists.

A316T-associated changes on GLP-1R coupling to $G\alpha_s$ and β-arrestin 2, and downstream signalling effects

We next explored changes associated with GLP-1R A316T capacity for $G\alpha_s$ and β-arrestin 2 coupling using NanoBiT complementation assays in INS-1 832/3 *Glp1r* $^{-/-}$ SNAP/FLAG-*hGlp1r* ^{WT} *versus* ^{A316T} cells. We first analysed mini-G_s and β-arrestin 2 recruitment to WT *versus* A316T variant receptors under vehicle conditions to evaluate changes in baseline coupling activity. The A316T GLP-1R demonstrated significantly increased basal mini-G_s, with no change in β-arrestin 2 recruitment compared to the WT receptor (Fig. 6j,k). For agonist-induced $G\alpha_s$ coupling, no significant changes *versus* WT receptors were found for A316T mini-G_s recruitment in response to GLP-1 or exendin-4, but we detected increased recruitment following stimulation with exendin-F1 (Fig. 6l, Extended Data Fig. 7g,h). Recruitment of β-arrestin 2 was again not significantly different for the A316T variant, besides a near-significant reduction again with exendin-F1 (Fig. 6m, Extended Data Fig. 7i,j). When both effects were combined to calculate β-arrestin 2 over $G\alpha_s$ recruitment bias, we found a significant shift towards $G\alpha_s$ recruitment for the A316T *versus* WT GLP-1R only when stimulated with exendin-F1 (Fig. 6n). Changes in GLP-1R cAMP outputs are often the result of combined trafficking and $G\alpha_s$ / β-arrestin 2 coupling effects. We therefore next analysed cAMP responses to the different GLP-1R agonists in INS-1 832/3 *Glp1r* $^{-/-}$ SNAP/FLAG-*hGlp1r* ^{WT} *versus* ^{A316T} cells. While we could not detect any significant changes, there was a tendency for

increased acute cAMP responses to GLP-1 and exendin-F1, reduced responses to exendin-4, and no change in response to semaglutide for the A316T *versus* the WT receptor (Extended Data, Fig. 7k-p).

We next used a previously described bystander NanoBiT assay, based on the recruitment of active $G\alpha_s$-binding nanobody 37 (nb37) to plasma membrane *versus* endosomal locations[53], to assess any possible effects of the A316T variant on subcellular receptor activity. Results showed a tendency for increased basal endosomal over plasma membrane activity of the A316T compared to the WT receptor (Extended Data Fig. 8a), with endosomal activity levels again showing a tendency to be increased following stimulation with GLP-1, with no change in plasma membrane activity (Extended Data Fig. 8b). We also tested potential changes in receptor conformational dynamics, using a TR-FRET assay that measures proximity between the receptor extracellular domain (ECD) and the plasma membrane as a surrogate marker for receptor ECD opening. While no changes were detected between WT and A316T GLP-1R under basal conditions (Extended Data Fig. 8c), significantly increased ECD opening was measured in response to GLP-1 stimulation (Extended Data Fig. 8d), indicative of a higher degree of GLP-1R activation, as determined from previous studies[8, 54, 55]. Further, we determined the impact of the A316T mutation on GLP-1R recruitment to plasma membrane lipid nanodomains, or lipid rafts, a preferential localisation for active GLP-1Rs prior to internalisation into endosomes[56]. In line with our previous findings of a higher level of constitutive receptor activity, the A316T variant presented with increased basal levels at lipid rafts (Extended Data Fig. 8e). Raft segregation fold responses were however not altered for A316T *versus* WT receptor following GLP-1 stimulation but were significantly reduced in response to exendin-4 stimulation (Extended Data Fig. 8f). Given the close association between lipid raft segregation, plasma membrane diffusion, and receptor clustering[56, 57], we next investigated potential changes in these parameters by Raster image correlation spectroscopy (RICS) analysis of INS-1 832/3 *Glp1r* $^{-/-}$ SNAP/FLAG-*hGlp1r* ^{WT} *versus* ^{A316T} cells. Results showed significantly reduced plasma membrane diffusion coefficients for A316T *versus* WT GLP-1R under vehicle conditions, an effect normally observed for the WT receptor following agonist stimulation[58], as also seen in the present study (Extended Data Fig.

8g-i). Lastly, we analysed changes in GLP-1R ubiquitination, a key post-translational modification (PTM) linked to changes in GLP-1R signalling and post-endocytic trafficking[59]. As previously seen[59], GLP-1R ubiquitination was apparent under vehicle conditions for both WT and A316T receptors. Exendin-4 stimulation led to a non-significant trend towards de-ubiquitination for the WT receptor, but instead triggered significantly increased ubiquitination of the A316T receptor (Extended Data Fig. 8j), a feature typically associated with receptor targeting to lysosomes for degradation[60].

To assess the effect of the GLP-1R A316T constitutive activity at a cellular level, we next performed a mass spectrometry-based interactome analysis in vehicle *versus* agonist- (GLP-1 and exendin-4) stimulated A316T GLP-1R using INS-1 832/3 *Glp1r* $^{-/-}$ SNAP/FLAG-*hGlp1r* ^{A316T} cells, in parallel with previously presented data for WT GLP-1R[61]. Interactome results showed global increased interactions with previously identified active GLP-1R partners for the A316T compared to WT GLP-1R under vehicle conditions (Extended Data Fig. 9). Stimulation of GLP-1R A316T with either GLP-1 or exendin-4 led to further increases in interaction for most GLP-1R-binding factors, but notably lead to loss of receptor binding to certain specific interacting proteins, including, notably, VAP-B and SPHKAP, GLP-1R binding partners for which we have recently identified a critical role in the control of mitochondrial function downstream of GLP-1RA stimulation[61].

Structural determination of the GLP-1R A316T variant

To elucidate structural changes associated with the A316T variant receptor, the GLP-1-bound cryo-EM structure of GLP-1R A316T in complex with dominant negative (DN) $G\alpha_s$ was resolved to a 3.3 Å resolution (Fig. 7a). In general, the complex was well resolved and amino acid side chains reasonably modelled for almost the entire structure. However, the α-helical domain of DN-$G\alpha_s$, the flexible ECD, extracellular loop 3 (ECL3) and intracellular loop 3 (ICL3) of GLP-1R A316T, as well as the final two C-terminal residues of GLP-1, were more poorly defined, in line with the intrinsic flexibility of these regions. The overall positioning of the transmembrane domains (TMDs) was extremely similar to the WT receptor

(Fig. 7b), and the binding arrangement of GLP-1 was essentially identical to that previously reported by high-resolution cryo-EM[54]. Broadly, the C-terminus of the peptide is cradled by the ECD and ECL1/2 of GLP-1R and oriented intracellularly at a steep angle (Fig. 7b). Rich contacts along the inward face of the receptor TMDs guide the N-terminus of GLP-1 deep into the orthosteric site, where it makes critical contacts with the conserved central polar network, including a salt bridge with R190$^{2.60}$. These interactions were preserved when bound to GLP-1R A316T (Fig. 7c). A network of structural waters connects the central parts of TM3, 5 and 6, likely forming hydrogen bonds (HBs) with the backbone, including the highly conserved G361$^{6.50}$ from the P$^{6.47}$xxG$^{6.50}$ motif[54], which is crucial for facilitating receptor activation and transducer coupling. In WT GLP-1R, the backbone carbonyl of Y241$^{3.44}$, part of the conserved central polar network, directly interfaces with this network through a HB with a structural water that sits between TM3 and TM5 (Fig. 7d). This water is also within HB distance of the backbone carbonyl of A316$^{5.42}$ and may contribute to the interhelical packing and stiffness. In the T316 variant cryo-EM structure, this backbone carbonyl is displaced around 1.5 Å away from the position of this structural water (Fig. 7d). While the orientation of the hydrogens for this water is unknown, the T316 backbone carbonyl has a shallower angle, poorly favourable for any possible hydrogen bonding compared to A316. Intriguingly, when modelled as the 'upwards' rotamer, the hydroxyl group of T316 could HB with the oxygen of this structural water, but this rotamer position would likely preclude the known interactions discussed above. The interface between GLP-1R and Gα_s is highly conserved with other class B1 GPCRs[62], and the interactions formed by GLP-1R A316T with the α5 helix of Gα_s are very similar to those found in WT GLP-1R agonist-bound structures[54] (Fig. 7e,f). Higher resolution structures of agonist-bound GLP-1R in complex with Gα_s have uncovered important structural waters in this region, including a water molecule acting as a key bridge between E247$^{3.50}$, highly conserved and part of the HETX motif, and Y391$^{G\alpha s}$. At this resolution, these waters are not present in the density map. The density for E247$^{3.50}$ was quite poor compared to neighbouring residues of similar size, which is not unusual for an acidic residue in single-particle cryo-EM at this resolution. N338^{ICL3} was also poorly resolved, indicating that it is comparatively

mobile (Fig. 7g, left graph). Compared to the WT GLP-1R, the position of R176$^{2.46}$ is rotated closer towards the α5 helix of Gα$_s$ by 2 Å and, independently, H387 is rotated slightly from its position in the WT GLP-1R structure (Fig. 7g, right graph). Overall, these are subtle differences that may contribute to the altered Gα$_s$ recruitment sometimes observed with this mutant[23, 26], but are not a 'smoking gun'. In summary, the static model built into the consensus density map of the GLP-1:GLP-1R (A316T):DN-Gα$_s$:nb35 complex, while largely similar to the WT receptor, suggests changes to key water-mediated interactions between TM5 and its neighbouring helices which could alter the dynamics of the TMD. Additionally, subtle changes to interactions between the intracellular face of the receptor and the α5 helix of DN-Gα$_s$ were found, which may correlate with the pharmacological profile of the A316T variant.

To explore these observations further, 3D variability analysis (3DVA) in cryoSPARC 3.2, with a 3-principal component analysis (PCA) model, was employed on the particles used in the consensus refinement. 3DVA, as implemented in the cryoSPARC software, is a powerful tool for examining conformational heterogeneity in cryo-EM datasets[63]. These data were analysed by a PCA model searching for 3 principal components with a tight mask around the receptor and G proteins to exclude variability from the detergent micelle. Previous analyses of GLP-1R cryo-EM structures with peptide ligands have demonstrated 3 major modes of motion: a coordinated twisting movement of the receptor TMD; a large oscillation of the peptide C-terminus and ECD; and a twisting/rocking of the receptor and G protein[54]. Unexpectedly, a striking increase in variability for ECL3 in GLP-1R A316T, compared to the WT receptor, was observed in all three principal components, and preserved at low contour. This motion was particularly evident in principal component 3 (Fig. 7h) and was accompanied by more extreme movements in TM6 and the N-terminal half of the peptide. Compared to 3DVA of the GLP-1R WT, GLP-1R A316T TM6-ECL3-TM7 underwent a larger motion down and away from the receptor core (Fig. 7h).

Molecular dynamics (MD) simulations of WT versus A316T GLP-1R: impact of the A316T SNP on receptor dynamics, structural water molecules, and HB interactions

To retrieve atomistic insights about the effect of the A316T substitution on the structure and dynamics of the GLP-1R, A316T and WT GLP-1Rs were simulated in three different configurations: i) the isolated TMD in the absence of any agonist; ii) in complex with the endogenous agonist GLP-1 (i.e., the new A316T cryo-EM structure presented here and the PDB 6X18); and iii) in complex with exendin-F1 and $G\alpha_s$ (i.e., the WT cryo-EM structure and a modelled A316T structure based on the former). The side chain of $T316^{5.46}$ (A316T) formed a HB with $Y242^{3.45}$, not present in the WT GLP-1R, where $Y242^{3.45}$ interacted with the $P312^{5.42}$ backbone instead. This HB reshuffling (Supplementary Table 5) was more evident in the isolated TMD in the absence of any agonist, where the $Y242^{3.45}$ - $P312^{5.42}$ HB persistency dropped from 95.2% (WT) to 2.2% (A316T), than in GLP-1R in complex with GLP-1 (from 93.3% down to 46.1%) and in GLP-1R in complex with exendin-F1 and $G\alpha_s$ (from 87.4% to 7.9%). This suggests that $Y242^{3.45}$ engages the hydrophilic $T316^{5.46}$ side chain instead of the $P312^{5.42}$ backbone in a ligand-dependent manner. Indeed, the $Y242^{3.45}$ - $T316^{5.46}$ HB was very persistent in the isolated TMD (85%), while in GLP-1R in complex with either GLP-1 or with exendin-F1 and $G\alpha_s$, it was less persistent but still present for more than one third of the simulations (41.8% and 37.7%, respectively). The reason for the $Y242^{3.45}$ - $T316^{5.46}$ HB strength in the isolated TMD lies in the rotameric state of $T316^{5.46}$ being blocked in the configuration prone to accept the HB from $Y242^{3.45}$ and donate the hydrogen to the $P312^{5.42}$ backbone (State 1 in Fig. 8a, Supplementary Table 5). For GLP-1R in complex with GLP-1, the T316 side chain flipped between the rotameric State 1 and another conformation able to form a HB with the backbone of $I313^{5.43}$ and a water bridge with the $Y241^{3.44}$ backbone (State 2 in Fig. 8b, Supplementary Tables 5 and 6). The HB reshuffling is consistent with our previous MD simulations of oxyntomodulin and $G\alpha_s$-complexed GLP-1R[64], where the $Y242^{3.45}$ - $P312^{5.42}$ HB in the WT (occupancy 88.9%) was replaced by the $Y242^{3.45}$ - $T316^{5.46}$ HB in A316T (62.3%) due to a consistent rotameric State 1 throughout the simulations, corroborating an allosteric effect of the agonist in the $T316^{5.46}$ dynamics and, in turn, $Y242^{3.45}$ - $T316^{5.46}$ HB. A double rotameric state for $T316^{5.46}$ is confirmed by our cryo-EM maps, able to accommodate both an “upward” and a “downward” side-chain orientation.

T316$^{5.46}$ (A316T) in the rotameric State 2 weakly interacted with the conserved N320$^{5.50}$ through a water bridge (Fig. 8b, Supplementary Table 6). A detailed analysis of the interaction involving N320$^{5.50}$ (Supplementary Table 7) reveals a stable direct HB with the backbone of L360$^{6.49}$ at the TM6 kink level in the 3 WT GLP-1R configurations (occupancy 68.5%, 79.6%, and 65.4%, respectively). This N320$^{5.50}$ - L360$^{6.49}$ HB is weakened in A316T when in complex with the endogenous agonist GLP-1 (35.6%) and for the isolated TMD (30.6%), and only slightly reduced in the case of A316T in complex with exendin-F1 and Gα_s (54.8%). The diminished HB strength is counterbalanced by an increase in water-mediated interactions between N320$^{5.50}$ and L360$^{6.49}$, as well as between N320$^{5.50}$ and G361$^{6.50}$, in A316T in complex with the endogenous agonist GLP-1 (from 12.2% to 26.8%) and in the isolated TMD (from 19.5% to 49.3%). Such water-mediated interactions involving N320$^{5.50}$ characterising A316T were due to a deeper water molecule permeation in the polar core of the receptor compared to WT GLP-1R (Fig. 8c-h), where they were stabilised by a concerted effect of the polar side chain of T316$^{5.46}$ and the presence of the agonist. Indeed, a significant increase in the water molecule residence time (up to 15% ca.) was observed in A316T in complex with GLP-1 or in complex with exendin-F1 and Gα_s (Supplementary Table 8) but not in the isolated TMD, where the water was exchanged with bulk solvent instead of being stabilised into structural water molecules, as occurring in the agonist-complexed A316T configurations.

To retrieve further insights into the allosteric effect of the persistent Y242$^{3.45}$ - T316$^{5.46}$ HB formed by T316$^{5.46}$ in the rotameric State 1, we further analysed the MD simulations involving the isolated TMD of GLP-1R. We reasoned that the GLP-1R structure other than the TMD (i.e. ECD and ECL1), or the binders GLP-1 and Gα_s, can either directly (i.e., GLP-1, Gα_s) or allosterically (i.e., ECD, ECL1) influence the possible conformations that the TMD adopts because of the A316T mutation, *de facto* shielding any subtle allosteric effects. The Y242$^{3.45}$ - T316$^{5.46}$ HB in A316T moved TM3 and TM5 away from each other, as shown by the increased backbone distance between the closely downstream residues L245$^{3.48}$ - V319$^{5.49}$ (Extended Data Fig. 10b,c). This is consistent with our cryo-EM maps of A316T in complex with GLP-1

and $G\alpha_s$, where the bulkier T316$^{5.46}$ side chain sterically displaces the T316$^{5.46}$ backbone carbonyl by approximately 1.5 Å away from the interhelical space compared to the WT A316$^{5.46}$. Structural contractions or expansions at the extracellular or intracellular side of a GPCR can allosterically influence the receptor dynamics at the opposite side[65]. Consistent with this GPCR structural effect, the TM3-TM5 intracellular distance in A316T, measured at the L251$^{3.54}$ - V327$^{5.57}$ level, shortened by ~1 Å (Extended Data Fig. 10b,c), favoured by a more persistent HB between Y252$^{3.55}$ and R326$^{5.56}$ (occupancy 35.7% in A316T *versus* 11.4% in WT). In concert with the TM3-TM5 intracellular contraction, the TM6 outwards opening, a structural hallmark of GPCR activation to accommodate the $G\alpha_s$ protein, was about 2.5 Å wider in A316T than in WT GLP-1R (Extended Data Fig. 10d). However, the TM6 wider opening in the isolated TMD of A316T was not observed when A316T was in complex with GLP-1, suggesting that the agonist can modulate the TM3-TM5 distance by influencing the rotameric state of T316 and in turn the formation of the Y242$^{3.45}$ -T316$^{5.46}$ HB.

Discussion

GPCRs are well known to harbour SNPs, leading to phenotypic variability amongst individuals potentially impacting pharmacological responses and disease traits[66]. Despite the importance of GLP-1R as a major T2D and obesity drug target, and the known variability of responses to GLP-1RAs amongst individuals taking this class of drugs[67], there is surprisingly little research on the functional consequences of *Glp1r* genetic variants associated with glycaemic traits and human metabolic diseases, particularly using *in vivo* models. Although most *Glp1r* variants are low-frequency mutations, understanding their phenotypes and associated pathophysiological changes in humans is valuable as a basis for the development of personalised therapeutic strategies, particularly when considering the large number of individuals affected by GLP-1R-related diseases. The current study has attempted to bridge this gap by employing a CRISPR/Cas9-based approach to generate a humanised knock-in mouse line bearing the A316T mutation in the human *Glp1r* locus in conjunction with *in silico*, *ex vivo*, and *in vitro* approaches to

understand the association of the rs10305492 G>A variant with T2D protection. Although this missense variant has been previously studied *in vitro*, previous analyses using HEK293T, CHO or INS-1 cell lines[23, 26, 28, 68] have not provided a comprehensive mechanistic explanation for its functional effects, and no data is available in primary tissues or *in vivo*. Here, our *in vivo* model exhibits improved oral glucose tolerance under both chow and HFHS diet conditions, suggesting enhanced sensitivity to endogenous GLP-1, as well as significantly lower fasting glucose levels in the chow-fed state, in agreement with the reported effects of the A316T variant in human GWAS studies[21-23]. Interestingly, the variant also exhibits slower weight gain in diet-induced obese mice, suggesting a protective effect on the development of obesity, measurable here despite the reduced human *Glp1r* expression levels in our humanised mouse model compared to non-humanised mice, which could have precluded the observation of brain-specific receptor effects, a location where the receptor is typically modestly expressed. We have therefore likely underestimated the anorectic effect of the A316T variant in this study, and this phenotype warrants additional investigations outside of the scope of the present study.

Despite the positive effect of the A316T variant on glucose homeostasis and endogenous GLP-1 responses, it also presented with reduced responses to pharmacological GLP-1RAs when these were assessed relative to the variant effect under vehicle conditions. Not all agonists were equally affected, with exendin-4 responses being particularly hampered, to the point of causing a relative increase in blood glucose levels *versus* vehicle exposure at the 6 hour time-point in chow-fed A316T mice, suggesting a detrimental impact on glucoregulation under those conditions, while exendin-F1, a $G\alpha_s$-biased analogue of exendin-4, retained its beneficial effect 6 hours post-agonist administration despite an initial acute effect loss in chow-fed homozygous A316T *versus* WT *hGLP1r* mice. These *in vivo* effects correlate with increases in plasma insulin levels in both lean and obese A316T mice following vehicle administration, likely due to increased constitutive GLP-1R activity mimicking agonist-induced effects in the pancreas, without concomitant increases in insulin levels in response to exendin-4 administration. We have also

established the clinical relevance of our observations, as the currently leading pharmacological GLP-1RA, semaglutide, triggers similarly reduced responses in HFHS-fed *hGLP1r* $^{A316T/A316T}$ mice, an effect that is also present in heterozygous *hGLP1r* $^{A316T/+}$ mice, the most likely presentation of this variant due to its low frequency in human populations.

In addition to the *in vivo* study, we have also performed *ex vivo* analyses of the effects of the A316T variant on islet gene expression, morphology, and α- *versus* β-cell mass. While effects were relatively mild in islets from chow-fed mice, we observed increased islet diameter and a striking accumulation of α-cells in HFHS-fed *hGLP1r* $^{A316T/A316T}$ mouse islets, with these cells distributed across the islet core instead of being restricted to the islet mantle under these metabolic stress conditions. Furthermore, we observed the existence of bi-hormonal cells expressing both insulin and glucagon, the presence of which has been previously associated with human islet responses to GLP1RA treatment[40, 69]. High-fat diet feeding and metabolic stress have previously been shown to induce β-cell-like features in a subset of α-cells, and an increase in α-cell-derived GLP-1 secretion[44, 70]. While the reason for our observation remains unclear, it is possible that a compensatory mechanism might take place in the HFHS diet-exposed islets expressing A316T GLP-1R, resulting in an abnormal accumulation of both α- and bi-hormonal cells which could potentially modify intra-islet paracrine signalling. However, despite these changes in islet morphology, we only observed mild increases in the expression of β-cell enriched genes such as *MafA*, and a tendency for increased expression of *Ins1* and *Gcg* in *hGLP1r* $^{A316T/A316T}$ islets under HFHS-fed conditions.

To further understand the mechanisms underlying the changes in glucoregulation observed with the GLP-1R A316T variant, we have assessed levels of receptor cell surface expression, cAMP production and insulin secretion in *hGLP1r* $^{+/+}$ *versus* $^{A316T/A316T}$ islets. In agreement with previous *in vitro* observations[28, 71], we detected a significant reduction in cell surface expression of the A316T variant, both when measured *ex vivo* as well as *in vivo* by injecting the LUXendin645 probe into living mice. This reduced cell surface expression has been corroborated throughout this study in all other systems tested, including

human EndoC-βH3 *hGlp1r* $^{-/-}$ cells, human islets and islets from *hGlp1r* $^{-/-}$ mice transduced with adenoviral vectors expressing pAV-SNAP/FLAG-*hGlp1r* ^{WT} or ^{A316T}, as well as in INS-1 832/3 *hGlp1r* $^{-/-}$ cells stably expressing the WT or A316T human GLP-1R variant. We have also established here that this effect is due to an increased rate of receptor turnover, involving increased endocytosis and lysosomal targeting of the A316T variant GLP-1R under basal conditions, in keeping with a higher degree of constitutive activity conferred by the A316T mutation. Further indications of this effect include increased levels of constitutive recruitment to lipid rafts and reduced levels of basal receptor plasma membrane diffusion rates for the A316T GLP-1R, both typically observed for WT GLP-1Rs following agonist-induced activation[57, 72], and therefore indicative of a higher degree of constitutive activity of the variant receptor.

In this study, we have also detected enhanced levels of glucose-stimulated insulin secretion triggered by the A316T variant in the various *ex vivo* and *in vitro* human and mouse islet and β-cell models tested, which, in agreement with our *in vivo* results, does not translate to concomitant increases in insulin secretion in response to any of the GLP-1RAs tested. Overnight exendin-4-fold responses were particularly affected, a result that tightly correlates with the *in vivo* loss of glucoregulatory benefit, which progresses to a detrimental effect resulting in increased plasma glucose levels *versus* vehicle conditions when assessed 6 hours post-exendin-4 administration. Conversely, measures of cAMP production or intracellular Ca^{2+} in response to the $G\alpha_s$-biased analogue exendin-F1 showed some degree of improvement in A316T compared to WT GLP-1R-expressing islets, which correlates with a milder impairment in glucoregulation, particularly at prolonged time points, with this GLP-1RA. We hypothesise that this effect might be linked to the favourable trafficking profile of this biased GLP-1RA, enabling it to counteract the accelerated desensitisation propensity of the A316T variant receptor, a feature likely exacerbated by a fast internalising, slow recycling agonist such as exendin-4[30]. This effect also correlates with the enhanced exendin-4-induced ubiquitination of A316T *versus* WT GLP-1R, a PTM traditionally linked to a higher degree of desensitisation associated with lysosomal targeting and degradation[60].

Alternatively, the milder phenotype associated with exendin-F1 might be explained by concerted ECL3 conformational changes occurring in both the A316T, as seen by our 3DVA on the GLP-1R A316T structure, and with exendin-F1 binding[27, 73-76], which may result in beneficial additive effects with this agonist.

As the variant is associated with structural changes in residue networks that may influence its capacity for $G\alpha_s$ and β-arrestin 2 recruitment and binding, we used NanoBiT complementation assays previously established in our group[57] to assess basal and agonist-induced recruitment of these downstream signalling mediators to the WT *versus* the A316T GLP-1R. These experiments revealed enhanced basal mini-G_s recruitment but no change in basal β-arrestin 2 association for the variant receptor, despite the observed increased endocytosis and lysosomal targeting of the A316T variant GLP-1R under vehicle conditions. These results corroborate our previous finding that, despite its apparent correlation, β-arrestin 2 is not required for GLP-1R internalisation[77]. On the other hand, changes in agonist-induced recruitment of either factor *versus* WT GLP-1Rs were modest, with a mild increase in mini-G_s recruitment as well as a tendency for reduced β-arrestin 2 recruitment observed for A316T in response only to exendin-F1 stimulation. A calculation of bias between these two factors showed a significant exacerbation of $G\alpha_s$ *versus* β-arrestin 2 bias for the variant receptor when stimulated with exendin-F1, an agonist that is already inherently $G\alpha_s$-biased[30], adding to the list of subtle improvements detected with this agonist at the A316T receptor which might underlie its capacity for sustained glucoregulation comparably to that of the WT receptor, at least under the non-metabolically stressed conditions of chow feeding. Additional measurements of spatially resolved receptor activity using an assay to detect nb37 recruitment to plasma membrane or endosomes[53] demonstrated a tendency for increased endosomal signalling from the A316T GLP-1R when stimulated with the endogenous agonist GLP-1, an observation that correlates with the increased internalisation and reduced recycling for the variant *versus* WT receptor when stimulated with

this agonist. This is accompanied by a higher degree of receptor ECD opening and might be behind the improved oral glucose responses detected *in vivo* with the A316T variant.

Lastly, β-cell protein-protein interactome studies for the A316T GLP-1R also corroborated the increased inherent activity of the variant receptor, with a marked enrichment in interactions under vehicle conditions compared to the WT GLP-1R. Agonist stimulation of A316T GLP-1R triggered further increased binding to most interacting partners, with a few exemptions, which interestingly include VAP-B and SPHKAP, an ER-resident membrane contact site (MCS) factor[78] and a PKA anchoring protein (AKAP)[79], respectively, recently shown by our group to act concertedly to engage active GLP-1R signalling at ER-mitochondria MCSs leading to GLP-1RA-mediated mitochondrial remodelling[61]. Whether the A316T variant receptor has modified capacity to trigger signalling in this specific ER-mitochondrial cAMP/PKA nanodomain and therefore modulate mitochondrial remodelling and function distinctively from the WT receptor remains to be established. Also interestingly, binding to SUMO1, one of the paralog peptides attached to lysines in the process of sumoylation[80], is reduced upon agonist stimulation for the WT receptor, but increased *versus* vehicle conditions for the variant GLP-1R A316T, a pattern that coincides with that of the closely related PTM ubiquitination, as previously discussed, suggesting differences in the regulation of GLP-1R PTMs which might play an important role in the identified changes in trafficking and signalling of the variant receptor.

Further structural insights are provided here by the cryo-EM structure of the GLP-1R A316T variant in complex with $G\alpha_s$ and GLP-1, with a static atomic model similar to the WT GLP-1R, but with subtle changes to interactions between TM3, 5 and 6. It has previously been proposed, using the X-ray crystal structure of exendin-4-bound GLP-1R as a model, that the A316T variant disrupts hydrogen bonding between $N320^{5.50}$ and $E364^{6.53}$ by the formation of a direct interaction between $E364^{6.53}$ and $T316^{21}$. However, the cryo-EM structure of the GLP-1-bound A316T receptor obtained in this study does not exhibit these structural changes, instead suggesting, as supported by our MD simulations, a potential

disruption to central polar network residues via subtle alterations in the interhelical water network bridging TM5 and 6. Additionally, consistent with the mechanism suggested by the MD simulations, the GLP-1-bound GLP-1R A316T cryo-EM structure offers support for the disruption of interactions between Y242$^{3.45}$ and P312$^{5.42}$ in favour of the Y242$^{3.45}$ - T316$^{5.46}$ HB selective for a specific T316$^{5.46}$ rotameric state. Interestingly, 3D variability analyses of the GLP-1R A316T structure were suggestive of greater mobility in the extracellular loops of the variant receptor, particularly in ECL3, compared to the WT receptor bound to the same agonist[74, 81]. If this region is truly more dynamic in the A316T variant, it is conceivable that GLP-1 peptide cycling (disengagement and re-engagement) with the receptor could be faster, leading to more signalling events per unit time than for the WT GLP-1R. These observations are subject to certain limitations, including the modest resolution of the A316T variant structure (3.3 Å), which allows for confident placement of the receptor TMD side chains but is well below the resolution required to place structural waters implicated in the proposed mechanism of constitutive activity for this variant. In this regard, MD simulations are a useful tool to study water molecules within biological systems with good reliability[82]. In this study, they aided in pinpointing a water network involved in the communication between TM5 and TM6 of A316T, possibly contributing to the unique A316T pharmacology. Besides, simulations also suggested an allosteric mechanism triggered by Y242$^{3.45}$ - T316$^{5.46}$ HB, transmitted to the intracellular receptor side, and altering TM6 mobility in the apo-state A316T. Higher resolution structures would be required to understand the structural changes underlying A316T constitutive activation. As of yet, there are no other structures of known constitutively active GLP-1R mutants, making it difficult to conclude whether the potential differences in water network interactions and extracellular loop dynamics suggested by the present structure would be sufficient to account for the A316T constitutive activity. Our findings additionally suggest that the source of the enhanced activity of the A316T GLP-1R is the receptor itself rather than being triggered by ligand binding. Hence, apo-state structures would need to be obtained to elucidate the structural changes of the variant compared to the WT receptor, which itself has not been resolved.

When taken together, MD simulations aligned with cryo-EM data suggest a concerted mechanism that enhances A316T activation in the absence of bound agonist, triggered by the bulkier, more polar Thr316 side chain. The cryo-EM and MD simulations-informed structural model for the effect of the Ala to Thr substitution in position 316 (Extended Data Fig. 10e) suggests an allosteric effect between TM3 and TM5 triggered at position 316 and transmitted to the intracellular side of GLP-1R. A stabilising effect of water molecules on the TM6 kink, in concert with the intracellular closing up between TM3 and TM5, aids the intracellular opening movement of TM6, pivotal for $G\alpha_s$ recruitment and activation. In physiological thermal conditions, this allosteric effect would move the inactive-active A316T equilibrium towards the active state, favouring the constitutive activation of the receptor and $G\alpha_s$ coupling.

To conclude, we present here a comprehensive assessment of the effects of the A316T missense mutation in human and murine pancreatic β-cells, primary islets and *in vivo* using a genetically engineered humanised knock-in mouse model, including both agonist-dependent and -independent responses. We demonstrate *in vivo* increased basal but reduced agonist-dependent glucoregulatory effects, also present in islet insulin secretion assessments, correlating with *ex vivo* and *in vitro* signalling responses. Our study analyses in detail the agonist-dependent and -independent trafficking and signalling of this variant in physiologically relevant β-cell systems, confirming results from previous studies, including a marked GoF phenotype for the A316T missense mutation, were it adopts an intermediate state of activity in the absence of ligand, leading to reduced cell surface expression due to increased basal turnover, but with varying effects on G protein coupling and receptor trafficking responses to agonist stimulation (see Supplementary Table 9 for a summary of the main results of the study). These data have important implications for the design of future GLP-1R agonists and precision medicine approaches, whereby structural residue-residue interactions could be emulated to achieve allosteric effects similar to those of the A316T variant, and individuals could be prescribed specific GLP-1RAs based on their GLP-1R variant profile.

Methods

Peptides, plasmids, and reagents

GLP-1(7-36)NH_2 was purchased from Bachem; semaglutide was obtained from Imperial College London Healthcare NHS Trust pharmacy; exendin-4 and exendin-F1 were custom synthesized by Wuxi AppTec/Insight Biotechnology and were at least 95% pure. Tetramethylrhodamine (TMR)-labelled exendin-9 and exendin-4 (exendin-9-TMR and exendin-4-TMR) have been described and validated before[83, 84]. Exendin-9-Cy5 (LUXendin645) has been described before[85] and is a kind gift from Prof David Hodson (Oxford Centre for Diabetes, Endocrinology and Metabolism, UK). SNAP-Surface fluorescent probes were purchased from New England Biolabs. Surface cleavable BG-S-S-649[86-88] was a gift of Dr Ivan Corrêa Jr, New England Biolabs. LgBiT-mini-G_s[89] was a gift from Prof Nevin Lambert (Augusta University, USA). LgBiT-β-arrestin 2[59, 90] was purchased from Promega. pSNAP/FLAG-tagged human *Glp1r* (*hGlp1r*) ^{A316T} and *hGlp1r* ^{A316T}-SmBiT constructs were generated *in house* by site-directed mutagenesis from pSNAP/FLAG-*hGlp1r* ^{wt} (Revvity) and *hGlp1r* ^{WT}-SmBiT[59] with the following primers: Forward 5'-CCGGCTGCCCATTCTCTTTACCATTGGGG-3', and Reverse 5'-ACCCCAATGGTAAAGAGAATGGGCAGCCG-3' for pSNAP/FLAG-*hGlp1r* ^{A316T}; Forward 5'-CCGGCTGCCCATTCTCTTTACCATTGGGG-3', and Reverse 5'-ACCCCAATGGTAAAGAGAATGGGCAGCCG-3' for *hGlp1r* ^{A316T}-SmBiT, using the QuikChange Site-Directed Mutagenesis Kit (Agilent) following the manufacturer's instructions.

Animal studies

All animal procedures were approved by the British Home Office under the UK animals (Scientific Procedures) Act 1986 (Project License number PP7151519 to Dr A. Martinez-Sanchez, Imperial College London, UK) and from the local ethical committee (Animal Welfare and Ethics Review Board) at the Central Biological Services unit of Imperial College London. Animals were housed in groups of up to four adult mice in individually ventilated cages under controlled conditions at 21-23°C with 12h:12h light to

dark cycles (lights on at 07:00). Ad libitum access to water and feed was provided unless otherwise stated. Lean mice were fed a standard chow diet [RM1 (E); Special Diet Services]. For high-fat high-sucrose (HFHS) diet studies, animals were put on a 58 kcal % fat and sucrose diet (D12331, Research Diets, Inc.) ad libitum for 12-14 weeks prior to experiments.

Generation of hGlp1r $^{A316T/A316T}$ and hGlp1r $^{-/-}$ mice

Transgenic mice were generated on a C57BL/6 *hGlp1r* $^{+/+}$ mouse background from Taconic Artemis GmbH that has been described before[29]. To generate mice with the *hGlp1r* A316T mutation, one-cell stage *hGlp1r* $^{+/+}$ embryos were electroporated with 100 µL Opti-MEM (Thermo Fisher Scientific) containing ribonucleoprotein (RNP) complexes of *S. pyogenes* Cas9 (1.2 µM Alt-R® *S.p.* Cas9 nuclease 3NLS) with 6 µM single guide RNA (sgRNA) and donor single-stranded repair oligo DNA nucleotides (ssODNs, 300 ng/µL) using the NEPA21 electroporator (NEPA GENE Co. Ltd.) DNA nucleotides, *S.p.* Cas9 nuclease and sgRNA were purchased from Integrated DNA Technologies. The sgRNA used to introduce the Ala316 to Thr mutation was 5'-GCCCATTCTCTTTGCCATTG-3', designed using RGEN tool (http://www.rgenome.net/cas-designer/), targeting a sequence in exon 9 of *hGlp1r* flanking the rs10305492 single nucleotide polymorphism (SNP). The donor ssODNs used in this study are: Forward 5'-CATGAACTACTGGCTCATTATCCGGCTGCCCATTCTCTTTACCATTGGGGTGAACTTCCTCATCTTTGTTCGGGTCATCTGCAT-3', and Reverse 3'-ATGCAGATGACCCGAACAAAGATGAGGAAGTTCACCCCAATGGTAAAGAGAATGGGCAGCCGGATAATGAGCCAGTAGTTCATG-5', designed using the Alt-R CRISPR HDR design tool (https://eu.idtdna.com/pages/tools/alt-r-crispr-hdr-design-tool/) with the same target sequence as for the sgRNA (Extended Data Fig. 1a). Following electroporation, two-cell stage embryos were placed into oviducts of pseudo-pregnant *hGlp1r* $^{+/+}$ foster mothers to generate the F0 founder mice, which were subsequently screened for the presence of the A316T substitution as described below (Extended Data

Fig. 1b). Mice with frameshift disruptions of *hGlp1r* were also selected from F0 to establish a *hGlp1r* $^{-/-}$ mouse colony.

Genomic DNA extraction and genotyping

To genotype the transgenic mice, ear samples were collected from weaned animals and genomic DNA extracted in alkaline lysis buffer (25 mM NaOH, 0.2 mM EDTA, pH 8.0) for 1 hour at 95°C and subsequently neutralised by addition of 13 mM Tris-HCl (pH 7.4)[59]. The purified genomic DNA was used as a template for PCR with appropriate primers prior to Sanger sequencing to identify the A316T mutation. The genotyping primers are described in Supplementary Table 1.

Oral glucose tolerance tests (OGTTs) and intraperitoneal glucose tolerance tests (IPGTTs)

For OGTTs, chow or HFHS fed *hGlp1r* $^{A316T/A316T}$ mice and littermate controls were fasted for 5 hours, and blood glucose levels serially assessed at 0, 10, 30, and 60 minutes via tail venipuncture using a handheld glucometer (Accu-Chek), after administration of a glucose challenge (2 g/kg of body weight) into the gut by oral gavage. To examine acute and prolonged glycaemic responses to GLP-1R agonists (GLP-1RAs), animals were fasted for 2 hours, starting at 8 a.m. on the morning of the experiments, prior to IPGTTs. GLP-1RAs were then co-administered at the indicated concentrations with 20% (w/v) D-glucose via IP injection at weight-adjusted volumes. Baseline glucose readings were taken via tail venipuncture, and subsequent readings taken at various time-points after glucose ± GLP-1RA administration as for the OGTTs. For GLP-1RAs with shorter half-lives (exendin-4 and exendin-F1), IPGTTs were repeated 6 hours after the start of the initial IPGTT, with continued fasting. For the extended half-life GLP-1RA semaglutide, IPGTTs were performed 24 and 72 hours after GLP-1RA administration, with access to food restored at the end of each IPGTT.

Measurement of in vivo plasma insulin levels

To measure insulin release during IPGTTs, 10 µL blood samples were collected via tail venipuncture into potassium EDTA cuvettes (Microvette CB 300, 16.444.100, Starstedt) 10 minutes after glucose challenge, and stored on ice before centrifugation at 8,000 x g for 10 minutes at 4°C to collect plasma supernatants. Plasma was collected in fresh Eppendorf tubes and kept at -80°C until further analysis using the Mouse Plasma Insulin Homogeneous Time Resolved Fluorescence (HTRF) kit (#62IN3PEF; Revvity) following the manufacturer's instructions.

Immunostaining of pancreatic sections

Whole pancreata from *hGlp1r* $^{A316T/A316T}$ mice and *hGlp1r* $^{+/+}$ control littermates were dissected, placed in ice cold phosphate buffer saline (PBS), cleared from surrounding fat and non-pancreatic tissues, weighed, and fixed for 24 hours in 4% paraformaldehyde (PFA) at 4°C and then cryoprotected in 30% sucrose, followed by embedding in optical cutting temperature (OCT) and stored at -80°C. Frozen 10 µm sections were prepared using a cryostat and immunostained with guinea pig anti-insulin polyclonal antibody (1:100; Dako IR002, Agilent Technologies; Alexa Fluor 488 secondary antibody, Thermo Fisher Scientific) for β-cell, and mouse anti-glucagon antibody (1:500; G2654, Sigma-Aldrich; Alexa Fluor 568 secondary antibody, Thermo Fisher Scientific) for α-cell detection. Samples were mounted with Prolong Diamond Antifade Mountant with DAPI (P36962, Thermo Fisher Scientific) for nuclei visualisation. Stained slides were imaged at 4x to quantify total pancreatic area, and at 40x to image pancreatic islet insulin and glucagon positive areas using a wide-field Zeiss Axio Observer inverted microscope from Imperial College Facility for Imaging by Light Microscopy (FILM). Total pancreatic, insulin and glucagon positive areas were measured per slide using the Fiji software. β- and α-cell mass was calculated by normalising to total pancreatic section area and pancreas weight as described before[91, 92]. Islet size and cytoarchitecture analyses were performed on the same images used for β- and α-cell mass assessments. All non-islet regions were erased using the ImageJ outline and clear outside functions. Cells were assigned to be in

the islet periphery/mantle if they were within the 2 outermost cell layers of the islet, or in the islet core if they fell within any layers deeper than these.

In vivo hGLP-1R labelling in the pancreas

The *hGlp1r* $^{A316T/A316T}$ mice and *hGlp1r* $^{+/+}$ control littermates were injected subcutaneously with 100 pmol/g of exendin-9-Cy5 two hours before terminal anaesthesia (1.5% sodium pentobarbital) and transcardial perfusion fixation with PBS at pH 7.2, supplemented with 4% fresh PFA[2]. Pancreata were dissected and frozen sections prepared and mounted as above. Images of sections were captured using a Nikon Eclipse Ti spinning disk confocal microscope and 60x oil immersion objective with an ORCA-Flash 4.0 camera (Hamamatsu) and Metamorph software (Molecular Devices), with λ_{ex} = 660 nm and analysed in Fiji.

Isolation and maintenance of islets

The appropriate animals were humanely euthanised prior to pancreas inflation via injection of RPMI 1640 medium (S1745602, Nordmark Biochemicals) supplemented with 1 mg/mL collagenase from Clostridium histolyticum (S1745602, Nordmark Biochemicals) into the common bile duct. The pancreas was then dissected and incubated in a water bath at 37°C for 10 min. Digestion was quenched with cold mouse islet culture medium: RPMI 1640 supplemented with 10% (v/v) fetal bovine serum (FBS) (F7524, Sigma-Aldrich) and 1% (v/v) penicillin/streptomycin (P/S) (15070-063, Invitrogen). Islets were subsequently washed, purified on a Histopaque gradient (Histopaque-1119 and -1083, Sigma-Aldrich), and allowed to recover overnight at 37°C in 5% CO_2 in mouse islet culture medium prior to any experiments. Human donor islets, obtained from the European Diabetes Study Centre (CEED) facilities in Strasbourg with all ethical approvals in place, were cultured in RPMI 1640 supplemented with L-glutamine, 10% (v/v) FBS, 1% (v/v) P/S, 0.25 µg/mL amphotericin B, and 5.5 mM glucose at 37°C in 5% CO_2. Human donor characteristics are listed in Supplementary Table 2.

Cell line generation and culture

INS-1 832/3 cells stably expressing pSNAP/FLAG-*hGlp1r* ^{WT} or ^{A316T} were derived *in house* from the parental INS-1 832/3 *Glp1r* $^{-/-}$ cell line, where endogenous rat GLP-1R has been eliminated by CRISPR/Cas9[50], a gift from Dr Jacqui Naylor, AstraZeneca, by transfecting the corresponding plasmid followed by selection in 1 mg/mL G418 and fluorescence-activated cell sorting (FACS) of the SNAP-positive cell population, and maintained in RPMI-1640 with 11 mM glucose, 10 mM HEPES, 2 mM glutamine, 1 mM sodium pyruvate, 50 µM β-mercaptoethanol, 10% FBS, 1% P/S and 1 mg/mL G418. Human EndoC-βH3 cells (Human Cell Design) were cultured on 2 µg/mL fibronectin and 1% extracellular matrix (E1270, Sigma-Aldrich) coated plates in Advance DMEM/F-12 (Thermo Fisher Scientific), 6.7 ng/ml sodium selenite, 10 mM nicotinamide, 5.5 µg/mL human transferrin, 2mM L-glutamine, 2% BSA Fraction V (Roche), 1% P/S solution and 50 µM β-mercaptoethanol. All cells were incubated in a humidified air incubator containing 5% CO_2 at 37°C.

Generation and characterisation of EndoC-βH3 hGlp1r $^{-/-}$ *cells*

a) CRISPR/Cas9 dgRNA design

To generate EndoC-βH3 *hGlp1r* $^{-/-}$ cells, a lentiviral CRISPR/Cas9 approach was used as previously described[93, 94]. Cas-Designer (http://www.rgenome.net/cas-designer/) was used to design two 17 nucleotide-long (truncated) guide RNAs (gRNAs), 5'- GCTGCTCGGGATGGTGGGCA-3' and 5'-GTTGCAGAACAAGTCTGTGG-3' (reverse complement), flanking the target DNA sequences. Designed gRNAs were cloned into a pSpCas9(BB)-2A-Blast backbone (plasmid #118055, Addgene), which allows for blasticidin selection of cells after transfection, following a previously described dual gRNA cloning strategy[94] as follows: oligonucleotides corresponding to deletion-yielding pairs of gRNAs were assembled in a reaction mix containing 1x Q5 reaction buffer, 200 µM dNTPs, 0.5 µM primer, 0.02 U/µL Q5 high-fidelity DNA polymerase and 0.25 ng/µL of pScaffold-H1 vector (plasmid #118152, Addgene), with Ta = 58°C, 15 second extension, for 30 amplification cycles. PCR products were digested and ligated to

pSpCas9(BB)-2A-Blast in a one-step digestion ligation reaction with 1x Tango buffer, 1 µL FastDigest BbsI (Thermo Fisher Scientific), 1µL DTT 0.1M, 1µL ATP 10 mM, 0.5 µL T7 ligase, 100 ng vector and 1 µL of PCR product (diluted 1:20). Digestion-ligation reactions underwent 6 cycles of 5 minutes at 37°C and 5 minutes at 23°C, and a final 5minute incubation at 37°C, after which 1 µL of ligation product was transformed into NEB Stable competent *E. coli* (New England Biolabs). Successful double gRNA (dgRNA) insertion was confirmed by Sanger sequencing.

b) Lentiviral production and transduction of EndoC-βH3 cells

To produce CRISPR/Cas9 lentiviral particles, HEK293T cells were co-transfected with dgRNA vector from above as well as packaging (psPAX2) and envelope (pMD2.G) vectors using a calcium phosphate protocol[95]. Viral supernatants were harvested 48 and 72 hours after transfection, cleared using a 0.45-µm Millex-HV filter, and concentrated by adding PEG 8000 (Sigma) and NaCl until final concentrations of 10% and 0.15 M, respectively. The mixture was then incubated for 16 to 20 hours on a shaker at 4°C, followed by centrifugation for 30 minutes at 10,000 g at 4°C. Virus pellets were resuspended in 100 µL PBS and stored at -80°C. 48 hours before transduction, EndoC-βH3 cells were seeded at 1 million cells per well in 6-well plates, and 50 µL of virus used to infect each well. After 72 hours, cells were selected for vector integration using blasticidin (20 µg/mL) for 10 days, with selection medium changed every ~3 days (Extended Data Fig. 1c). After selection, cells were labelled with fluorescent exendin-9-TMR for 10 minutes and reverse FACS sorted to recover the population enriched in non-labelled *hGlp1r* $^{-/-}$ cells.

c) EndoC-βH3 hGlp1r $^{-/-}$ *validation by HTRF cAMP assay*

EndoC-βH3 WT and *hGlp1r* $^{-/-}$ cells were pre-treated for 3 weeks with 1 µM of 4-hydroxytamoxifen to induce beta cell differentiation[49]. On the day of the experiment, cells were incubated in 0.5 mM glucose comtaining EndoC-βH3 medium ± 100 nM exendin-4 and the phosphodiesterase inhibitor isobutyl methylxanthine (IBMX). Cells were then lysed in in Krebs-Ringer bicarbonate-HEPES (KRBH) (140 mM NaCl, 3.6 mM KCl, 1.5 mM $CaCl_2$, 0.5 mM $MgSO_4$, 0.5 mM NaH_2PO_4, 2 mM $NaHCO_3$, 10 mM HEPES,

saturated with 95% O_2/5% CO_2; pH 7.4) buffer + 1% Triton X-100 and lysates used to determine cAMP production using a cAMP Dynamic 2 homogeneous time-resolved fluorescence (HTRF)-based assay kit (Revvity) in a PHERAstar reader (BMG Labtech), following the manufacturer's instructions. Results show decreased cAMP responses in *EndoC-βH3 hGlp1r* $^{-/-}$ *versus* WT cells (Extended Data Fig. 1d), suggesting enrichment in *hGlp1r* $^{-/-}$ cells within the CRISPR/Cas9-transduced cell population.

Insulin secretion assays

Purified mouse islets used for insulin secretion assays were treated in 24-well non-adherent plates. Eight islets were used per replicate with three technical replicates per condition. For acute studies, islets were preincubated for 1 hour in KRBH buffer containing 0.1% (w/v) bovine serum albumin (BSA) (10775835001, Roche) and 3 mM glucose before incubation with 11 mM glucose ± 100 nM GLP-1RAs in KRBH buffer in a shaking 37°C water bath (80 rpm) for 1 hour. For overnight studies, preincubation was carried out in RPMI 1640 medium containing FBS, P/S, and 3 mM glucose, followed by treatment with medium supplemented with 11 mM glucose ± GLP-1RAs for 16 hours. Supernatants containing secreted insulin were collected, centrifuged at 1000 rpm for 1 minute, and transferred to fresh tubes. For total insulin content, islets were lysed using acidic ethanol (75% ethanol, 1.5 mM HCl). Lysates were sonicated 3x 10 seconds each in a water bath and centrifuged at 10,000 g for 10 minutes, and supernatants collected. For human islets, the same experiment was performed with islets previously transduced with pAV-SNAP/FLAG-*hGlp1r* ^{WT} or ^{A316T} adenoviruses (generated by VectorBuilder) at a multiplicity of infection (MOI) of 1, 24 hours prior to the start of experiments. Insulin secretion assays with the human EndoC-βH3 cell line were performed following 3 weeks of treatment with 4-hydroxytamoxifen as above, followed by transduction with pAV-SNAP/FLAG-*hGlp1r* ^{WT} or ^{A316T} adenoviruses, with insulin secretion assessed as previously described[49], with the following modifications: after preincubation with 0.5 mM glucose KRBH buffer, cells were stimulated with 15 mM glucose ± exendin-4 for 60 minutes. Total and secreted insulin samples from islets and cells were stored at −20°C until quantification using an Insulin

Ultra-Sensitive HTRF kit (62IN2PEG, Revvity) in a PHERAstar plate reader (BMG Labtech), according to the manufacturer's instructions.

Real-time cAMP imaging

To measure cAMP, *hGlp1r* $^{A316T/A316T}$ *versus* $^{+/+}$ control mouse islets, or INS-1 832/3 SNAP/FLAG-*hGlp1r* ^{WT} *versus* ^{A316T} cells cultured on glass-bottom MatTek dishes, were transduced with cADDis (Green Gs cADDis cAMP Kit, Montana Molecular), a baculovirus genetically encoding a fluorescent cAMP in situ biosensor, following the manufacturer's instructions. Transduced islets were subsequently encased into Matrigel on glass-bottom MatTek dishes 24 hours after transduction, and both islets and cells were imaged at λ_{ex} = 488 nm in a Nikon Eclipse Ti spinning disk confocal microscope and 20x objective with an ORCA-Flash 4.0 camera (Hamamatsu) for time-lapse recordings with image acquisitions every 6 seconds in KRBH buffer containing 0.1% (w/v) BSA and 6 mM glucose for 2 minutes to record the baseline, with 100 nM GLP-1RA subsequently added by manual pipetting, and islets imaged for a further 5 minutes before addition of 100 μM IBMX + 10 μM forskolin for the final 2 minutes of the acquisition. Raw green fluorescence intensity traces were extracted from whole islet regions of interest (ROIs) using Fiji, and mean intensities calculated for each ROI and time point. Responses were plotted relative to average fluorescence intensity per islet during the baseline period before GLP-1RA addition.

Islet immunofluorescence

For immunostaining, *hGlp1r* $^{A316T/A316T}$ or $^{+/+}$ control mouse islets were fixed in 4% PFA and stored in PBS. After 15 minutes of permeabilisation with 0.5% (v/v) Triton X-100 in PBS, the islets were washed once with PBS and incubated in blocking buffer (PBS + 1% BSA) for 1 hour. Primary antibodies against insulin (1:50; Dako IR002, Agilent Technologies) and glucagon (1:500; G2654, Sigma-Aldrich) were added overnight in blocking buffer, followed by 3x washes in PBS and 1 hour incubation at room temperature with secondary anti-guinea pig Alexa Fluor 488 and anti-mouse Alexa Fluor 647 (both at 1:500; Thermo Fisher Scientific). Islets were then loaded onto glass-bottom MatTek dishes in PBS and three images

acquired at different z positions by confocal microscopy in a Zeiss LSM-780 inverted confocal laser-scanning microscope and a 63×/1.4 numerical aperture oil immersion objective from Imperial College FILM Facility. Images were analysed using Fiji.

Measurement of mini-G_s and β-arrestin 2 recruitment by NanoBiT complementation

For mini-G_s recruitment, INS-1 832/3 *Glp1r* $^{-/-}$ cells were seeded in 6-cm dishes and transiently co-transfected with 1.7 µg each of *hGlp1r* ^{WT} or ^{A316T}-SmBiT and LgBiT-mini-G_s constructs for 24 hours. Cells were then detached, resuspended in Hank's buffered salt solution (HBSS) containing NanoGlo Live Cell Reagent (1:20; Promega) with furimazine, and seeded onto white 96-well half-area plates. Baseline luminescence was immediately recorded over 8 minutes at 37°C in a Flexstation 3 plate reader (Molecular Devices), and for a further 30 minutes after GLP-1RA addition at serial doses up to 100 nM. Readings were taken every 30 seconds and normalised to average well baseline, and average vehicle-induced signal subtracted to establish the agonist-induced effect. To measure β-arrestin 2 recruitment, cells were processed as above with slight modifications: INS-1 832/3 *Glp1r* $^{-/-}$ cells were co-transfected with 1.77 µg each of *hGlp1r* ^{WT} or ^{A316T}-SmBiT and LgBiT-β-arrestin 2 plasmids for 24 hours and GLP-1RAs added at serial doses up to 1 µM. Areas under the curve (AUCs) were calculated for each agonist concentration and fitted to log(agonist) *versus* response four-parameter curves using GraphPad Prism 10.1.2.

High content microscopy GLP-1R trafficking assays

a) Internalisation assay

INS-1 832/3 SNAP/FLAG-*hGlp1r* ^{WT} or ^{A316T} cells were seeded onto poly-D-lysine-coated black 96-well plates for 24 hours before the assay. Cells were labelled for 30 minutes with 1 µM SNAP surface cleavable BG-SS-649 probe at 37°C and washed once with HBSS before treatment with GLP-1RA or vehicle for 60, 30, 15, or 5 minutes at 37°C in complete medium. Cells were then washed with cold HBSS, and subsequent steps carried out at 4°C. The cell impermeable reducing agent Mesna [100 mM in alkaline

TNE buffer (20 mM TrisHCl, 1 mM EDTA, 150 mM NaCl, pH 8.6)] or alkaline TNE buffer without Mesna was applied for 5 minutes to cleave BG-SS-649 probe left at the cell surface, and then washed with HBSS. Plates were imaged immediately without fixation using a modular microscope platform from Cairn Research incorporating a Nikon Ti2E, LED light source (CoolLED), fitted with a 20x phase contrast objective, assisted by custom-written high content analysis software implemented in Micro-Manager. A minimum of 9 images per well were acquired for both epifluorescence and transmitted phase contrast. Internalised GLP-1R, indicated by cell-associated fluorescence, was analysed after flat-field correction of fluorescent images using the BaSiC plugin[96], segmentation of cell-containing regions from phase contrast images using Phantast[97], and fluorescence intensity quantification. The percentage of internalised receptor was calculated as follows:

$$\frac{(F_{+Me}(t_x)/(F_{-Me}(t_x)) - (F_{+Me}(t_0)/(F_{-Me}(t_0))}{1 - (\frac{F_{+Me}(t_0)}{F_{-Me}(t_0)})}$$

Where F_{+Me} and F_{-Me} are mean fluorescence intensities ± MesNa at times t_x (5, 15, 30, or 60 minutes) or t_0 (0 minutes). Percentages of internalisation were plotted to calculate the AUC using GraphPad Prism 10.1.2.

b) Recycling assay

INS-1 832/3 SNAP/FLAG-*hGlp1r* ^{WT} or ^{A316T} cells were seeded as above for 24 hours, washed with HBSS, pre-treated with vehicle or GLP-1RA for 1 hour at 37°C in complete medium, washed again and treated with 100 nM exendin-4-TMR in reverse time order for 3 hours and 1 hour at 37°C in complete medium. Plates were then promptly imaged after washing as above. In this assay, total exendin-4-TMR uptake is indicative of residual surface receptor at the end of the GLP-1RA treatment and cumulative reappearance of the surface receptor during the recycling period.

c) Degradation assay

INS-1 832/3 SNAP/FLAG-*hGlp1r* ^{WT} or ^{A316T} cells were seeded as above. Cells were then washed with HBSS before addition of 50 μg/mL cycloheximide in serum-free medium to halt protein translation. After one hour, a time course was performed with the GLP-1RA added in reverse time order for 8, 4, 2, 1, 0.5, and 0 hours. For the final 30 minutes of the experiment, the cell medium was replaced with 1 μM of total SNAP-labelling fluorescent probe BG-OG in complete medium, to label total residual GLP-1R. Cells were then washed 3x with HBSS prior to plate imaging as above using a green fluorescence filter set. Total GLP-1R was quantified as the average cellular fluorescence labelling per well (as defined above), with further subtraction of non-specific fluorescence (i.e. cells without BG-OG labelling). Results were expressed as a percentage relative to vehicle treated BG-OG labelled cells and AUCs recorded as above.

Lysosomal inhibition assay

INS-1 832/3 SNAP/FLAG-*hGlp1r* ^{WT} or ^{A316T} cells on coverslips, mouse *hGlp1r* $^{-/-}$ islets transduced with pAV-SNAP/FLAG-*hGlp1r* ^{WT} or ^{A316T} adenoviruses, or *hGlp1r* $^{A316T/A316T}$ and $^{+/+}$ control islets were incubated for 2 hours ± 100 nmol/L bafilomycin-A1 (Sigma-Aldrich), an established vacuolar H^+-ATPase and lysosomal trafficking inhibitor[98], in complete medium. Cells and transduced *hGlp1r* $^{-/-}$ islets were then labelled with 1 μM SNAP-Surface 549, and *hGlp1r* $^{A316T/A316T}$ *versus* $^{+/+}$ islets treated with exendin-9-TMR in complete medium at 37 °C for 10 minutes. Cells were washed and fixed in 4% PFA, mounted in Prolong Diamond antifade reagent with DAPI, while islets were loaded onto glass-bottom MatTek dishes in PBS and images acquired by confocal microscopy with a Zeiss LSM-780 inverted confocal laser-scanning microscope and a 63x/1.4 numerical aperture oil immersion objective from the Imperial College FILM Facility. Images were analysed using Fiji.

Surface GLP-1R expression analysis

INS-1 832/3 SNAP/FLAG-*hGlp1r* ^{WT} or ^{A316T} cells, or EndoC-βH3 cells transduced with pAV-SNAP/FLAG-*hGlp1r* ^{WT} or ^{A316T} adenoviruses were labelled with 1 μM SNAP-Surface 549 at 37°C in 5% CO_2, washed

twice in PBS and fixed with 4% PFA at 4°C for 20 minutes, mounted onto slides in Diamond Prolong anti-fade Mountant with DAPI (Thermo Fisher Scientific), and images acquired by confocal microscopy with the Zeiss LSM-780 inverted confocal laser-scanning microscope from above using a 20x objective. Human and *hGlp1r* $^{-/-}$ mouse islets transduced with pAV-SNAP/FLAG-*hGlp1r* ^{WT} or ^{A316T} adenoviruses were labelled with 1 μM SNAP-Surface 649 for 10 minutes, washed with PBS and imaged as above with a 63x/1.4 numerical aperture oil immersion objective. *hGlp1r* $^{A316T/A316T}$ *versus* $^{+/+}$ transgenic mouse islets were labelled with exendin-9-TMR in complete medium at 37°C for 10 minutes and imaged as above. Images were analysed using Fiji.

RNA extraction and qPCR

Total RNA was extracted from islets (50-100) isolated from *hGlp1r* $^{A316T/A316T}$ *versus* $^{+/+}$ mice, using TRIzol reagent (Invitrogen) and briefly vortexed for homogenisation. Chloroform was added to achieve phase separation, and the upper aqueous phase collected. RNA was recovered overnight by precipitation with isopropanol (Thermo Fisher Scientific) and 100-500 ng reverse transcribed using the MultiScribe Reverse Transcriptase (Thermo Fisher Scientific) according to the manufacturer's instructions. Quantitative PCR (qPCR) using SYBR Green Technology was carried out on an Applied Biosystems 7500 real-time PCR system. Data were analysed using the 2−ΔΔCt method[99]. A list of qPCR primer sequences is provided in Supplementary Table 3.

Protein extraction and Western blotting

INS-1 832/3 SNAP/FLAG-*hGlp1r* ^{WT} or ^{A316T} cells were treated with vehicle or exendin-4 for 5 minutes, washed once in cold PBS and lysed 1x TNE lysis buffer (20 mM Tris, 150 mM NaCl, 1 mM EDTA, 1% NP40, protease and phosphatase inhibitors) for 10 minutes at 4°C. Samples were then sonicated in a water bath sonicator 3x 10 seconds and centrifuged at 13,000 rpm for 5 minutes. Supernatants were collected and resolved by SDS-polyacrylamide gel electrophoresis (10% acrylamide gels) in 2x urea loading buffer (200mM Tris HCl, 5% w/v SDS, 8 M urea,100 mM DTT, 0.02% w/v bromophenol blue, pH

6.8). A Bio-Rad wet transfer system was used for immunoblotting onto PVDF membranes (Immobilon-P, 0.45-µm pore size, IPVH00010, Merck) before incubation with appropriate primary and secondary antibodies in 5% skimmed milk. SNAP-tagged GLP-1R was detected with an anti-SNAP tag rabbit polyclonal antibody (1:500; New England Biolabs) followed by goat anti rabbit IgG HRP (1:2,000; Abcam). Post-stripping, tubulin was labelled with anti-α-tubulin mouse monoclonal antibody (1:5,000; T5168, Sigma) followed by sheep anti-mouse secondary antibody HRP (1:5,000; Abcam). Blots were developed using Clarity™ Western ECL Substrate System (BioRad) in a Xograph Compact X5 processor and specific band densities quantified in Fiji.

Cryo-EM determination of GLP-1:GLP-1R (A316T):Gα_s complex structure

a) Construct design

A human GLP-1R construct with residue Ala316 substituted for Thr (c.946G>A) was generated from the WT sequence by Q5 enzyme site-directed mutagenesis (New England Biolabs) and cloned into the pFastBac vector. The native signal peptide was replaced with HA to enhance expression, and an N-terminal FLAG epitope and a C-terminal 6xHis epitope added as affinity tags with 3C protease cleavage sites. These modifications do not significantly alter the function of WT GLP-1R[100].

b) Purification of GLP-1:GLP-1R (A316T):DN-Gα_s:nb35

A-FLAG-GLP-1R (A316T)-His, DN-Gα_S, and Gβ1γ2-His P2 baculoviruses were co-infected in a 500 mL culture of *T. ni* Hi5 insect cells in suspension (density 3-4x10^6 cells/mL), at a ratio of 2:1:1. After 48 hours, the cell preparations were harvested by centrifugation at 8,000 g for 10 minutes and the supernatant discarded. The pelleted cell mass was stored at -80°C until use. For purification, cell preparations were rapidly thawed and resuspended in 50 mL of buffer. Receptor-G protein complex was formed in the presence of 10 µM GLP-1 for 30 minutes at room temperature with gentle stirring. After this period, nanobody 35 (nb35, 1 mg) and apyrase (5 µL/L of starting culture, equivalent to 2.5 U) were added to the

resuspension and incubated at room temperature for a further 30 minutes. Purified nb35 was a kind gift from Minakshi Baruah.

c) Vitrification and data collection of purified samples

2 µL of sample was applied to glow-discharged R1.1/1.2 gold foil grids, manufactured by Quantifoil at the Melbourne Centre for Nanofabrication (MCN) immediately followed by plunge-freezing in liquid ethane using a Vitrobot Mark IV (Thermo Scientific) set at 4°C, 100% humidity. At least 3 grids were prepared for each sample, and blot force and blot time varied between 16-18 and 6-8 seconds, respectively. Vitrification conditions for grids used in data collection were as follows: blot force 16 and blot time 7 seconds. cryo-EM data were collected on a Glacios cryo-TEM (Thermo Scientific) operating at 200 kV accelerating voltage in cryo-TEM nanoprobe mode with a 100 µm objective aperture inserted. Data were collected using aberration-free image shift in fast acquisition mode in the EPU software (Thermo Scientific).

d) Data processing for GLP-1:GLP-1R (A316T):DN-Gα_s:nb35

3,170 micrographs were assigned to 69 optics groups based on their beam-image shift coordinates, motion corrected in RELION 3.1.2 and CTF parameters estimated using CTFFIND 4.1 within RELION[101]. For quality control, micrographs with an estimated maximum resolution >20 Å were excluded, leaving 2,940 micrographs in the dataset. 1,667,111 particles were picked using a pre-trained general model in crYOLO 1.7.6[102] and extracted with 4.5-fold binning. These particles were imported into cryoSPARC 3.2[103] and subjected to rounds of 2D classification to homogenise the particle stack, with 583,410 particles remaining. These particles were re-extracted at the full box size (288 px2) and subjected to Bayesian polishing in RELION 3.1.2. The polished particles were re-imported into cryoSPARC, filtered for polishing artefacts by 2D classification, and a final set of 330,000 was subjected to non-uniform refinement to obtain a 3.3 Å global resolution consensus density map. Atomic model refinement used an existing model of WT GLP-1R bound to GLP-1 and DN-Gα_s proteins (PDB: 6X18) where Ala316 of GLP-1R was mutated to

Thr. The mutated model was fitted into the experimental density map and subjected to MDFF refinement using Isolde[104] within ChimeraX 1.5[105]. Iterative rounds of real-space refinement in PHENIX 1.20[106], followed by MDFF in Isolde, were used to obtain the final model for analysis. Data collection, processing and refinement statistics for the cryo-EM of GLP-1:GLP-1R (A316T):DN-Gα_s:nb35 complex are summarised in Supplementary Table 4.

Computational methods and MD simulations

a) MD simulations of the A316T and WT GLP-1R structures

The cryo-EM GLP-1:GLP-1R (A316T):Gα_s complex structure and the corresponding GLP-1:GLP-1R(WT):Gα_s (PDB 6X18[54]) were subjected to the same preparation for MD simulations. The missing stalk region (residues 130-135) and ICL3 (residues 339-343) of 6X18 were added by superimposition from the GLP-1:GLP-1R:Gα_s structure simulated in [107] and Gα_s was removed. The resulting systems (i.e., WT and A316T) were superimposed with the PDB 6X18 OPM reference[108] in order to opportunely orient the receptor, and parameterized with the CHARMM36 force field[109], employing in-house Python HTMD[110] and Tool Command Language (TCL) scripts. Hydrogen atoms were added at a simulated pH of 7.0 using the pdb2pqr[111] and propka[112] software, and the protonation of titratable side chains was checked by visual inspection to correctly orient the receptor before inserting[113] in a rectangular 100 Å x 101 Å 1-palmitoyl-2-oleyl-sn-glycerol-3-phosphocholine (POPC) bilayer (previously built by using the VMD Membrane Builder plugin 1.1 at http://www.ks.uiuc.edu/Research/vmd/plugins/membrane/), removing the lipid molecules overlapping the receptor TMD bundle. TIP3P water molecules[114] were added to the simulation box (100 Å x 101 Å x 136 Å) employing the VMD Solvate plugin 1.5 at http://www.ks.uiuc.edu/Research/vmd/plugins/solvate/. Overall charge neutrality was finally reached by adding Na^+/Cl^- counter ions (final ionic concentration of 0.150 M), using the VMD Autoionize plugin 1.3 at http://www.ks.uiuc.edu/Research/vmd/plugins/autoionize/. For WT and A316T GLP-1Rs, equilibration and production replicas were computed using ACEMD[115]. For the equilibration, isothermal-isobaric

conditions (Berendsen barostat[116] with a target pressure of 1 atm; Langevin thermostat[117] with a target temperature of 300 K and damping of 1 picosecond^{-1}) were employed to equilibrate the systems through a multi-stage procedure (integration time step of 2 femtoseconds). First, clashes between lipid atoms were reduced through 1,500 conjugate-gradient minimisation steps. A positional constraint of 1 kcal/mol Å^{-2} lipid phosphorus atoms, protein Ca carbon and all the other protein-heavy atoms were applied and gradually released over 4, 100 and 80 nanoseconds respectively, before further 50 nanoseconds without any restraints for a total of 150 nanoseconds. Productive trajectories (2.5 Å microseconds for each replica, 7.5 microseconds for each system) were computed with an integration time step of 4 femtoseconds in the canonical ensemble (NVT) at 300 K, using a thermostat damping of 0.1 ps^{-1} and the M-SHAKE algorithm[118] to constrain the bond lengths involving hydrogen atoms. The cut-off distance for electrostatic interactions was set at 9 Å, with a switching function applied beyond 7.5 Å. Long-range Coulomb interactions were handled using the particle mesh Ewald summation method (PME)[119] by setting the mesh spacing to 1.0 Å.

b) GLP-1R WT and A316T TMD simulations

Using the GLP-1:GLP-1R:Gα_s cryo-EM complex (PDB 6X18[54]) as the starting structure, we removed Gα_s, GLP-1, ECD, and extracellular loop 1 (ECL1) to minimise the possible interference with the GLP-1R TMD dynamics (Extended Data Fig. 10a). Position 316 of the resulting TMD WT was mutated from Ala to Thr to model the A316T TMD and after membrane insertion and solvation, the two systems (i.e. TMD WT and TMD A316T) underwent 12 milliseconds of MD each; ICL3 residues 339I - 343 were modelled using Modeller 9.18[120] through Chimera[105] (v1.14) user interface, considering the best DOPE score. A316T was modelled using Chimera. The resulting GLP-1R TMD systems (i.e., WT and A316T) were prepared for MD simulations as reported above, after superimposition with the PDB 6X18 OPM reference[108], with the CHARMM36 force field[109] by inserting[113] them in a rectangular 96 Å x 96 Å POPC bilayer. For both WT and A316T, three independent equilibrations and production replicas were computed using ACEMD[115]

and the settings reported above Productive trajectories (4 microseconds for each replica, 12 microseconds for each system) were computed with an integration time step of 4 femtoseconds in the canonical ensemble (NVT) at 300 K.

c) MD simulations of exendin-F1 (Ex-F1) in complex with A316T and WT GLP-1R

The Ex-F1:GLP-1R (A316T):Gα_s was modelled from the Ex-F1:GLP-1R(WT):Gα_s complex structure by mutating in silico A316$^{5.46}$ to T316$^{5.46}$. Ex-F1:GLP-1R(WT):Gα_s and Ex-F1:GLP-1R (A316T):Gα_s were prepared for MD simulations by superimposing the structures on GLP-1R coordinates retrieved from the OPM database in order to opportunely orient the receptor before being inserted in a rectangular 125 Å x 116 Å POPC bilayer, removing the lipid molecules overlapping the receptor TMs bundle. TIP3P water molecules[114] were added to the simulation box (125 Å x 116 Å x 190 Å) and overall charge neutrality was finally reached by adding Na^+/Cl^- counter ions (final ionic concentration of 0.150 M). Equilibration and MD productive simulations computed using ACEMD in isothermal-isobaric conditions (target pressure 1 atm; target temperature 310 K) were employed to equilibrate the systems through 125 nanoseconds of simulation (integration time step of 2 femtoseconds). First, clashes between lipid atoms were reduced through 2,500 conjugate-gradient minimization steps, and then a positional constraint of 1 kcal mol^{-1} Å^{-2} on protein and lipid phosphorus atoms was applied. Lipids restraints were gradually released over a time window of 6 nanoseconds, protein atoms other than alpha carbon atoms were gradually released from the restraints over 100 nanoseconds, while alpha carbon atoms were gradually released over 120 nanoseconds. No restraint was applied in the last 5 nanoseconds of equilibration. Productive trajectories (four 500 nanoseconds-long replicas for each GLP-1R complex) were computed with an integration time step of 4 femtoseconds in the canonical ensemble (NVT) at 310 K as reported above.

d) MD analysis

Atom distances were computed at the Cα level using MDTraj[121]. HBs were quantified using the GetContacts analysis tool (https://getcontacts.github.io/) as the percentage of frames over all the frames

obtained by merging the different replicas in which they were present. Water molecule occupancy was computed employing the VMD[122] Volmap plugin (https://www.ks.uiuc.edu/Research/vmd/plugins/volmapgui/) with 1 Å resolution.

e) Numbering system

Throughout the manuscript, the Wootten residues numbering system for class B GPCRs[73] was adopted.

Statistical analyses

All data analyses and graph generation were performed with GraphPad Prism 10.1.2. The *n* numbers refer to the number of independent biological replicates, representing the number of mice per genotype for *in vivo* experiments, or the number of biologically independent experiments performed from islets isolated from separate mice or from a separate batch of cells, for *ex vivo* or *in vitro* experiments, respectively. Technical replicates within the same assay were averaged to determine the mean value for each biological replicate, prior to statistical tests as indicated in the corresponding figure legends. Statistical significance was assessed with the indicated test, with matched analyses performed for matched design experiments. Statistical significance was inferred when $p<0.05$. Unless indicated, values represented are mean ± SEM.

Data availability

Cryo-EM maps and atomic models for GLP-1:GLP-1R (A316T):Gα_s are deposited in the PDB and EMDB databases with the following code: 3DVA. Proteomics data is deposited in the ProteomeXchange (PRIDE) repository.

Acknowledgements

The authors thank Steve Rothery from the Imperial College Facility for Imaging by Light Microscopy (FILM) for technical support on microscopy experiments and microscopy data analysis; Prof D. Hodson, University of Oxford, for providing LUXendin645; and Elodie Ndjetehe and Zoe Webster from the

Transgenics and Embryonic Stem Cell Facility, MRC Laboratory of Medical Sciences, for their help with CRISPR/Cas9 embryo electroporation and generation of knock-in mice. We additionally thank Drs Bryn Owen and Aida Martinez-Sanchez for providing animal project licenses.

Funding

This work was supported by Diabetes UK PhD Studentship grant 19/0006094 to A.T. and a Society for Endocrinology Research Grant to A.T. and L.E.E. The A.T. group is additionally funded by an MRC Project Grant (MR/X021467/1, with B.J. as co-I), and a Wellcome Trust Discovery Award (301619/Z/23/Z, with B.J. and J.B.S. as co-Is). J.B.S. also acknowledges funding from BBSRC (BB/V019791/1) and MRC (MR/W024985/1). B.J. is further supported by MRC Clinician Scientist Fellowship MR/Y00132X/1 and a Project Grant from Diabetes UK. The Section of Endocrinology at Imperial College London is funded by grants from the MRC, NIHR and is supported by the NIHR Biomedical Research Centre Funding Scheme and the NIHR/Imperial Clinical Research Facility. The views expressed are those of the author(s) and not necessarily those of the NHS, the NIHR or the Department of Health. G.A.R. was supported by a Wellcome Trust Investigator Award (WT212625/Z/18/Z), MRC Programme Grant (MR/R022259/1), NIH-NIDDK Project Grant (R01DK135268), CIHR-JDRF Team Grant (CIHR-IRSC TDP-186358 and JDRF 4-SRA-2023-1182-S-N), CRCHUM start-up funds, and an Innovation Canada John R. Evans Leader Award (CFI 42649). D.J.W. acknowledges support from the MRC (MC-A654-5QB40).

Figure Legends

Fig. 1. *In vivo* glucose responses of adult *hGlp1r* $^{A316T/A316T}$ *versus hGlp1r* $^{+/+}$ mice on a chow diet. **a**, Age-matched body weight of *hGlp1r* $^{+/+}$ *versus* $^{A316T/A316T}$ mixed sex adult littermate mice (*n* = 9 per genotype) maintained on a normal chow diet. **b**, OGTT responses and corresponding AUCs following 2 g/kg body weight glucose administration via oral gavage after 5 hours of fasting in a mixed sex cohort of lean, adult *hGlp1r* $^{+/+}$ *versus* $^{A316T/A316T}$ mice on a chow diet (*n* = 6 per genotype). **c**, Glucose levels after 2

hours of fasting from mice in (**a**). **d**,**e**, IPGTTs (2 g/kg body weight glucose) following acute (0 hours), or 6 hours post-intraperitoneal administration of saline vehicle (Veh) in chow-fed *hGlp1r* $^{+/+}$ *versus* $^{A316T/A316T}$ mixed sex adult mice. Glucose curves (**d**) and corresponding AUCs (**e**) shown; *n* = 9 mice per genotype. **f**-**i**, As in (**d**,**e**) following administration of 2 nmol/kg exendin-4 (Ex-4) (**f**,**g**) or exendin-F1 (Ex-F1) (**h**,**i**). **j**,**k** Vehicle-corrected ΔAUC responses from (**g**) and (**i**), respectively. **l**,**m**, Plasma insulin levels acutely (**l**) and 6 hours (**m**) post-administration of Veh or Ex-4 in chow-fed *hGlp1r* $^{+/+}$ *versus* $^{A316T/A316T}$ mixed sex adult mice. **n**, Plasma insulin vehicle fold changes from (**l**,**m**). Data are mean ± SEM; *p<0.05; **p<0.01; ***p< 0.001; ****p<0.0001; ns, not significant by paired t-tests, one- or two-way ANOVA with Sidak's post-hoc tests.

Fig. 2. *In vivo* glucose responses of adult *hGlp1r* $^{A316T/A316T}$ *versus hGlp1r* $^{+/+}$ mice on a HFHS diet. **a**, Body weight gain for *hGlp1r* $^{+/+}$ *versus* $^{A316T/A316T}$ mixed sex adult littermate mice (*n* = 9 per genotype) maintained on a HFHS diet for the indicated times. **b**, AUCs from (**a**). **c**, OGTT responses and corresponding AUCs following 2 g/kg body weight glucose administration via oral gavage after 5 hours of fasting in a mixed sex cohort of adult *hGlp1r* $^{+/+}$ *versus* $^{A316T/A316T}$ mice on a HFHS diet (*n* = 8 per genotype). **d**, Glucose levels after 2 hours of fasting from mice in (**a**). **e**,**f**, IPGTTs (2 g/kg body weight glucose) following acute (0 hours), or 6 hours post-intraperitoneal administration of saline vehicle (Veh) in HFHS-fed *hGlp1r* $^{+/+}$ *versus* $^{A316T/A316T}$ mixed sex adult mice. Glucose curves (**e**) and corresponding AUCs (**f**) shown; *n* = 9 mice per genotype. **g**-**j**, As in (**e**,**f**) following administration of 2 nmol/kg exendin-4 (Ex-4) (**g**,**h**) or exendin-F1 (Ex-F1) (**i**,**j**). **k**,**l**, Vehicle-corrected ΔAUC responses from (**h**) and (**j**), respectively. **m**-**p**, Glucose curves and corresponding AUCs following vehicle (Veh) (**m**,**n**), or 20 nmol/kg semaglutide (Sema) (**o**,**p**) treatment of HFHS-fed *hGlp1r* $^{+/+}$ *versus* $^{A316T/A316T}$ mice; IPGTTs performed 24 and 72 hours post-agonist administration. **q**, Vehicle-corrected ΔAUC responses from (**p**). Data are mean ± SEM; *p<0.05; **p<0.01; ***p< 0.001; ****p<0.0001; ns, not significant by paired t-tests, one- or two-way ANOVA with Sidak's post-hoc tests.

Fig. 3. Morphological analyses of *hGlp1r* $^{A316T/A316T}$ *versus hGlp1r* $^{+/+}$ mouse islets. a,**b**, Immunofluorescence analysis of insulin (green), and glucagon (red) localisation in isolated islets from chow-fed *hGlp1r* $^{+/+}$ *versus* $^{A316T/A316T}$ mice; size bars, 20 µm. Representative images (**a**) and α- *versus* β-cell number and percentage quantifications (**b**); *n* = 4. **c**,**d**, As in (**a**,**b**) for islets from HFHS-fed *hGlp1r* $^{+/+}$ *versus* $^{A316T/A316T}$ mice; *n* = 4. **e**-**h**, Immunofluorescence analysis of insulin (green), and glucagon (red) localisation in pancreas sections from chow-fed *hGlp1r* $^{+/+}$ *versus* $^{A316T/A316T}$ mice; nuclei (DAPI), blue; size bars, 20 µm. Representative images (**e**), quantification of α- and β-cell number (**f**), α- over β-cell ratio (**g**) and islet diameter (**h**); *n* = 3-4. **i**-**l**, as for (**e**-**h**) in pancreas sections from HFHS-fed *hGlp1r* $^{+/+}$ *versus* $^{A316T/A316T}$ mice. Representative images (**i**), quantification of α- and β-cell number (**j**), α- over β-cell ratio (**k**) and islet diameter (**l**); *n* = 3-5; size bars, 20 µm; arrows indicate cells positive for both insulin and glucagon. **m**, Percentage of islet peripheral/mantle *versus* core α-cells in pancreas sections from HFHS-fed *hGlp1r* $^{+/+}$ *versus* $^{A316T/A316T}$ mice; *n* = 3. Data are mean ± SEM; *p<0.05; **p<0.01; ns, not significant by paired t-tests or two-way ANOVA with Sidak's post-hoc tests.

Fig. 4. GLP-1R surface expression and downstream signalling in *hGlp1r* $^{A316T/A316T}$ *versus hGlp1r* $^{+/+}$ mouse islets. a,**b**, GLP-1R surface expression, assessed *ex vivo* with exendin-9-TMR (Ex-9-TMR) in purified chow and HFHS islets, or *in vivo* following subcutaneous injection of exendin-9-Cy5 (Ex-9-Cy5, LUXendin645) and fluorescence imaging of pancreatic tissue sections of *hGlp1r* $^{+/+}$ *versus* $^{A316T/A316T}$ mice. Representative images (**a**) and quantifications of surface GLP-1R levels (**b**); size bars, 20 µm; *n* = 4-6. **c**,**d**, Live cell cAMP responses to 100 nM exendin-4 (Ex-4) (**c**) or exendin-F1 (Ex-F1) (**d**), measured with the Green Up cADDis cAMP biosensor in chow-fed *hGlp1r* $^{+/+}$ *versus* $^{A316T/A316T}$ mouse islets; responses normalised to baseline; IBMX and forskolin (FSK) added at the acquisition end for maximal responses; *n* = 4. **e**, AUCs calculated from agonist-stimulated periods in (**c**,**d**); *n* = 4 per genotype. **f**, Percentage of acute and overnight (O/N) surface expression (SE)-corrected insulin secretion in chow-fed *hGlp1r* $^{+/+}$ *versus* $^{A316T/A316T}$ mouse islets stimulated with 11 mM glucose (G11) alone or supplemented with 100 nM

exendin-4 (Ex-4) or exendin-F1 (Ex-F1); *n* = 4. **g**, Insulin secretion fold changes to G11 calculated from data in (**f**). **h**, Overnight over acute insulin secretion responses calculated from data in (**g**). **i**, Percentage of SE-corrected insulin secretion in chow-fed *hGlp1r* $^{+/+}$ *versus* $^{A316T/A316T}$ mouse islets stimulated for 24 hours with 11 mM glucose (G11) alone or supplemented with 100 nM semaglutide; *n* = 4. **j**, Insulin secretion fold changes to G11 calculated from data in (**i**). Data are mean ± SEM; *p<0.05; **p<0.01; ***p< 0.001; ****p<0.0001; ns, not significant by paired t-tests, one- or two-way ANOVA with Sidak's post-hoc tests.

Fig. 5. SNAP/FLAG-*hGlp1r* ^{WT} *versus* ^{A316T} surface expression levels and insulin secretion in human β-cell models. a,**b**, Surface expression in EndoC-βH3 *hGlp1r* $^{-/-}$ cells transduced with pAV-SNAP/FLAG-*hGlp1r* ^{WT} or ^{A316T} labelled with SNAP-Surface Alexa Fluor 647. Representative images (**a**) and quantification of surface GLP-1R (**b**); size bars, 10 μm; *n* = 4. **c**, Percentage of surface expression (SE)-corrected insulin secretion in EndoC-βH3 *hGlp1r* $^{-/-}$ cells transduced with pAV-SNAP/FLAG-*hGlp1r* ^{WT} or ^{A316T} in response to 15 mM glucose (G15) alone or supplemented with 100 nM exendin-4 (Ex-4); *n* = 4. **d**, Insulin secretion fold changes to G15 calculated from data in (**c**). **e**,**f**, Surface expression in primary human islets transduced with pAV-SNAP/FLAG-*hGlp1r* ^{WT} or ^{A316T} labelled with SNAP-Surface Alexa Fluor 647. Representative images (**e**) and quantification of surface GLP-1R (**f**); size bars, 20 μm; *n* = 4. **g**, Percentage of SE-corrected insulin secretion in primary human islets transduced with pAV-SNAP/FLAG-*hGlp1r* ^{WT} or ^{A316T} in response to 11 mM glucose (G11) alone or supplemented with 100 nM exendin-4 (Ex-4); *n* = 4. **h**, Insulin secretion fold changes to G11 calculated from data in (**g**). Data are mean ± SEM; *p<0.05; **p<0.01; ***p< 0.001; ****p<0.0001; ns, not significant by paired t-tests or one-way ANOVA with Sidak's post-hoc tests.

Fig. 6. Changes in basal turnover and functional characterisation of INS-1 832/3 *hGlp1r* $^{-/-}$ SNAP/FLAG-*hGlp1r* ^{WT} *versus* ^{A316T} sublines. a, Surface GLP-1R expression in rat insulinoma INS-1 832/3 *hGlp1r* $^{-/-}$ SNAP/FLAG-*hGlp1r* ^{WT} *versus* ^{A316T} cells labelled with SNAP-Surface Alexa Fluor 647.

Representative images and quantification shown; size bars, 10 μm; *n* = 6. **b**, Total GLP-1R expression in INS-1 832/3 *hGlp1r* $^{-/-}$ SNAP/FLAG-*hGlp1r* ^{WT} *versus* ^{A316T} cells, analysed by anti-SNAP tag Western blotting, with tubulin used as loading control; *n* = 4. **c**, Total GLP-1R expression in INS-1 832/3 *hGlp1r* $^{-/-}$ SNAP/FLAG-*hGlp1r* ^{WT} *versus* ^{A316T} cells labelled with membrane-permeable SNAP-tag probe BG-OG. Representative images and quantification shown; size bars, 10 μm; *n* = 5. **d**, Representative images and quantification of surface GLP-1R expression in INS-1 832/3 *hGlp1r* $^{-/-}$ SNAP/FLAG-*hGlp1r* ^{WT} *versus* ^{A316T} cells treated for 2 hours with vehicle (Veh) or 400 μM bafilomycin A1 (Baf) prior to labelling with SNAP-Surface Alexa Fluor 647; size bars, 10 μm; *n* = 5. **e**, As in (**d**) for *hGlp1r* $^{-/-}$ mouse islets transduced with pAV-SNAP/FLAG-*hGlp1r* ^{WT} or ^{A316T}; size bars, 10 μm; *n* = 3. **f**, As in (**d**) for *hGlp1r* $^{+/+}$ *versus* $^{A316T/A316T}$ mouse islets labelled with exendin-9-Cy5 (LUXendin645); size bars, 10 μm; *n* = 4. **g**, GLP-1R internalisation ΔAUC (SNAP/FLAG-*hGlp1r* ^{A316T} minus ^{WT}, calculated from data in Extended Data Fig. 7a,b) in INS-1 832/3 *hGlp1r* $^{-/-}$ SNAP/FLAG-*hGlp1r* ^{WT} *versus* ^{A316T} cells stimulated with the indicated agonists; *n* = 3. **h**, GLP-1R plasma membrane recycling ΔAUC (SNAP/FLAG-*hGlp1r* ^{A316T} minus ^{WT}, calculated from data in Extended Data Fig. 7c,d) in INS-1 832/3 *hGlp1r* $^{-/-}$ SNAP/FLAG-*hGlp1r* ^{WT} *versus* ^{A316T} cells stimulated with the indicated agonists; *n* = 3-4. **i**, GLP-1R degradation ΔAUC (SNAP/FLAG-*hGlp1r* ^{A316T} minus ^{WT}, calculated from data in Extended Data Fig. 7e,f) in INS-1 832/3 *hGlp1r* $^{-/-}$ SNAP/FLAG-*hGlp1r* ^{WT} *versus* ^{A316T} cells stimulated with the indicated agonists; *n* = 3-5. **j**, Baseline LgBiT-mini-G_s recruitment to *hGlp1r* ^{WT} or ^{A316T}-SmBiT in INS-1 832/3 *hGlp1r* $^{-/-}$ cells; responses over time and AUCs shown; *n* = 14. **k**, Baseline LgBiT-β-arrestin 2 (βarr2) recruitment to *hGlp1r* ^{WT} or ^{A316T}-SmBiT in INS-1 832/3 *hGlp1r* $^{-/-}$ cells; responses over time and AUCs shown; *n* = 19. **l**, LgBiT-mini-G_s recruitment to *hGlp1r* ^{WT} or ^{A316T}-SmBiT in INS-1 832/3 *hGlp1r* $^{-/-}$ cells in response to the indicated agonists; log(E_{max}/EC_{50}) calculated from data in Extended Data Fig. 7g,h; SNAP/FLAG-*hGlp1r* ^{A316T} minus ^{WT} Δlog(E_{max}/EC_{50}) also shown; *n* = 5. **m**, LgBiT-β-arrestin 2 (βarr2) recruitment to *hGlp1r* ^{WT} or ^{A316T}-SmBiT in INS-1 832/3 *hGlp1r* $^{-/-}$ cells in response to the indicated agonists; log(E_{max}/EC_{50}) calculated from data

in Extended Data Fig. 7i,j; SNAP/FLAG-*hGlp1r* ^{A316T} minus ^{WT} $\Delta\log(E_{max}/EC_{50})$ also shown; $n = 5$. **n**, LgBiT-β-arrestin 2 minus LgBiT-mini-G_s (βarr2 - mini-G_s) recruitment to *hGlp1r* ^{A316T} minus ^{WT}-SmBiT, shown as $\Delta\log(E_{max}/EC_{50})$, in INS-1 832/3 *hGlp1r* $^{-/-}$ cells as a measure of signal bias. Data are mean ± SEM except for *hGlp1r* ^{A316T} minus ^{WT} responses [ΔAUC or $\Delta\log(E_{max}/EC_{50})$] which are mean ± 95% confidence interval (CI); *p<0.05; **p<0.01; ns, not significant by paired t-tests, one-way ANOVA with Sidak's or two-way ANOVA with Tukey's post-hoc tests.

Fig. 7. Cryo-EM structure of GLP-1:GLP-1R A316T:DN-Gα$_s$:nb35. a, Representative micrograph from 200 kV cryo-EM imaging of the complex (top), with representative 2D class averages of particles used in the consensus refinements (bottom). **b**, Non-uniform refined density map used as the primary source for modelling (top), with atomic model built into the density map, including backbone trace of ECD (bottom). **c**, Transmembrane domains, rendered as cartoons, of GLP-1R A316T (orange) and WT (lavender) overlaid (left), and 140° rotation (right); black arrows indicate the position of residue 316. **d**, Binding arrangement of residues 7-31 of GLP-1 (green) with GLP-1R A316T (orange), facing inwards from TM5 (left), and facing inwards from TM6 (right); dashed lines indicate HBs predicted by ChimeraX 1.5. **e**, Positioning of T316 and Y241$^{3.44}$ below the binding site for GLP-1 (green) (top left); comparison between local arrangement of residues T/A316$^{5.40}$ and Y241$^{3.44}$ in the A316T variant (orange) and WT GLP-1R (azure blue; PDB 6X18) (bottom left); a structural water (red) from the 2.1 Å WT structure has HB interactions (dashed lines) with the backbone of these residues in the WT. Black arrow indicates movement of T316 carbonyl away from A316$^{5.40}$ position. The 2 Å zoned density map (3.4 Å resolution) of the GLP-1R A316T structure is represented as a transparent grey surface; intracellular-facing view of the receptor core, showing the positioning of the TM3-TM5-TM6 structural water network (red) from PDB 6X18 (right). A red cross indicates a potential HB lost for T316. TM7, 1, and 2 have been removed from each panel for clarity. **f**, Key interactions between the GLP-1R A316T intracellular cavity (orange) and the α5 helix of DN-Gα$_s$ (pink) with 'forward' view indicated by left cartoon. HBs, determined by ChimeraX 1.5,

are dashed lines. **g**, Alternate view of GLP-1R A316T – α5 helix interactions as indicated by left cartoon. **h**, left, Cryo-EM density map used to model interactions depicted as coloured transparent silhouettes. There is no density for N338 ICL3, while other nearby side chains are well-resolved; **h**, right, Comparison between GLP-1R A316T – α5 helix (orange and pink) and GLP-1R WT – α5 helix (blue and white) interactions. **i**, left, Close-up of the first and last frames from principal component 3 after 3DVA of GLP-1R A316T, with distant density clipped for clarity; **i**, right, Principal component 3 from 3DVA for GLP-1R WT; raw data from[123]; ECL3 is indicated by bold arrows.

Fig. 8. Divergent HB and solvation patterns in WT *versus* A316T GLP-1R. a, T316$^{5.46}$ rotameric State 1 forms a stable HB with Y242$^{3.45}$. **b**, T316$^{5.46}$ rotameric State 2 is involved in water-mediated interactions with the polar core of the receptor. N320$^{5.50}$ forms stable water bridges with TM6 kink (L360$^{6.49}$ and G261$^{6.50}$) in A316T. **c**-**e**, volumetric map (isovalue 0.3) of water molecules within the TMD of WT GLP-1R (cyan ribbon) in complex only with the endogenous agonist GLP-1 (orange ribbon) from three independent MD simulation replicas. **f**-**h**, volumetric map (isovalue 0.3) of water molecules within the TMD of A316T (cyan ribbon) in complex only with the endogenous agonist GLP-1 (orange ribbon) from three independent MD simulation replicas. The red arrows indicate the position of stable water molecules interacting with N320$^{5.50}$ and the TM6 kink.

Extended Data Figure Legends

Extended Data Fig. 1. Model generation. a, Targeting strategy for *hGlp1r* $^{A316T/A316T}$ knock-in mouse generation; CRISPR single guide RNA (sgRNA) targeting the Cas9 nuclease to the indicated PAM region of exon 9 in the human *Glp1r* gene and corresponding ssODN homology directed repair template sequences are indicated. **b**, Schematic diagram of the method to generate *hGlp1r* $^{A316T/A316T}$ knock-in mice: electroporation of Cas9, sgRNA and ssODN templates into *hGlp1r* $^{+/+}$ pronucleus, followed by IVF transfer of two cell embryo into *hGlp1r* $^{+/+}$ female mice resulting in F0 generation and screening via genomic PCR and Sanger sequencing, with sequences from *hGlp1r* $^{+/+}$ and $^{A316T/A316T}$ mice included. **c**,

Schematic diagram of the method to generate EndoC-βH3 *hGlp1r* $^{-/-}$ cells: transduction with engineered lentiviral CRISPR/Cas9 double guide RNA (dgRNA) vector targeting *hGlp1r* followed by blasticidin selection. **d**, Static cAMP levels from *EndoC-βH3 hGlp1r* $^{+/+}$ *versus* $^{-/-}$ cells under vehicle (Veh) and 30 minutes exendin-4 (Ex-4) stimulation.

Extended Data Fig. 2. *In vivo* glucose responses of adult *hGlp1r* $^{A316T/A316T}$ and *hGlp1r* $^{A316T/+}$ *versus hGlp1r* $^{+/+}$ mice on a chow diet – extra data. a, AUCs from acute IPGTTs taken from Fig. 1e,g,i. **b**, As in (**a**) for IPGTTs 6 hours post-vehicle or agonist administration. **c**, Vehicle fold AUC responses calculated from Fig. 1e,g,i. **d**, Exendin-4 (Ex-4) ΔΔAUC responses (6 hours minus acute) calculated from Fig. 1j. **e**, Exendin-F1 (Ex-F1) ΔΔAUC responses (6 hours minus acute) calculated from Fig. 1k. **f**, Age-matched body weight of *hGlp1r* $^{+/+}$ *versus* $^{A316T/+}$ mixed sex littermate adult mice (*n* = 9 per genotype) on a chow diet. **g**, OGTT responses and corresponding AUCs following 2 g/kg body weight glucose administration via oral gavage after 5 hours of fasting in a mixed sex cohort of lean, adult *hGlp1r* $^{+/+}$ *versus* $^{A316T/+}$ mice on a chow diet (*n* = 5 per genotype). **h**, Glucose levels after 2 hours of fasting in chow fed *hGlp1r* $^{+/+}$ *versus* $^{A316T/+}$ mixed sex adult mice (*n* = 7 per genotype). **i**,**j**, IPGTTs (2 g/kg body weight glucose) following acute (0 hours), or 6 hours post-intraperitoneal administration of saline vehicle (Veh) in chow-fed *hGlp1r* $^{+/+}$ *versus* $^{A316T/+}$ mixed sex adult mice. Glucose curves (**i**) and corresponding AUCs (**j**) shown; *n* = 7 per genotype. **k**-**n**, As in (**i**,**j**) following administration of 2 nmol/kg exendin-4 (Ex-4) (**k**,**l**), or exendin-F1 (Ex-F1) (**m**,**n**). **o**,**p**, Vehicle-corrected ΔAUC responses from (**l**) and (**n**), respectively. Data are mean ± SEM; *p<0.05; **p<0.01; ***p< 0.001; ****p<0.0001; ns, not significant by paired t-tests, one- or two-way ANOVA with Sidak's post-hoc tests.

Extended Data Fig. 3. *In vivo* glucose responses of adult *hGlp1r* $^{A316T/A316T}$ *versus hGlp1r* $^{+/+}$ mice on a HFHS diet – extra data. a, AUCs from acute IPGTTs taken from Fig. 2f,h,j. **b**, As in (**a**) for IPGTTs at 6 hours post-vehicle or agonist administration. **c**, Vehicle fold AUC responses calculated from Fig. 2f,h,j. **d**, Exendin-4 (Ex-4) ΔΔAUC responses (6 hours minus acute) calculated from Fig. 2k. **e**, Exendin-

F1 (Ex-F1) ΔΔAUC responses (6 hours minus acute) calculated from Fig. 2l. **f**, Acute plasma insulin levels post-vehicle (Veh) administration in HFHS-fed *hGlp1r* $^{+/+}$ *versus* $^{A316T/A316T}$ mixed sex adult mice. **g**, AUCs from IPGTTs at 24 hours post-vehicle (Veh) or agonist administration taken from Fig. 2n,p. **h**, As in (g) for IPGTTs at 72 hours post-vehicle (Veh) or agonist administration. **i**, Vehicle (Veh) fold AUC responses calculated from Fig. 2n,p. **j**, Semaglutide (Sema) ΔΔAUC responses (72 hours minus 24 hours) calculated from Fig. 2q. Data are mean ± SEM; *p<0.05; **p<0.01; ***p< 0.001; ****p<0.0001; ns, not significant by paired or ratio paired t-tests, one- or two-way ANOVA with Sidak's post-hoc tests.

Extended Data Fig. 4. *In vivo* glucose responses of adult *hGlp1r* $^{A316T/+}$ *versus hGlp1r* $^{+/+}$ mice on a HFHS diet. a, Body weight gain for *hGlp1r* $^{+/+}$ *versus* $^{A316T/+}$ mixed sex littermate adult mice (*n* = 7 per genotype) maintained on a HFHS diet for the indicated times. **b**, AUC from (**a**). **c**, OGTT responses and corresponding AUC following 2 g/kg body weight glucose administration via oral gavage after 5 hours of fasting in a mixed sex cohort of adult *hGlp1r* $^{+/+}$ *versus* $^{A316T/+}$ mice on a HFHS diet (*n* = 7 per genotype). **d**, Glucose levels after 2 hours of fasting from mice in (**a**). **e**,**f**, IPGTTs (2 g/kg body weight glucose) following acute (0 hours), or 6 hours post-intraperitoneal administration of saline vehicle (Veh) in HFHS-fed *hGlp1r* $^{+/+}$ *versus* $^{A316T/+}$ mixed sex adult mice. Glucose curves (**e**) and corresponding AUCs (**f**) shown; *n* = 7 mice per genotype. **g**-**j**, As in (**e**,**f**) following administration of 2 nmol/kg exendin-4 (Ex-4) (**g**,**h**) or exendin-F1 (Ex-F1) (**i**,**j**). **k**,**l**, Vehicle-corrected ΔAUC responses from (**h**) and (**j**), respectively. **m**-**r**, Glucose curves and corresponding AUCs following vehicle (Veh) (**m**,**n**) or 20 nmol/kg semaglutide (Sema) (**o**,**p**) treatment of HFHS-fed *hGlp1r* $^{+/+}$ *versus* $^{A316T/+}$ mice; IPGTTs performed 24 and 72 hours post-agonist administration; *n* = 7 mice per genotype. **q**, Vehicle-corrected ΔAUC responses from (**p**). Data are mean ± SEM; *p<0.05; **p<0.01; ****p<0.0001; ns, not significant by paired t-tests, one- or two-way ANOVA with Sidak's post-hoc tests.

Extended Data Fig. 5. GLP-1R-induced downstream signalling in *hGlp1r* $^{A316T/A316T}$ *versus hGlp1r* $^{+/+}$ mouse islets – extra data. a,**b**, Relative gene expression of β-cell enriched and disallowed genes

in islets purified from *hGlp1r* $^{A316T/A316T}$ *versus hGlp1r* $^{+/+}$ mice fed a chow (**a**) or HFHS (**b**) diet; size bars, 20 μm; *n* = 4. **c**, Representative confocal microscopy images of islets from *hGlp1r versus mGlp1r* mice treated for 10 minutes with 100 nM exendin-9-TMR. **d**, Quantification of exendin-9-TMR (Ex-9-TMR) fluorescence intensity in islets from (**c**); *n* = 4. **e**, Percentage of acute and overnight (O/N) surface expression (SE)-corrected insulin secretion in HFHS-fed *hGlp1r* $^{+/+}$ *versus* $^{A316T/A316T}$ mouse islets stimulated with 11 mM glucose (G11) alone or supplemented with 100 nM exendin-4 (Ex-4) or exendin-F1 (Ex-F1); *n* = 4. **f**, Insulin secretion fold changes to G11 calculated from data in (**e**). **g**, Overnight over acute insulin secretion responses calculated from data in (**f**). Data are mean ± SEM; *p<0.05; **p<0.01; ***p<0.001; ns, not significant by paired t-tests, or two-way ANOVA with Sidak's post-hoc tests.

Extended Data Fig. 6. GLP-1R surface expression and calcium signalling in *hGlp1r* $^{-/-}$ mouse islets transduced with SNAP/FLAG-*hGlp1r* ^{WT} *versus* ^{A316T} adenoviruses. a,**b**, Surface expression in islets from *hGlp1r* $^{-/-}$ mice transduced with pAV-SNAP/FLAG-*hGlp1r* ^{WT} or ^{A316T} labelled with SNAP-Surface Alexa Fluor 647. Representative images (**a**) and quantification of surface GLP-1R (**b**); size bars, 20 μm; *n* = 9. **c-f**, Ca^{2+} responses from Cal-520 AM-loaded *hGlp1r* $^{-/-}$ mouse islets previously transduced with pAV-SNAP/FLAG-*hGlp1r* ^{WT} or ^{A316T} and subsequently stimulated with 100 nM GLP-1 (**c**), exendin-4 (Ex-4) (**d**), exendin-F1 (Ex-F1) (**e**), or semaglutide (Sema) (**f**), followed by 20 mM KCl for maximal responses; Ca^{2+} traces and corresponding AUCs for agonist responses at 6 mM (G6) and 11 mM glucose (G11) shown; *n* = 3-4. **g**,**h**, ΔAUC (SNAP/FLAG-*hGlp1r* ^{A316T} minus ^{WT}) responses at G6 (**g**) or G11 (**h**), calculated from data in (**c-f**). Data are mean ± SEM except for ΔAUC *hGlp1r* ^{A316T} minus ^{WT} responses which are mean ± 95% confidence interval (CI); *p<0.05; ***p<0.001; ns, not significant by paired or ratio paired t-tests.

Extended Data Fig. 7. Functional characterisation of INS-1 832/3 *hGlp1r* $^{-/-}$ SNAP/FLAG-*hGlp1r* ^{WT} *versus* ^{A316T} sublines – extra data. a, Percentage of GLP-1R internalisation over time following stimulation with the indicated agonists in INS-1 832/3 *hGlp1r* $^{-/-}$ SNAP/FLAG-*hGlp1r* ^{WT} *versus* ^{A316T} cells;

n = 3. **b**, Internalisation AUCs calculated from (**a**). **c**, Percentage of GLP-1R recycling to the plasma membrane over time following stimulation with the indicated agonists in INS-1 832/3 *hGlp1r* $^{-/-}$ SNAP/FLAG-*hGlp1r* ^{WT} *versus* ^{A316T} cells; *n* = 3. **d**, Recycling AUCs calculated from (**c**). **e**, Percentage of GLP-1R degradation over time following stimulation with the indicated agonists in INS-1 832/3 *hGlp1r* $^{-/-}$ SNAP/FLAG-*hGlp1r* ^{WT} *versus* ^{A316T} cells; *n* = 3. **f**, Degradation AUCs calculated from (**e**). **g**, Vehicle-subtracted LgBiT-mini-G_s recruitment to *hGlp1r* ^{WT} or ^{A316T}-SmBiT over time in INS-1 832/3 *hGlp1r* $^{-/-}$ cells following stimulation with 100 nM of the indicated agonist; *n* = 5. **h**, LgBiT-mini-G_s recruitment to *hGlp1r* ^{WT} or ^{A316T}-SmBiT AUC dose responses to the indicated agonist; *n* = 5. **i**, Vehicle-subtracted LgBiT-β-arrestin 2 (βarr2) recruitment to *hGlp1r* ^{WT} or ^{A316T}-SmBiT over time in INS-1 832/3 *hGlp1r* $^{-/-}$ cells following stimulation with 100 nM of the indicated agonist; *n* = 5. **j**, LgBiT-βarr2 recruitment to *hGlp1r* ^{WT} or ^{A316T}-SmBiT AUC dose responses to the indicated agonist; *n* = 5. **k**-**n**, cAMP responses from cADDis transduced INS-1 832/3 *hGlp1r* $^{-/-}$ SNAP/FLAG-*hGlp1r* ^{WT} *versus* ^{A316T} cells in response to 100 nM GLP-1 (**k**), exendin-4 (Ex-4) (**l**), exendin-F1 (Ex-F1) (**m**), or semaglutide (Sema) (**n**), followed by IBMX plus forskolin (FSK) stimulation for maximal responses; *n* = 4. **o**,**p**, cAMP AUCs (**o**) or ΔAUC (SNAP/FLAG-*hGlp1r* ^{A316T} minus ^{WT}) (**p**) calculated from agonist-stimulated periods in (**k**-**n**); *n* = 4. Data are mean ± SEM except for ΔAUC *hGlp1r* ^{A316T} minus ^{WT} responses which are mean ± 95% confidence interval (CI); *p<0.05; ns, not significant by two-way ANOVA with Sidak's post-hoc tests.

Extended Data Fig. 8. Molecular characterisation of GLP-1R behaviours in INS-1 832/3 *hGlp1r* $^{-/-}$ SNAP/FLAG-*hGlp1r* ^{WT} *versus* ^{A316T} sublines. a, Baseline endosomal over plasma membrane GLP-1R activity, measured by SmBiT-nb37 complementation with Endofin-LgBiT over LgBiT-CAAX under vehicle conditions in INS-1 832/3 *hGlp1r* $^{-/-}$ SNAP/FLAG-*hGlp1r* ^{WT} *versus* ^{A316T} cells; AUCs also shown; *n* = 12. **b**, AUC dose response curves and log(E_{max}/EC_{50}) of plasma membrane and endosomal GLP-1R activity in response to GLP-1 stimulation, measured by SmBiT-nb37 complementation with LgBiT-CAAX and Endofin-LgBiT in INS-1 832/3 *hGlp1r* $^{-/-}$ SNAP/FLAG-*hGlp1r* ^{WT} *versus* ^{A316T} cells; *n* = 4. **c**, Baseline GLP-1R ECD opening, measured by SNAP-Lumi4-Tb - NR12A TR-FRET over time under

vehicle conditions in INS-1 832/3 *hGlp1r* $^{-/-}$ SNAP/FLAG-*hGlp1r* ^{WT} *versus* ^{A316T} cells; AUCs also shown; *n* = 5. **d**, AUC dose response curves and log(E_{max}/EC_{50}) of GLP-1R ECD opening in response to GLP-1 stimulation, measured by SNAP-Lumi4-Tb - NR12A TR-FRET increases over time in INS-1 832/3 *hGlp1r* $^{-/-}$ SNAP/FLAG-*hGlp1r* ^{WT} *versus* ^{A316T} cells; *n* = 5. **e**, Representative blots showing SNAP/FLAG-*hGlp1r* recruitment to DRM fractions (or lipid rafts) from INS-1 832/3 *hGlp1r* $^{-/-}$ SNAP/FLAG-*hGlp1r* ^{WT} *versus* ^{A316T} cells following stimulation for 2 minutes with the indicated agonist, with flotillin used as DRM loading control; quantification of surface expression (SE)-corrected baseline SNAP/FLAG-*hGlp1r* ^{WT} *versus* ^{A316T} DRM levels under vehicle conditions also shown; *n* = 5. **f**, SNAP/FLAG-*hGlp1r* ^{WT} *versus* ^{A316T} DRM recruitment fold changes to vehicle (Veh), quantified from (**e**); *n* = 5. **g**, Representative images from RICS analysis of GLP-1R WT and A316T plasma membrane lateral diffusion in INS-1 832/3 *hGlp1r* $^{-/-}$ SNAP/FLAG-*hGlp1r* ^{WT} *versus* ^{A316T} cells labelled with SNAP-Surface Alexa Fluor 647 and subsequently stimulated with vehicle (Veh) or 100 nM exendin-4 (Ex-4). **h**,**i**, GLP-1R WT *versus* A316T average RICS diffusion coefficients (**h**) and vehicle (Veh) fold changes (**i**); *n* = 4. **j**, Representative blots showing SNAP/FLAG-*hGlp1r* ubiquitination following anti-FLAG immunoprecipitation in INS-1 832/3 *hGlp1r* $^{-/-}$ SNAP/FLAG-*hGlp1r* ^{WT} *versus* ^{A316T} cells under vehicle (Veh) or 100 nM exendin-4 (Ex-4) stimulation for 10 minutes; quantification of GLP-1R ubiquitination and vehicle (Veh) fold changes also shown; *n* = 4.

Extended Data Fig. 9. GLP-1R WT *versus* A316T interactome analysis in INS-1 832/3 *hGlp1r* $^{-/-}$ SNAP/FLAG-*hGlp1r* ^{WT} *versus* ^{A316T} cells. Heatmap of GLP-1R interactor enrichment from LC-MS/MS analysis of INS-1 832/3 *hGlp1r* $^{-/-}$ SNAP/FLAG-*hGlp1r* ^{WT} *versus* ^{A316T} anti-FLAG co-immunoprecipitates under vehicle (Veh) or 5 minutes stimulation with exendin-4 (Ex-4) or GLP-1; blue, decreased; pink, increased interactor enrichment; LC-MS/MS data analysed in LFQ-Analyst and normalized to hGLP-1R levels for each experimental repeat; *n* = 2-4.

Extended Data Fig. 10. MD simulations of GLP-1R A316T TMD. a, GLP-1R structure used in MD simulations: only the TMD, ECL2, ECL3, and ICLs were retained to highlight the subtle allosteric effect exerted by A316T. **b**, Comparison between GLP-1R WT and A316T TMD. The side chain of Y242$^{3.45}$ forms a persistent HB with the backbone of P312$^{5.42}$ in WT GLP-1R (left), while in A316T the side chain of T316$^{5.46}$ engages Y242$^{3.45}$ (right); as a result of this HB reshuffling, the TM3-TM5 interhelical distance at the L245$^{3.48}$ -V319$^{5.49}$ level (d1) increases from 7.58 ± 0.28 Å to 8.09 ± 0.34 Å, while the TM3-TM5 interhelical distance at the L251$^{3.54}$ -V327$^{5.57}$ level (d2) decreases from 8.91 ± 0.68 Å to 7.75 ± 0.48 Å; this is accompanied by a stabilisation of the intracellular side of TM5 due to a more persistent HB between Y252$^{3.55}$ and R326$^{5.56}$. **c**, TM5-TM6 interhelical distances, d1 and d2. **d**, In A316T, TM6 dynamics is accentuated and the characteristic, active state opening of TM6 (TM6 swing) increases by ~2.5 Å compared to WT [25.12 ± 1.80 Å (WT GLP-1R) *versus* 27.65 ± 2.02 Å (A316T GLP-1R)]. **e**, Proposed dynamic model for the enhanced constitutive activity of GLP-1R A316T.

References

1. Tornehave, D., Kristensen, P., Rømer, J., Knudsen, L.B. & Heller, R.S. Expression of the GLP-1 receptor in mouse, rat, and human pancreas. *Journal of Histochemistry and Cytochemistry* **56**, 841-851 (2008).
2. Ast, J. *et al.* Revealing the tissue-level complexity of endogenous glucagon-like peptide-1 receptor expression and signaling. *Nature Communications 2023 14:1* **14**, 1-15 (2023).
3. Donnelly, D. The structure and function of the glucagon-like peptide-1 receptor and its ligands. *British Journal of Pharmacology* **166**, 27-27 (2012).
4. Holst, J.J. & Ørskov, C. The incretin approach for diabetes treatment: modulation of islet hormone release by GLP-1 agonism. *Diabetes* **53 Suppl 3** (2004).
5. Garvey, W.T. *et al.* Two-year effects of semaglutide in adults with overweight or obesity: the STEP 5 trial. *Nat Med* **28**, 2083-2091 (2022).
6. Davies, M. *et al.* Semaglutide 2.4 mg once a week in adults with overweight or obesity, and type 2 diabetes (STEP 2): a randomised, double-blind, double-dummy, placebo-controlled, phase 3 trial. *Lancet* **397**, 971-984 (2021).
7. Zhang, Y. *et al.* Cryo-EM structure of the activated GLP-1 receptor in complex with G protein. *Nature* **546**, 248-248 (2017).
8. Deganutti, G. *et al.* Dynamics of GLP-1R peptide agonist engagement are correlated with kinetics of G protein activation. *Nature communications* **13** (2022).

9. Kang, G. *et al.* Epac-selective cAMP analog 8-pCPT-2'-O-Me-cAMP as a stimulus for Ca2+-induced Ca2+ release and exocytosis in pancreatic beta-cells. *The Journal of biological chemistry* **278**, 8279-8285 (2003).

10. Chen, X.Y., Chen, L., Yang, W. & Xie, A.M. GLP-1 Suppresses Feeding Behaviors and Modulates Neuronal Electrophysiological Properties in Multiple Brain Regions. *Frontiers in Molecular Neuroscience* **14** (2021).

11. Wang, B. *et al.* Blood pressure-lowering effects of GLP-1 receptor agonists exenatide and liraglutide: A meta-analysis of clinical trials. *Diabetes, Obesity and Metabolism* **15**, 737-749 (2013).

12. Goud, A., Zhong, J., Peters, M., Brook, R.D. & Rajagopalan, S. GLP-1 Agonists and Blood Pressure: A Review of the Evidence. *Current hypertension reports* **18**, 1-11 (2016).

13. Rieg, T. *et al.* Natriuretic effect by exendin-4, but not the DPP-4 inhibitor alogliptin, is mediated via the GLP-1 receptor and preserved in obese type 2 diabetic mice. *American Journal of Physiology - Renal Physiology* **303**, 963-971 (2012).

14. Crajoinas, R.O. *et al.* Mechanisms mediating the diuretic and natriuretic actions of the incretin hormone glucagon-like peptide-1. *American Journal of Physiology - Renal Physiology* **301**, 355-363 (2011).

15. Hansen, H.H. *et al.* The GLP-1 Receptor Agonist Liraglutide Improves Memory Function and Increases Hippocampal CA1 Neuronal Numbers in a Senescence-Accelerated Mouse Model of Alzheimer's Disease. *Journal of Alzheimer's Disease* **46**, 877-888 (2015).

16. During, M.J. *et al.* Glucagon-like peptide-1 receptor is involved in learning and neuroprotection. *Nature medicine* **9**, 1173-1179 (2003).

17. Reich, N. & Hölscher, C. The neuroprotective effects of glucagon-like peptide 1 in Alzheimer's and Parkinson's disease: An in-depth review. *Frontiers in neuroscience* **16** (2022).

18. Ghosh, P. *et al.* Targeting redox imbalance in neurodegeneration: characterizing the role of GLP-1 receptor agonists. *Theranostics* **13**, 4872-4884 (2023).

19. Dawed, A.Y. *et al.* Pharmacogenomics of GLP-1 receptor agonists: a genome-wide analysis of observational data and large randomised controlled trials. *The Lancet Diabetes & Endocrinology* **11**, 33-41 (2023).

20. Hauser, A.S. *et al.* Pharmacogenomics of GPCR Drug Targets. *Cell* **172**, 41-41 (2018).

21. Wessel, J. *et al.* Low-frequency and rare exome chip variants associate with fasting glucose and type 2 diabetes susceptibility. *Nature Communications 2015 6:1* **6**, 1-16 (2015).

22. Scott, R.A. *et al.* Genomic approach to therapeutic target validation identifies a glucose-lowering GLP1R variant protective for coronary heart disease. *Science translational medicine* **8**, 341ra376-341ra376 (2016).

23. Lagou, V. *et al.* GWAS of random glucose in 476,326 individuals provide insights into diabetes pathophysiology, complications and treatment stratification. *Nature Genetics* **55**, 1448-1448 (2023).

24. Handley, D. *et al.* Rare variants of the glucagon-like peptide-1 receptor (GLP1R) gene are overrepresented in a severe obesity cohort and associated with type 2 diabetes in the UK Biobank. *medRxiv*, 2023.2005.2022.23290347-23292023.23290305.23290322.23290347 (2023).

25. Li, W. *et al.* GLP1R Single-Nucleotide Polymorphisms rs3765467 and rs10305492 Affect β Cell Insulin Secretory Capacity and Apoptosis through GLP-1. *DNA and Cell Biology* **39**, 1700-1710 (2020).

26. Koole, C. *et al.* Polymorphism and ligand dependent changes in human glucagon-like peptide-1 receptor (GLP-1R) function: Allosteric rescue of loss of function mutation. *Molecular Pharmacology* **80**, 486-497 (2011).

27. El Eid, L., Reynolds, C.A., Tomas, A. & Ben, J. Biased agonism and polymorphic variation at the GLP-1 receptor: Implications for the development of personalised therapeutics. *Pharmacological Research* **184**, 106411-106411 (2022).

28. Gao, W. *et al.* Human GLP1R variants affecting GLP1R cell surface expression are associated with impaired glucose control and increased adiposity. *Nature metabolism* **5** (2023).

29. Jun, L.S. *et al.* A novel humanized GLP-1 receptor model enables both affinity purification and Cre-LoxP deletion of the receptor. *PLoS One* **9**, e93746 (2014).

30. Jones, B. *et al.* Targeting GLP-1 receptor trafficking to improve agonist efficacy. *Nat Commun* **9**, 1602 (2018).

31. Clark, L. GLP-1 receptor agonists: A review of glycemic benefits and beyond. *JAAPA* **37**, 1-4 (2024).

32. Xie, J. *et al.* Exendin-4 stimulates islet cell replication via the IGF1 receptor activation of mTORC1/S6K1. *Journal of Molecular Endocrinology* **53**, 105-115 (2014).

33. Hui, H., Nourparvar, A., Zhao, X. & Perfetti, R. Glucagon-Like Peptide-1 Inhibits Apoptosis of Insulin-Secreting Cells via a Cyclic 5′-Adenosine Monophosphate-Dependent Protein Kinase A- and a Phosphatidylinositol 3-Kinase-Dependent Pathway. *Endocrinology* **144**, 1444-1455 (2003).

34. Ling, Z. *et al.* Glucagon-like peptide 1 receptor signaling influences topography of islet cells in mice. *Virchows Archiv* **438**, 382-387 (2001).

35. Portha, B., Tourrel-Cuzin, C. & Movassat, J. Activation of the GLP-1 Receptor Signalling Pathway: A Relevant Strategy to Repair a Deficient Beta-Cell Mass. *Experimental Diabetes Research* **2011**, 376509-376509 (2011).

36. Shrestha, S. *et al.* Aging compromises human islet beta cell function and identity by decreasing transcription factor activity and inducing ER stress. *Science Advances* **8** (2022).

37. Bartolomé, A. *et al.* Notch-mediated Ephrin signaling disrupts islet architecture and β cell function. *JCI insight* **7** (2022).

38. Hu, F., Qiu, X. & Bu, S. Pancreatic islet dysfunction in type 2 diabetes mellitus. *Archives of Physiology and Biochemistry* **126**, 235-241 (2020).

39. Lv, C.G., Wang, R.R. & Meng, Z.X. Molecular mechanism of islet β-cell functional alternations during type 2 diabetes. *Yi chuan = Hereditas* **44 10**, 840-852 (2022).

40. Saikia, M. *et al.* GLP-1 receptor signaling increases PCSK1 and β cell features in human α cells. *JCI insight* **6** (2021).

41. Holter, M. *et al.* 366-OR: 14-3-3-ζ Contributes to Effect of ß-Cell GLP1 Receptor Signaling to Alter a-Cell Proglucagon Processing. *Diabetes* **71** (2022).

42. Zhang, Z. *et al.* A New Way for Beta Cell Neogenesis: Transdifferentiation from Alpha Cells Induced by Glucagon-Like Peptide 1. *Experimental Diabetes Research* **2019**, 2583047-2583047 (2019).

43. Lee, Y.S., Lee, C., Choung, J.S., Jung, H.S. & Jun, H.S. Glucagon-Like Peptide 1 Increases β-Cell Regeneration by Promoting α- to β-Cell Transdifferentiation. *Diabetes* **67**, 2601-2614 (2018).

44. Holter, M.M., Saikia, M. & Cummings, B.P. Alpha-cell paracrine signaling in the regulation of beta-cell insulin secretion. *Frontiers in Endocrinology* **13** (2022).

45. Chakravarthy, H. *et al.* Converting Adult Pancreatic Islet α Cells into β Cells by Targeting Both Dnmt1 and Arx. *Cell Metabolism* **25**, 622-634 (2017).

46. Martinez-Sanchez, A. *et al.* Disallowance of Acot7 in beta-Cells Is Required for Normal Glucose Tolerance and Insulin Secretion. *Diabetes* **65**, 1268-1282 (2016).

47. Cattani-Cavalieri, I., Margolis, J., Anicolaesei, C., Nunez, F.J. & Ostrom, R.S. Real-Time cAMP Dynamics in Live Cells Using the Fluorescent cAMP Difference Detector In Situ. *J Vis Exp* (2024).

48. Greenhill, C. GWAS gives insights into glucose regulation. *Nat Rev Endocrinol* **19**, 684 (2023).

49. Benazra, M. *et al.* A human beta cell line with drug inducible excision of immortalizing transgenes. *Molecular metabolism* **4**, 916-925 (2015).

50. Naylor, J. *et al.* Use of CRISPR/Cas9-engineered INS-1 pancreatic beta cells to define the pharmacology of dual GIPR/GLP-1R agonists. *Biochem J* **473**, 2881-2891 (2016).

51. Ast, J. *et al.* Revealing the tissue-level complexity of endogenous glucagon-like peptide-1 receptor expression and signaling. *Nat Commun* **14**, 301 (2023).

52. Yamamoto, A. *et al.* Bafilomycin A1 prevents maturation of autophagic vacuoles by inhibiting fusion between autophagosomes and lysosomes in rat hepatoma cell line, H-4-II-E cells. *Cell Struct Funct* **23**, 33-42 (1998).

53. Manchanda, Y. *et al.* Engineered mini-G proteins block the internalization of cognate GPCRs and disrupt downstream intracellular signaling. *Sci Signal* **17**, eabq7038 (2024).

54. Zhang, X. *et al.* Differential GLP-1R Binding and Activation by Peptide and Non-peptide Agonists. *Molecular Cell* **80**, 485-500.e487 (2020).

55. Liang, Y.L. *et al.* Toward a Structural Understanding of Class B GPCR Peptide Binding and Activation. *Molecular cell* **77**, 656-668.e655 (2020).

56. Buenaventura, T. *et al.* Agonist-induced membrane nanodomain clustering drives GLP-1 receptor responses in pancreatic beta cells. *PLOS Biology* **17**, e3000097-e3000097 (2019).

57. Manchanda, Y. *et al.* Enhanced Endosomal Signaling and Desensitization of GLP-1R vs GIPR in Pancreatic Beta Cells. *Endocrinology* **164** (2023).

58. Oqua, A.I. *et al.*, Molecular mapping and functional validation of GLP-1R cholesterol binding sites in pancreatic beta cells. *eLife* **13**:RP101011 (2024).

59. Bitsi, S. *et al.* Divergent acute versus prolonged pharmacological GLP-1R responses in adult β cell–specific β-arrestin 2 knockout mice. *Science Advances* **9** (2023).

60. Dores, M.R. & Trejo, J. Endo-lysosomal sorting of G-protein-coupled receptors by ubiquitin: Diverse pathways for G-protein-coupled receptor destruction and beyond. *Traffic* **20**, 101-109 (2019).

61. Austin, G. *et al.* An inter-organelle contact between endosomal GLP-1R, ER VAP-B, and the mitochondrial AKAP SPHKAP triggers PKA-dependent MIC19 phosphorylation and β-cell mitochondrial remodelling. *bioRxiv*, 2024.2004.2028.591531-592024.591504.591528.591531 (2024).

62. Cong, Z. *et al.* Structural perspective of class B1 GPCR signaling. *Trends in Pharmacological Sciences* **43**, 321-334 (2022).

63. Punjani, A. & Fleet, D.J. 3D variability analysis: Resolving continuous flexibility and discrete heterogeneity from single particle cryo-EM. *Journal of Structural Biology* **213**, 107702-107702 (2021).

64. Lagou, V. *et al.* GWAS of random glucose in 476,326 individuals provide insights into diabetes pathophysiology, complications and treatment stratification. *Nat Genet* **55**, 1448-1461 (2023).

65. Weis, W.I. & Kobilka, B.K. The Molecular Basis of G Protein-Coupled Receptor Activation. *Annual Review of Biochemistry* **87**, 897-919 (2018).

66. Balasubramanian, S., Xia, Y., Freinkman, E. & Gerstein, M. Sequence variation in G-protein-coupled receptors: analysis of single nucleotide polymorphisms. *Nucleic Acids Res* **33**, 1710-1721 (2005).

67. Austin, G.O. & Tomas, A. Variation in responses to incretin therapy: Modifiable and non-modifiable factors. *Front Mol Biosci* **10**, 1170181 (2023).

68. Hinds, C.E. *et al.* Abolishing β-arrestin recruitment is necessary for the full metabolic benefits of G protein-biased glucagon-like peptide-1 receptor agonists. *Diabetes, Obesity and Metabolism* **26**, 65-77 (2024).

69. Katahira, T. *et al.* Conversion of pancreatic α cells into insulin-producing cells modulated by β-cell insufficiency and supplemental insulin administration. *Biochemical and Biophysical Research Communications* **521**, 178-183 (2020).

70. de Souza, A.H. *et al.* Intra-islet GLP-1, but not CCK, is necessary for β-cell function in mouse and human islets. *Scientific Reports 2020 10:1* **10**, 1-10 (2020).

71. Koole, C. *et al.* Polymorphism and ligand dependent changes in human glucagon-like peptide-1 receptor (GLP-1R) function: allosteric rescue of loss of function mutation. *Mol Pharmacol* **80**, 486-497 (2011).

72. Buenaventura, T. *et al.* Agonist-induced membrane nanodomain clustering drives GLP-1 receptor responses in pancreatic beta cells. *PLoS Biol* **17**, e3000097 (2019).

73. Wootten, D., Simms, J., Miller, L.J., Christopoulos, A. & Sexton, P.M. Polar transmembrane interactions drive formation of ligand-specific and signal pathway-biased family B G protein-coupled receptor conformations. *Proceedings of the National Academy of Sciences of the United States of America* **110**, 5211-5216 (2013).

74. Wootten, D. *et al.* The Extracellular Surface of the GLP-1 Receptor Is a Molecular Trigger for Biased Agonism. *Cell* **165**, 1632-1643 (2016).

75. Lei, S. *et al.* Two distinct domains of the glucagon-like peptide-1 receptor control peptide-mediated biased agonism. *Journal of Biological Chemistry* **293**, 9370-9387 (2018).

76. Li, B. *et al.* Structure and Molecular Mechanism of Signaling for the Glucagon-like Peptide-1 Receptor Bound to Gs Protein and Exendin-P5 Biased Agonist. *Journal of the American Chemical Society* **145**, 20422-20431 (2023).

77. Bitsi, S. *et al.* Divergent acute versus prolonged pharmacological GLP-1R responses in adult beta cell-specific beta-arrestin 2 knockout mice. *Sci Adv* **9**, eadf7737 (2023).

78. Kors, S., Costello, J.L. & Schrader, M. VAP Proteins - From Organelle Tethers to Pathogenic Host Interactors and Their Role in Neuronal Disease. *Front Cell Dev Biol* **10**, 895856 (2022).

79. Means, C.K. *et al.* An entirely specific type I A-kinase anchoring protein that can sequester two molecules of protein kinase A at mitochondria. *Proc Natl Acad Sci U S A* **108**, E1227-1235 (2011).

80. Celen, A.B. & Sahin, U. Sumoylation on its 25th anniversary: mechanisms, pathology, and emerging concepts. *FEBS J* **287**, 3110-3140 (2020).

81. Zhang, X. *et al.* Structure and dynamics of semaglutide- and taspoglutide-bound GLP-1R-Gs complexes. *Cell Reports* **36**, 109374-109374 (2021).

82. Cuzzolin, A., Deganutti, G., Salmaso, V., Sturlese, M. & Moro, S. AquaMMapS: An Alternative Tool to Monitor the Role of Water Molecules During Protein-Ligand Association. *ChemMedChem* **13**, 522-531 (2018).

83. Clardy, S.M. *et al.* Fluorescent exendin-4 derivatives for pancreatic beta-cell analysis. *Bioconjug Chem* **25**, 171-177 (2014).

84. Lucey, M. *et al.* Acylation of the Incretin Peptide Exendin-4 Directly Impacts Glucagon-Like Peptide-1 Receptor Signaling and Trafficking. *Molecular Pharmacology* **100**, 319-334 (2021).

85. Ast, J. *et al.* Super-resolution microscopy compatible fluorescent probes reveal endogenous glucagon-like peptide-1 receptor distribution and dynamics. *Nature Communications 2020 11:1* **11**, 1-18 (2020).

86. Fang, Z. *et al.* The Influence of Peptide Context on Signaling and Trafficking of Glucagon-like Peptide-1 Receptor Biased Agonists. *ACS Pharmacology & Translational Science* **3**, 345-360 (2020).

87. Jones, B. *et al.* Genetic and biased agonist-mediated reductions in beta-arrestin recruitment prolong cAMP signaling at glucagon family receptors. *J Biol Chem* **296**, 100133 (2021).

88. Manchanda, Y. *et al.* Enhanced Endosomal Signaling and Desensitization of GLP-1R vs GIPR in Pancreatic Beta Cells. *Endocrinology* **164**, 1-15 (2023).

89. Wan, Q. *et al.* Mini G protein probes for active G protein-coupled receptors (GPCRs) in live cells. *J Biol Chem* **293**, 7466-7473 (2018).

90. Shintani, Y. *et al.* beta-Arrestin1 and 2 differentially regulate PACAP-induced PAC1 receptor signaling and trafficking. *PLoS One* **13**, e0196946 (2018).

91. Johnston, N.R. *et al.* Beta Cell Hubs Dictate Pancreatic Islet Responses to Glucose. *Cell metabolism* **24**, 389-401 (2016).

92. Bru-Tari, E. *et al.* Pancreatic alpha-cell mass in the early-onset and advanced stage of a mouse model of experimental autoimmune diabetes. *Scientific reports* **9** (2019).

93. Bitsi, S. *et al.* Divergent acute versus prolonged in vivo GLP-1R responses in β-arrestin 2-deleted primary beta cells. *bioRxiv*, 2022.2004.2021.489075-482022.489004.489021.489075 (2022).

94. Miguel-Escalada, I. *et al.* Human pancreatic islet three-dimensional chromatin architecture provides insights into the genetics of type 2 diabetes. *Nat Genet* **51**, 1137-1148 (2019).

95. Brown, L.Y., Dong, W. & Kantor, B. An Improved Protocol for the Production of Lentiviral Vectors. *STAR Protoc* **1**, 100152 (2020).

96. Peng, T. *et al.* A BaSiC tool for background and shading correction of optical microscopy images. *Nature communications* **8** (2017).

97. Jaccard, N. *et al.* Automated method for the rapid and precise estimation of adherent cell culture characteristics from phase contrast microscopy images. *Biotechnology and Bioengineering* **111**, 504-517 (2014).

98. Riahi, Y. *et al.* Autophagy is a major regulator of beta cell insulin homeostasis. *Diabetologia* **59**, 1480-1491 (2016).

99. Livak, K.J. & Schmittgen, T.D. Analysis of relative gene expression data using real-time quantitative PCR and the 2(-Delta Delta C(T)) Method. *Methods (San Diego, Calif.)* **25**, 402-408 (2001).

100. Liang, Y.L. *et al.* Phase-plate cryo-EM structure of a class B GPCR–G-protein complex. *Nature 2017 546:7656* **546**, 118-123 (2017).

101. Fernandez-Leiro, R. & Scheres, S.H.W. A pipeline approach to single-particle processing in RELION. *Acta Crystallographica Section D: Structural Biology* **73**, 496-502 (2017).

102. Wagner, T. *et al.* SPHIRE-crYOLO is a fast and accurate fully automated particle picker for cryo-EM. *Communications Biology 2019 2:1* **2**, 1-13 (2019).

103. Punjani, A., Rubinstein, J.L., Fleet, D.J. & Brubaker, M.A. cryoSPARC: algorithms for rapid unsupervised cryo-EM structure determination. *Nature Methods 2017 14:3* **14**, 290-296 (2017).

104. Croll, T.I. ISOLDE: A physically realistic environment for model building into low-resolution electron-density maps. *Acta Crystallographica Section D: Structural Biology* **74**, 519-530 (2018).

105. Pettersen, E.F. *et al.* UCSF Chimera—A visualization system for exploratory research and analysis. *Journal of Computational Chemistry* **25**, 1605-1612 (2004).

106. Liebschner, D. *et al.* Macromolecular structure determination using X-rays, neutrons and electrons: recent developments in Phenix. *urn:issn:2059-7983* **75**, 861-877 (2019).

107. Deganutti, G. *et al.* Dynamics of GLP-1R peptide agonist engagement are correlated with kinetics of G protein activation. *Nat Commun* **13**, 92 (2022).

108. Lomize, M.A., Lomize, A.L., Pogozheva, I.D. & Mosberg, H.I. OPM: Orientations of Proteins in Membranes database. *Bioinformatics* **22**, 623-625 (2006).

109. Huang, J. & Mackerell, A.D. CHARMM36 all-atom additive protein force field: Validation based on comparison to NMR data. *Journal of Computational Chemistry* **34**, 2135-2145 (2013).

110. Doerr, S., Harvey, M.J., Noé, F. & De Fabritiis, G. HTMD: High-Throughput Molecular Dynamics for Molecular Discovery. *Journal of Chemical Theory and Computation* **12**, 1845-1852 (2016).

111. Dolinsky, T.J., Nielsen, J.E., McCammon, J.A. & Baker, N.A. PDB2PQR: an automated pipeline for the setup of Poisson–Boltzmann electrostatics calculations. *Nucleic Acids Research* **32**, W665-W667 (2004).

112. Olsson, M.H.M., SØndergaard, C.R., Rostkowski, M. & Jensen, J.H. PROPKA3: Consistent treatment of internal and surface residues in empirical p K a predictions. *Journal of Chemical Theory and Computation* **7**, 525-537 (2011).

113. Sommer, B. MEMBRANE PACKING PROBLEMS: A SHORT REVIEW ON COMPUTATIONAL MEMBRANE MODELING METHODS AND TOOLS. *Computational and Structural Biotechnology Journal* **5**, e201302014-e201302014 (2013).

114. Jorgensen, W.L., Chandrasekhar, J., Madura, J.D., Impey, R.W. & Klein, M.L. Comparison of simple potential functions for simulating liquid water. *The Journal of Chemical Physics* **79**, 926-935 (1983).

115. Harvey, M.J., Giupponi, G. & De Fabritiis, G. ACEMD: Accelerating biomolecular dynamics in the microsecond time scale. *Journal of Chemical Theory and Computation* **5**, 1632-1639 (2009).

116. Berendsen, H.J.C., Postma, J.P.M., Van Gunsteren, W.F., Dinola, A. & Haak, J.R. Molecular dynamics with coupling to an external bath. *The Journal of Chemical Physics* **81**, 3684-3690 (1984).

117. Loncharich, R.J., Brooks, B.R. & Pastor, R.W. Langevin dynamics of peptides: The frictional dependence of isomerization rates of N-acetylalanyl-N′-methylamide. *Biopolymers* **32**, 523-535 (1992).

118. Kräutler, V., Van Gunsteren, W.F. & Hünenberger, P.H. A Fast SHAKE Algorithm to Solve Distance Constraint Equations for Small Molecules in Molecular Dynamics Simulations. *J Comput Chem* **22**, 501-508 (2001).

119. Essmann, U. *et al.* A smooth particle mesh Ewald method. *The Journal of Chemical Physics* **103**, 8577-8593 (1995).

120. Fiser, A. & Šali, A. Modeller: Generation and Refinement of Homology-Based Protein Structure Models. *Methods in Enzymology* **374**, 461-491 (2003).

121. McGibbon, R.T. *et al.* MDTraj: A Modern Open Library for the Analysis of Molecular Dynamics Trajectories. *Biophysical Journal* **109**, 1528-1532 (2015).

122. Humphrey, W., Dalke, A. & Schulten, K. VMD: Visual molecular dynamics. *Journal of Molecular Graphics* **14**, 33-38 (1996).

123. Zhang, X. *et al.* Differential GLP-1R Binding and Activation by Peptide and Non-peptide Agonists. *Mol Cell* **80**, 485-500 e487 (2020).

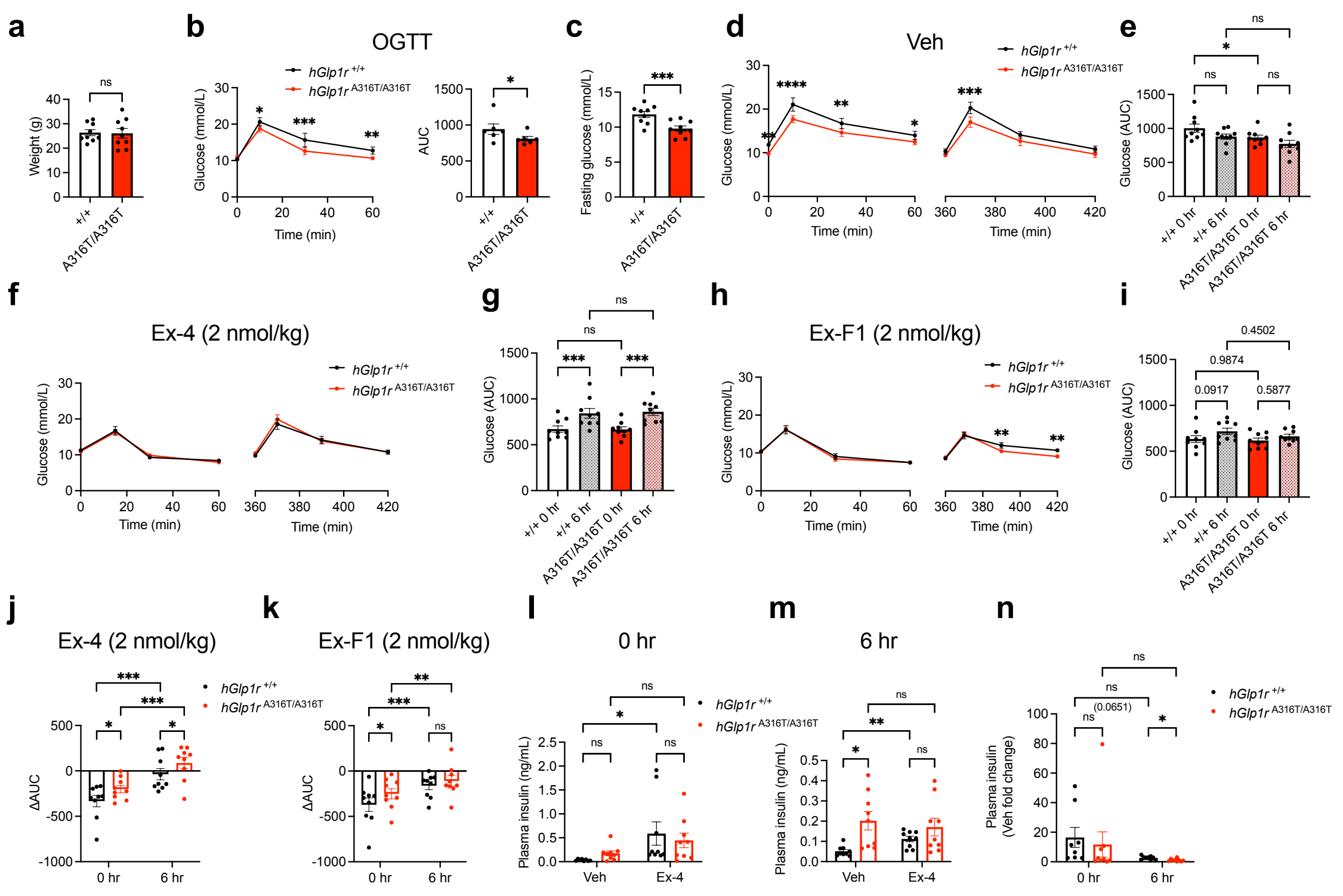
a
Weight (g)
ns
+/+
A316T/A316T
b
OGTT
Glucose (mmol/L)
Time (min)
hGlp1r +/+
hGlp1r A316T/A316T
AUC
c
Fasting glucose (mmol/L)
d
Veh
e
Glucose (AUC)
+/+ 0 hr
+/+ 6 hr
A316T/A316T 0 hr
A316T/A316T 6 hr
f
Ex-4 (2 nmol/kg)
g
h
Ex-F1 (2 nmol/kg)
i
0.4502
0.9874
0.0917
0.5877
j
Ex-4 (2 nmol/kg)
ΔAUC
0 hr
6 hr
k
Ex-F1 (2 nmol/kg)
l
0 hr
Plasma insulin (ng/mL)
Veh
Ex-4
m
6 hr
n
Plasma insulin (Veh fold change)
(0.0651)

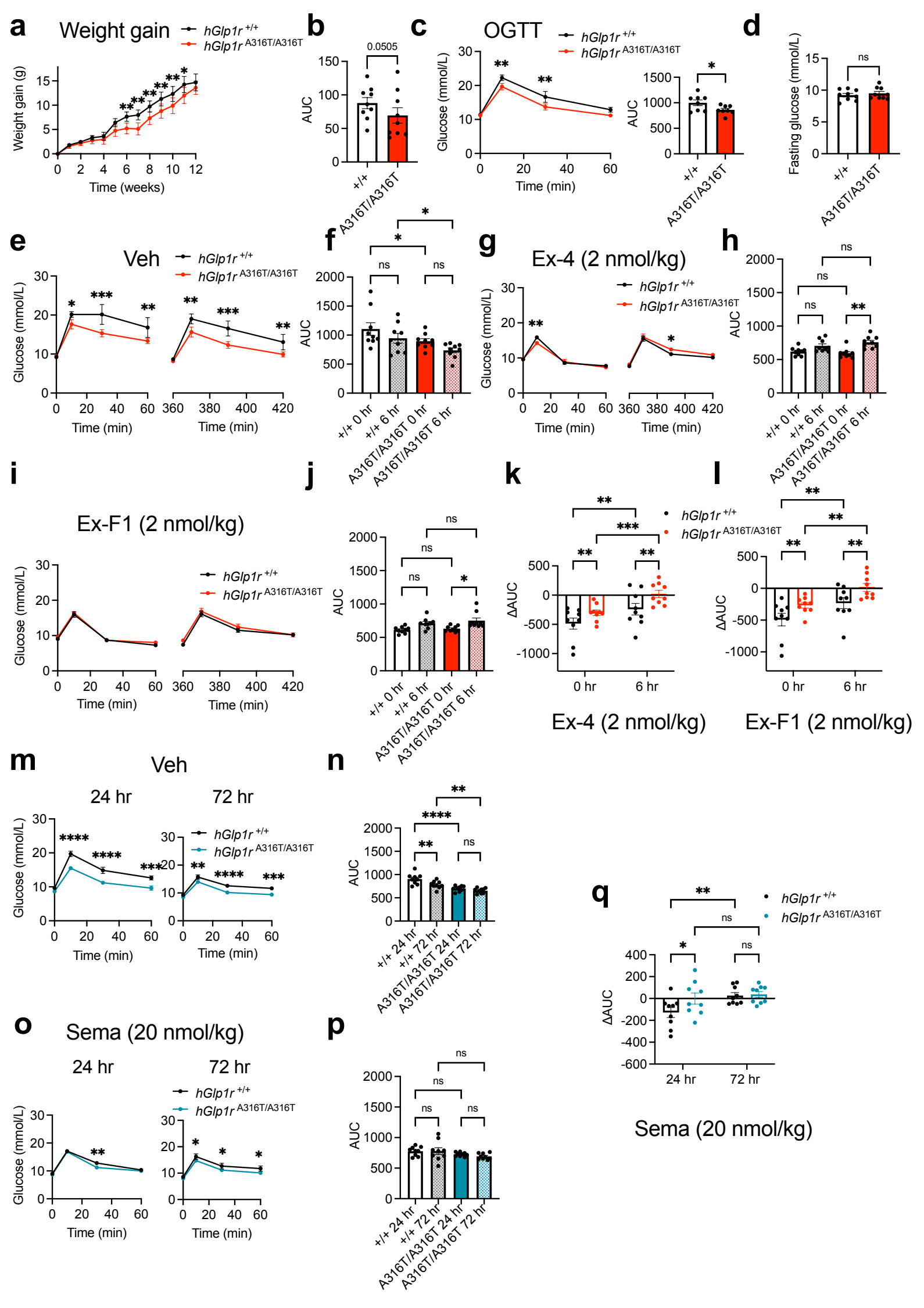
a
Weight gain
hGlp1r +/+
hGlp1r A316T/A316T
Weight gain (g)
Time (weeks)
b
0.0505
AUC
+/+
A316T/A316T
c
OGTT
Glucose (mmol/L)
Time (min)
AUC
d
Fasting glucose (mmol/L)
ns
e
Veh
Glucose (mmol/L)
Time (min)
f
AUC
ns
+/+ 0 hr
+/+ 6 hr
A316T/A316T 0 hr
A316T/A316T 6 hr
g
Ex-4 (2 nmol/kg)
h
i
Ex-F1 (2 nmol/kg)
j
k
ΔAUC
0 hr
6 hr
Ex-4 (2 nmol/kg)
l
Ex-F1 (2 nmol/kg)
m
Veh
24 hr
72 hr
n
o
Sema (20 nmol/kg)
p
q
Sema (20 nmol/kg)

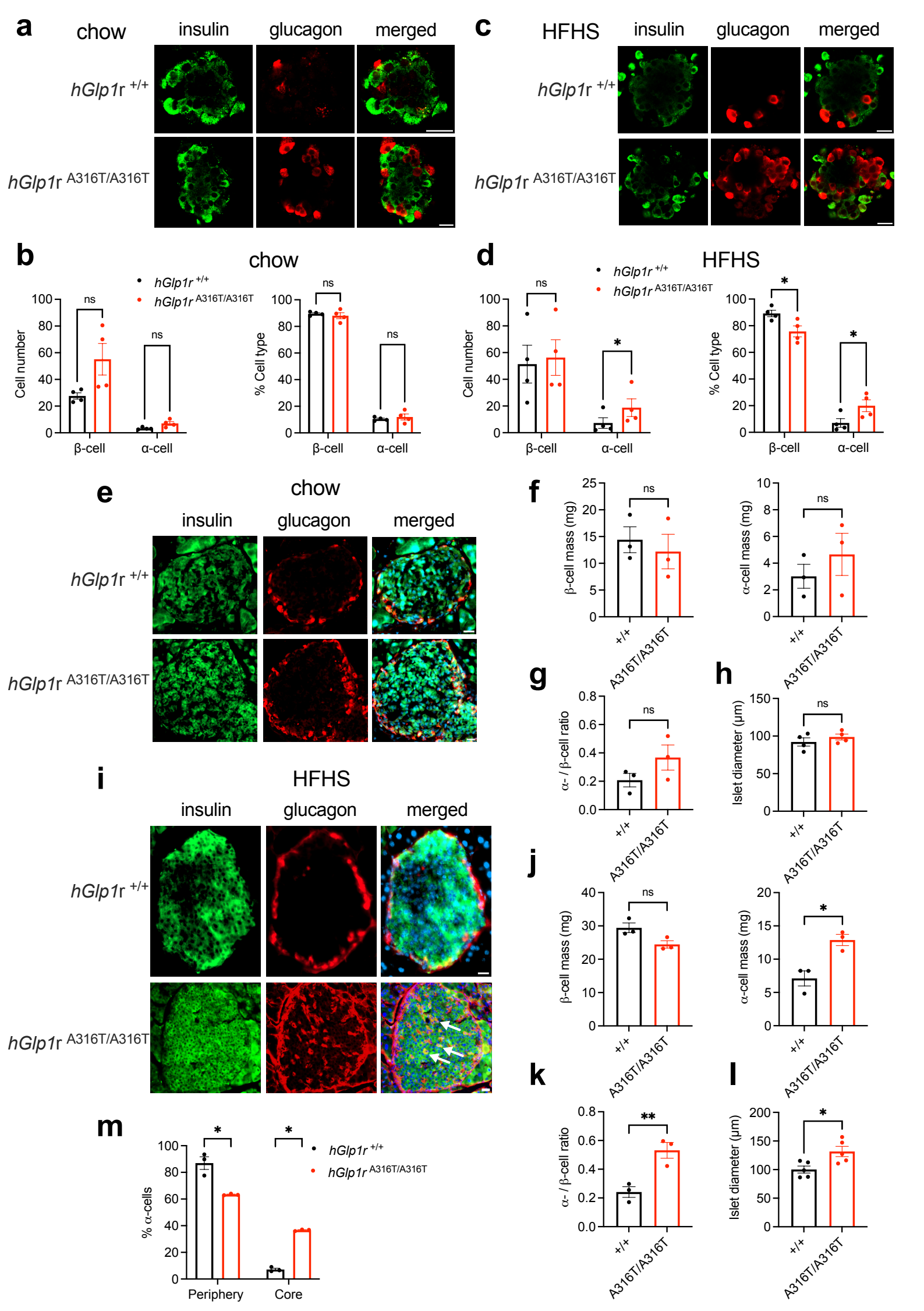
a
chow
insulin
glucagon
merged
hGlp1r +/+
hGlp1r A316T/A316T
c
HFHS
insulin
glucagon
merged
hGlp1r +/+
hGlp1r A316T/A316T
b
chow
hGlp1r +/+
hGlp1r A316T/A316T
Cell number
% Cell type
ns
β-cell
α-cell
d
HFHS
hGlp1r +/+
hGlp1r A316T/A316T
Cell number
% Cell type
ns
*
β-cell
α-cell
e
chow
insulin
glucagon
merged
hGlp1r +/+
hGlp1r A316T/A316T
f
β-cell mass (mg)
α-cell mass (mg)
ns
+/+
A316T/A316T
g
α- / β-cell ratio
ns
h
Islet diameter (µm)
ns
i
HFHS
insulin
glucagon
merged
hGlp1r +/+
hGlp1r A316T/A316T
j
β-cell mass (mg)
α-cell mass (mg)
ns
*
k
α- / β-cell ratio
**
l
Islet diameter (µm)
*
m
% α-cells
*
hGlp1r +/+
hGlp1r A316T/A316T
Periphery
Core

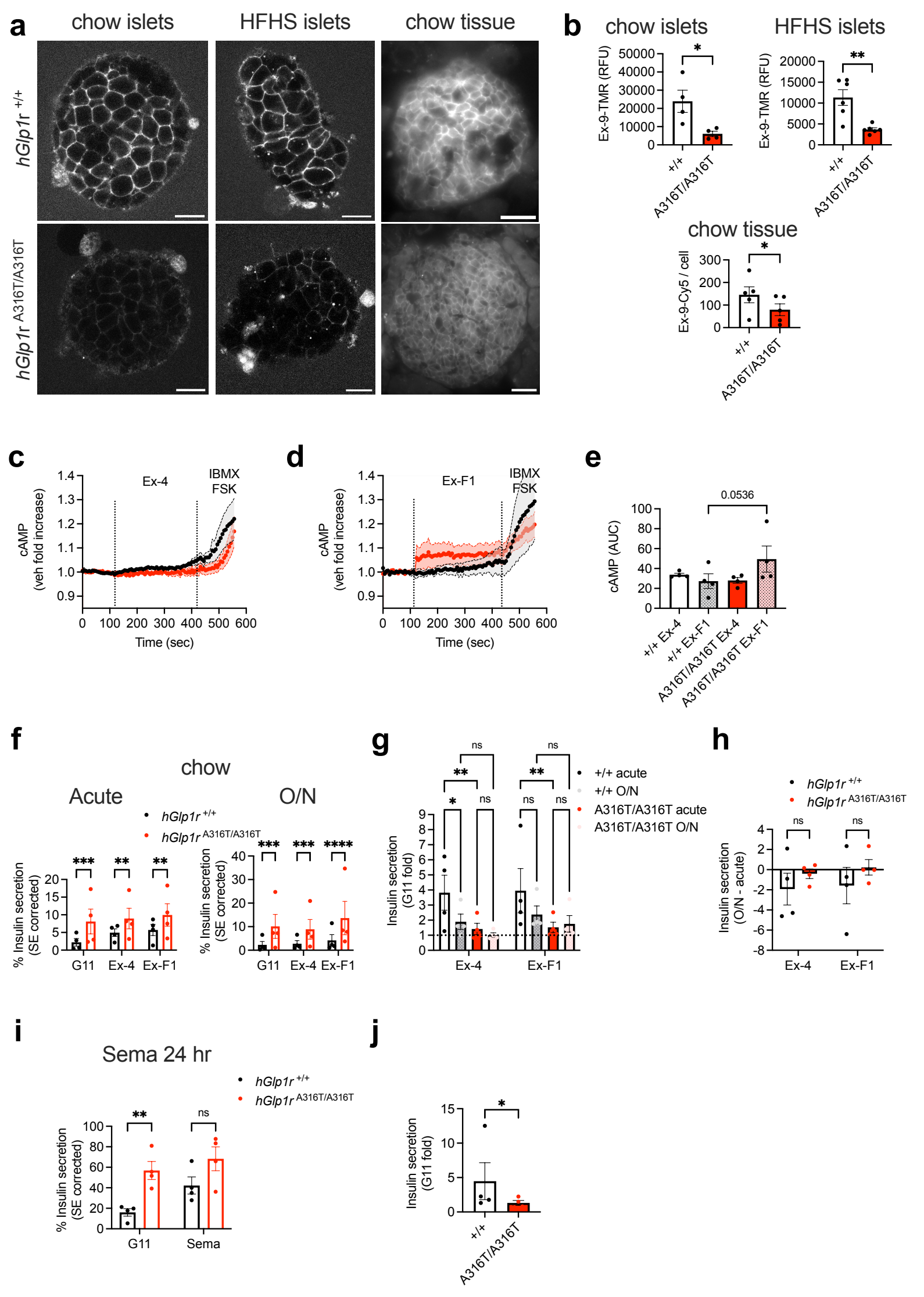
a
chow islets
HFHS islets
chow tissue
hGlp1r +/+
hGlp1r A316T/A316T
b
chow islets
HFHS islets
Ex-9-TMR (RFU)
+/+
A316T/A316T
chow tissue
Ex-9-Cy5 / cell
c
Ex-4
IBMX
FSK
cAMP
(veh fold increase)
Time (sec)
d
Ex-F1
e
0.0536
cAMP (AUC)
+/+ Ex-4
+/+ Ex-F1
A316T/A316T Ex-4
A316T/A316T Ex-F1
f
chow
Acute
O/N
hGlp1r +/+
hGlp1r A316T/A316T
% Insulin secretion
(SE corrected)
G11
Ex-4
Ex-F1
g
ns
+/+ acute
+/+ O/N
A316T/A316T acute
A316T/A316T O/N
Insulin secretion
(G11 fold)
h
Insulin secretion
(O/N - acute)
i
Sema 24 hr
Sema
j

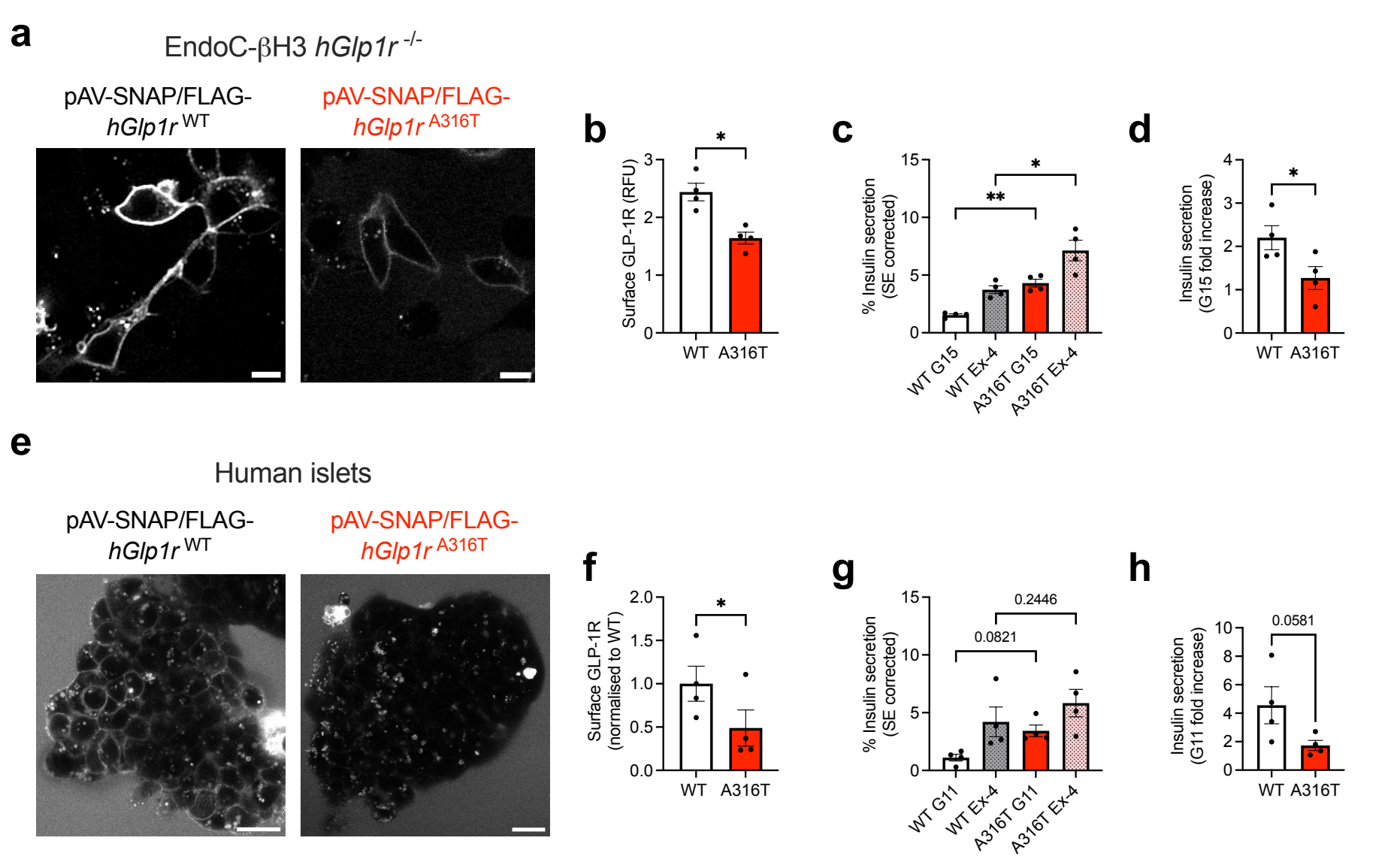
a
EndoC-βH3 hGlp1r -/-
pAV-SNAP/FLAG-hGlp1r WT
pAV-SNAP/FLAG-hGlp1r A316T
b
Surface GLP-1R (RFU)
WT
A316T
c
% Insulin secretion (SE corrected)
WT G15
WT Ex-4
A316T G15
A316T Ex-4
d
Insulin secretion (G15 fold increase)
WT
A316T
e
Human islets
pAV-SNAP/FLAG-hGlp1r WT
pAV-SNAP/FLAG-hGlp1r A316T
f
Surface GLP-1R (normalised to WT)
WT
A316T
g
% Insulin secretion (SE corrected)
0.2446
0.0821
WT G11
WT Ex-4
A316T G11
A316T Ex-4
h
Insulin secretion (G11 fold increase)
0.0581
WT
A316T

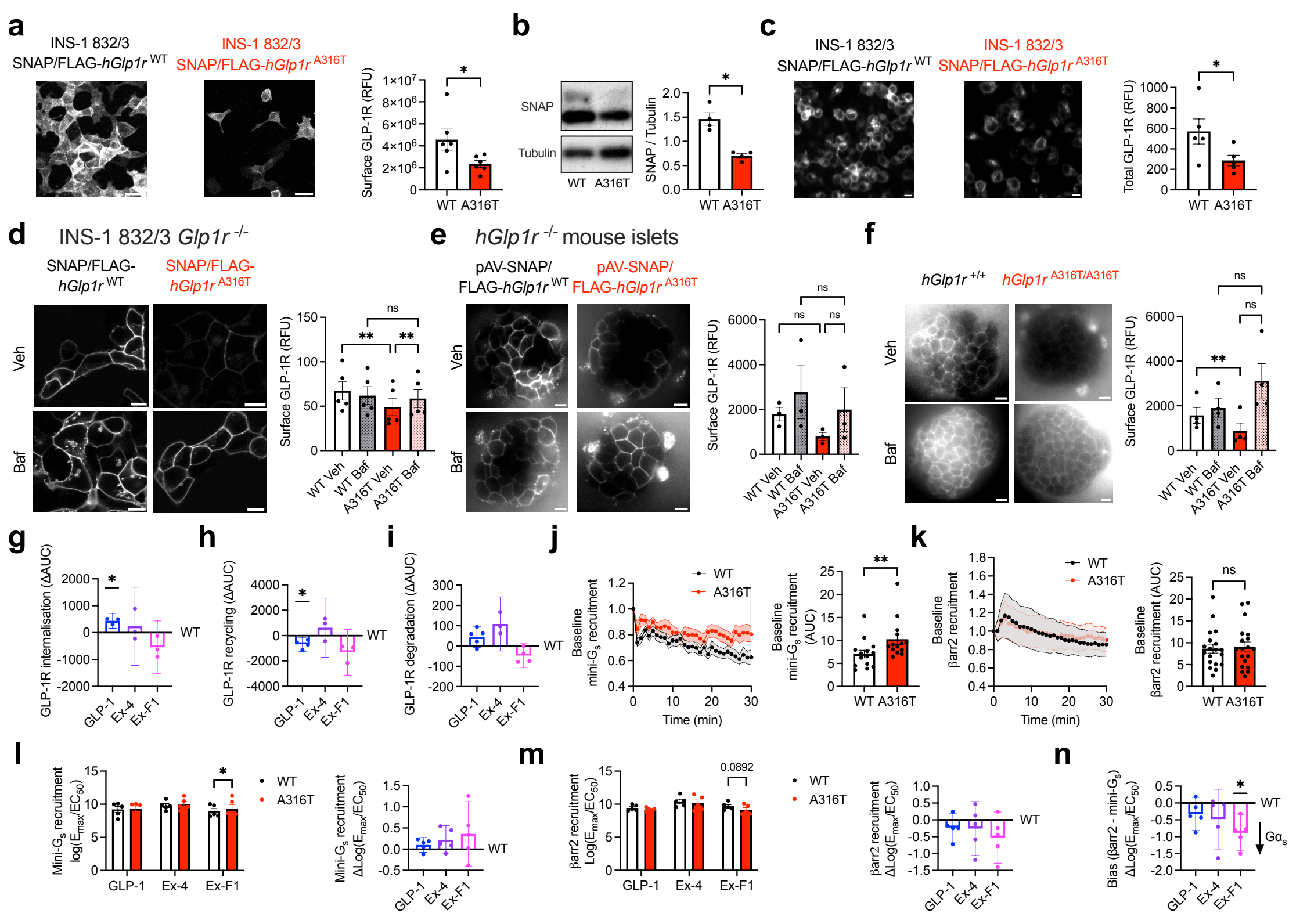
a
INS-1 832/3
SNAP/FLAG-hGlp1r WT
INS-1 832/3
SNAP/FLAG-hGlp1r A316T
Surface GLP-1R (RFU)
WT A316T
b
SNAP
Tubulin
WT A316T
SNAP / Tubulin
c
INS-1 832/3
SNAP/FLAG-hGlp1r WT
INS-1 832/3
SNAP/FLAG-hGlp1r A316T
Total GLP-1R (RFU)
d
INS-1 832/3 Glp1r -/-
SNAP/FLAG-hGlp1r WT
SNAP/FLAG-hGlp1r A316T
Veh
Baf
Surface GLP-1R (RFU)
ns
WT Veh
WT Baf
A316T Veh
A316T Baf
e
hGlp1r -/- mouse islets
pAV-SNAP/FLAG-hGlp1r WT
pAV-SNAP/FLAG-hGlp1r A316T
Veh
Baf
Surface GLP-1R (RFU)
f
hGlp1r +/+
hGlp1r A316T/A316T
Veh
Baf
Surface GLP-1R (RFU)
g
GLP-1R internalisation (ΔAUC)
GLP-1
Ex-4
Ex-F1
WT
h
GLP-1R recycling (ΔAUC)
i
GLP-1R degradation (ΔAUC)
j
Baseline mini-Gs recruitment
Time (min)
WT
A316T
Baseline mini-Gs recruitment (AUC)
k
Baseline βarr2 recruitment
Baseline βarr2 recruitment (AUC)
l
Mini-Gs recruitment log(Emax/EC50)
Mini-Gs recruitment ΔLog(Emax/EC50)
m
βarr2 recruitment Log(Emax/EC50)
0.0892
βarr2 recruitment ΔLog(Emax/EC50)
n
Bias (βarr2 - mini-Gs) ΔLog(Emax/EC50)
Gαs

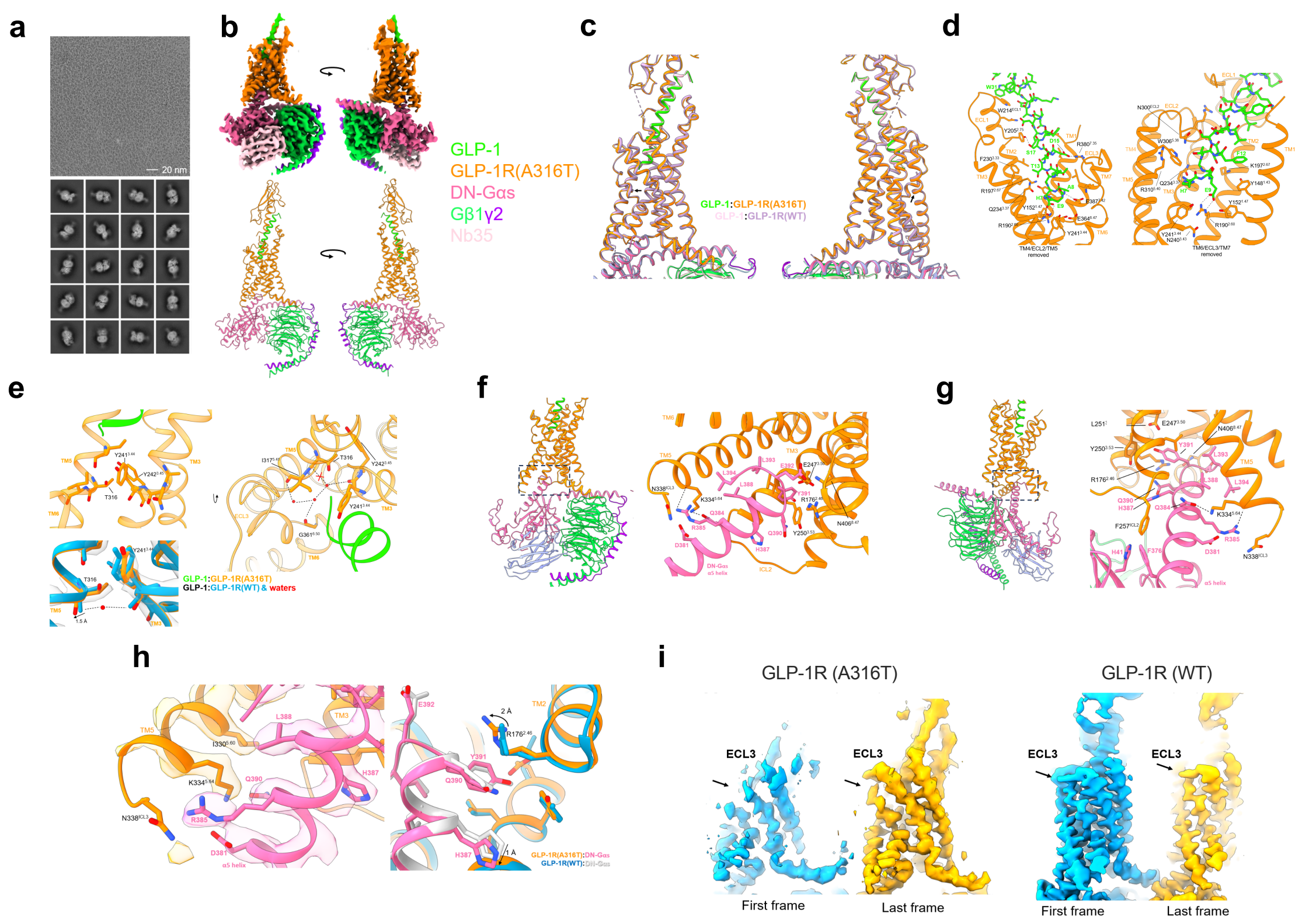
a
20 nm
b
GLP-1
GLP-1R(A316T)
DN-Gαs
Gβ1γ2
Nb35
c
GLP-1:GLP-1R(A316T)
GLP-1:GLP-1R(WT)
d
TM4/ECL2/TM5 removed
TM6/ECL3/TM7 removed
e
GLP-1:GLP-1R(A316T)
GLP-1:GLP-1R(WT) & waters
1.5 Å
f
DN-Gαs α5 helix
ICL2
g
α5 helix
h
α5 helix
2 Å
1 Å
GLP-1R(A316T):DN-Gαs
GLP-1R(WT):DN-Gαs
i
GLP-1R (A316T)
GLP-1R (WT)
ECL3
First frame
Last frame

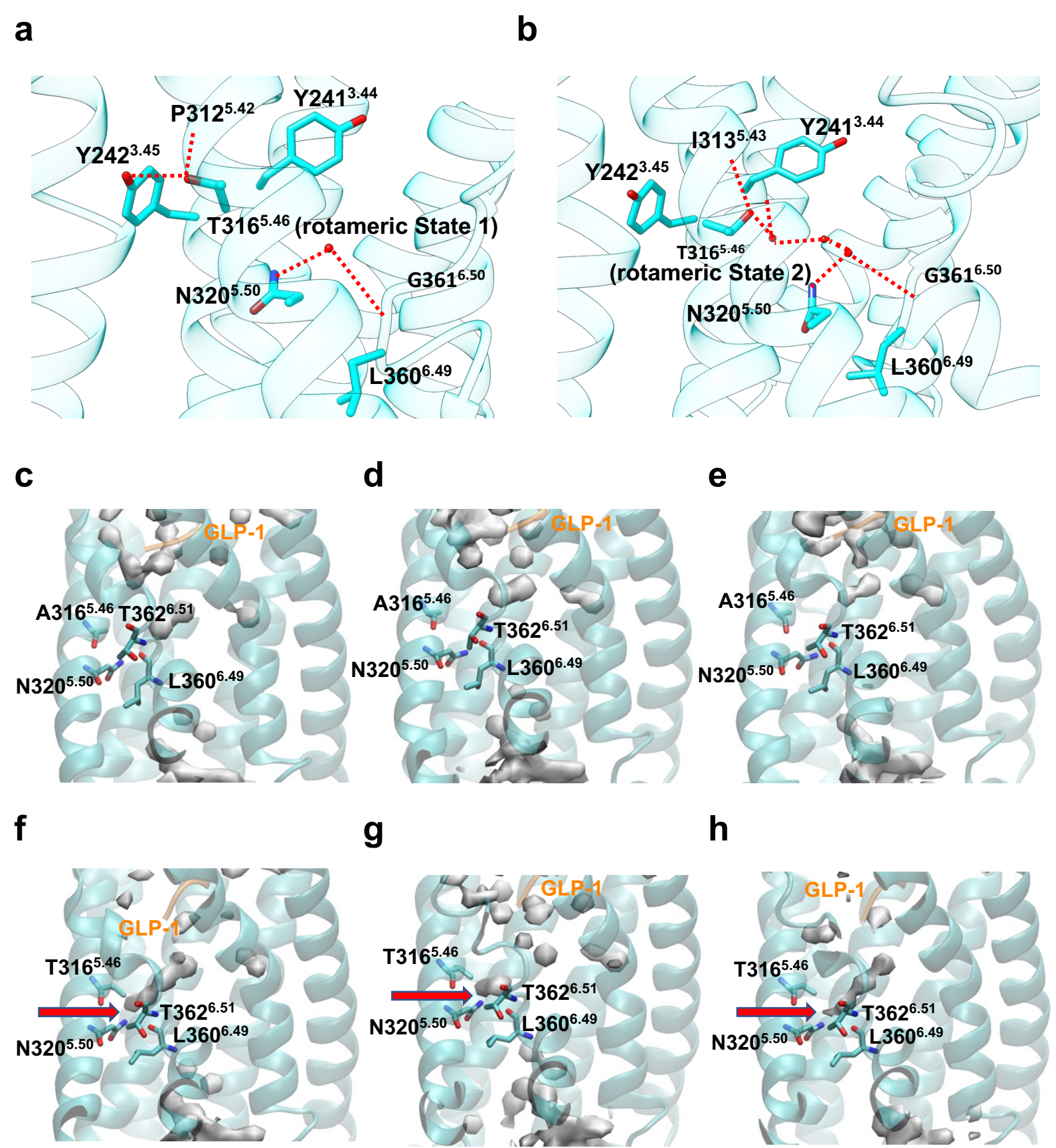
a
P312 5.42
Y241 3.44
Y242 3.45
T316 5.46 (rotameric State 1)
N320 5.50
G361 6.50
L360 6.49
b
I313 5.43
Y241 3.44
Y242 3.45
T316 5.46
(rotameric State 2)
G361 6.50
N320 5.50
L360 6.49
c
GLP-1
A316 5.46
T362 6.51
N320 5.50
L360 6.49
d
GLP-1
A316 5.46
T362 6.51
N320 5.50
L360 6.49
e
GLP-1
A316 5.46
T362 6.51
N320 5.50
L360 6.49
f
GLP-1
T316 5.46
T362 6.51
N320 5.50
L360 6.49
g
GLP-1
T316 5.46
T362 6.51
N320 5.50
L360 6.49
h
GLP-1
T316 5.46
T362 6.51
N320 5.50
L360 6.49